ASPECTS OF MATHEMATICAL BIOLOGY: FROM SELF-ORGANISATION OF THE CYTOSKELETON TO TRANSPORT OF MIGRATORY SPECIES

by
Aleksandra Zofia Płochocka

Submitted for the degree of
Doctor of Philosophy

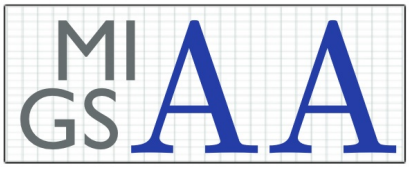

The Maxwell Institute Graduate School in Analysis & its Applications,
School of Mathematical and Computer Sciences,
Heriot-Watt University.

June 2019

Abstract

This thesis spans scales of mathematical biology, from single molecules to groups of organisms. We explore questions regarding the self-organisation of the cytoskeleton and the long distance migration of animals. Though disparate at first glance, both topics revolve around transport and self-organisation of biological particles.

We first model the microtubule cytoskeleton: a self-organising dynamic scaffolding along which cellular components, e.g. proteins, are transported. Its organisation is crucial for correct cellular functions; for example, maintaining the correct distribution of E-cadherin (the epithelial cell adhesion protein) along the cell boundary to ensure tissue integrity. Using stochastic simulations, genetic manipulations of the *Drosophila* epithelial cells and a probabilistic model we show that microtubule cytoskeleton self-organisation principally depends on cell geometry and microtubule seed density and is robust at the tissue scale.

We then extend this work. Specifically, we build and explore an analytical model and perform stochastic simulations to explain microtubule self-organisation in crowded cytoplasm, i.e. containing various highly anisotropic barriers. We consider *Drosophila* follicular epithelium cells, which contain actin cables throughout. We find that anisotropy in the cell interior leads to a significant increase in the number of microtubules pointing in the direction of the anisotropy. This allows us to deduce the type of interaction between microtubules and actin cables. We introduce a new measure of self-organisation of microtubules, the bundling factor, and use it to explore the persistent direction of transport created by microtubule bundles.

A second research topic is subsequently discussed. Many animals navigate long distances for purposes including foraging or nesting. While often mysterious, various lines of research support the idea that navigation is aided by a combination of cues whose magnitudes change with distance from the target. Motivated by agent-based simulations from a study of green sea turtle migration, we construct an abstract model for taxis-based animal navigation. We investigate the key properties of various navigating cues and their impact on animal migration, and discuss how the starting location can affect the mean first passage time of a migratory journey.

Dla mojej mamy.

Acknowledgments

First and foremost I would like to thank my supervisors Dr. Lyuba Chumakova and Prof. Kevin Painter; it was a great privilege to work with you and learn from you over these years. Thank you Lyuba for providing such an interesting project for us to work on; your passion for research has been contagious and I look forward to exploring more of the area you introduced me to in the future. You have always supported me tremendously in everything I do; from presentations to job applications. To Kevin: thank you for all your patience and wisdom. There have been many times during my PhD when I have panicked about my work and your advice always helps me persevere.

I would also like to acknowledge Dr. Natalia Bulgakova. Thank you for always maintaining a positive attitude even when answering my very basic biology questions and providing such interesting experiments for us to model.

Thank you to Prof. Sandy Davie for introducing me to the beauty of probabilistic modelling in mathematics.

My time in Edinburgh was significantly enriched by the mathematical biology group at Heriot Watt University and the applied mathematics group at Edinburgh University. Throughout seminars, coffee breaks and hill-walking these academics always made me feel that I belong to the Universities. Thank you to the many people that during my PhD always helped me to see the big picture: Gissell Estrada, Konstanze Simbriger, Aleksandra Szyk, Dave Burrell, Paul Dobson, Ben Goddard, Gleb Zhelezov and many of the wonderful members of the Edinburgh Tango Society.

Thank you to my parents for being by my side even half a world away.

Finally, thank you to Martín for always dancing with me.

Aleksandra was supported by The Maxwell Institute Graduate School in Analysis and its Applications, a Centre for Doctoral Training funded by the UK Engineering and Physical Sciences Research Council (grant EP/L016508/01), the Scottish Funding Council, Heriot-Watt University and the University of Edinburgh.

ACADEMIC REGISTRY

Research Thesis Submission

Name*:*			
School:			
Version: *(i.e. First, Resubmission, Final)*		Degree Sought:	

Declaration

In accordance with the appropriate regulations I hereby submit my thesis and I declare that:

1) the thesis embodies the results of my own work and has been composed by myself
2) where appropriate, I have made acknowledgement of the work of others and have made reference to work carried out in collaboration with other persons
3) the thesis is the correct version of the thesis for submission and is the same version as any electronic versions submitted*.
4) my thesis for the award referred to, deposited in the Heriot-Watt University Library, should be made available for loan or photocopying and be available via the Institutional Repository, subject to such conditions as the Librarian may require
5) I understand that as a student of the University I am required to abide by the Regulations of the University and to conform to its discipline.
6) I confirm that the thesis has been verified against plagiarism via an approved plagiarism detection application e.g. Turnitin.

* *Please note that it is the responsibility of the candidate to ensure that the correct version of the thesis is submitted.*

Signature of Candidate*:*		Date:	

Submission

Submitted By *(name in capitals):*	
Signature of Individual Submitting:	
Date Submitted:	

For Completion in the Student Service Centre (SSC)

Received in the SSC by *(name in capitals):*			
Method of Submission *(Handed in to SSC; posted through internal/external mail):*			
*E-thesis Submitted (**mandatory for final theses)***			
Signature:		Date:	

Please note this form should be bound into the submitted thesis.

Contents

Chapter 1

Introduction

The goal of mathematical biology is to explain observed biological phenomena using mathematical techniques. It involves the delicate balance of using enough biological assumptions to better describe the system while excluding many of the complicated details. Despite technological advances, biological experiments cannot elucidate everything about a given system due to inherent limitations. For example, microscopy is confined to magnification limits and may only give a snapshot of the system at a single point in time. Francis Crick believed that "the job of theorists is to make predictions" [32], regardless of whether they turn out to be correct or not: knowing that a system cannot behave a certain way is crucial for understanding it better.

Mathematical modelling relies on building an abstraction of reality. Many systems are far too complex to be understood without the use of a simple mathematical model and even if experiments can be carried out they are often expensive. In the *Physical Biology of the Cell* the authors argue that including theoretical models is what changes vast amounts of data into "meaningful scientific results" [124]. We are currently living in a time of tremendous technological advances which leads to the generation of huge volumes of data [31], so the need for mathematical modelling has become particularly acute.

The advances in mathematical modelling closely relate to the availability and limitations of experimental data existing at the time. During the 1700s, there was little available data, nonetheless human population size was already measured. Bernoulli, motivated by the devastating impact of smallpox, developed quantitative models of population dynamics [16]. With the emergence of techniques to study bacteria at microscopic detail, Fisher created a fundamental model for the evolutionary biology of bacteria [47], still in use today [145]. Hodgkin and Huxley's combination of the-

ory and experiments in electrophysiology using the giant squid[1] contributed to our understanding of neural signalling, providing the foundations of many models on ion channel kinetics. Finally, in the absence of related biological experiments, mathematical models can predict biological behaviour. One such example is Alan Turing's seminal paper "The chemical basis of morphogenesis" [153], which laid the foundations for theoretical studies of biological pattern formation. Subsequently there have been several biological systems where his ideas have been proposed to operate [130, 112, 151, 77].

In recent years, with the development of super-resolution microscopy, a frontier of mathematical biology has shifted to the biology of the cell. At an entirely different scale, it is also now possible to use GPS tracking to evaluate long distance migrations of animals. In this thesis, we contribute to the advances of the mathematical biology field by addressing the following questions:

i How does the microtubule cytoskeleton self-organise in *Drosophila* (fruit fly) epithelial cells?

ii How does an anisotropic cytoplasm impact on the self-organisation of the microtubule cytoskeleton?

iii How do different modes of taxis-based navigation combine to allow successful animal migration?

The overarching theme of this thesis is transport in biological systems. Both systems require mathematical modelling: the dynamics of individual microtubules cannot be easily imaged, so models are needed to explain microtubule cytoskeleton dynamics; similarly, animal tracking studies are rarely able to track large groups of migratory species over the course of their journeys through complicated environments. Most importantly, we believe understanding the underlying forces which drive successful cytoskeleton self-organisation and animal migration can be greatly aided through mathematical modelling.

[1]The vast size of the giant squid axon enabled them to carry out experiments to test their model, which would not have been possible at the time with smaller model organisms such as a mouse or fruit fly.

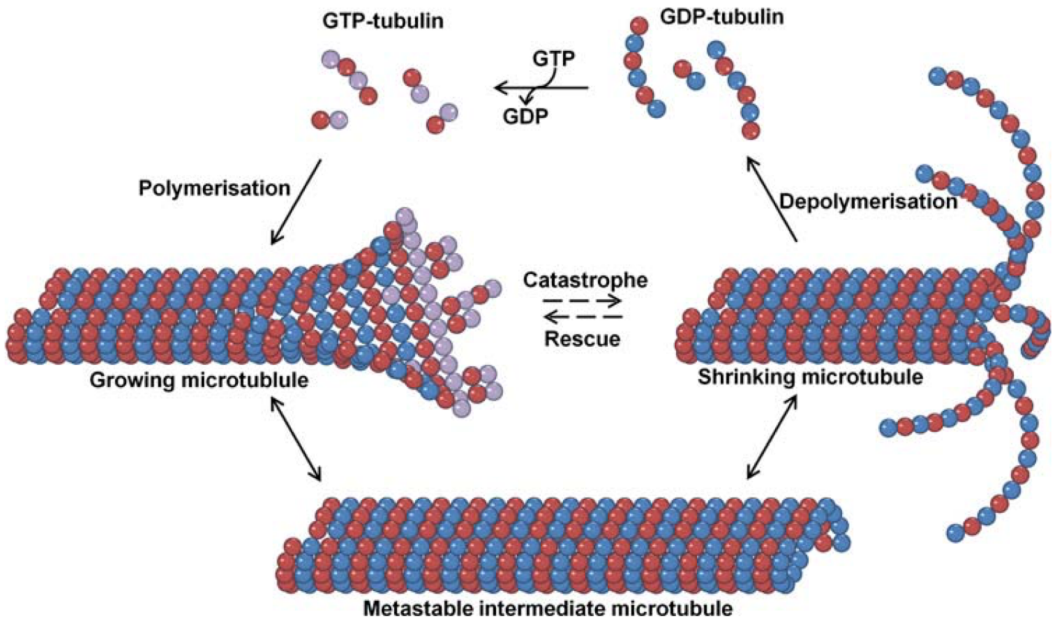

Figure 1.1: A schematic showing the dynamic instability of microtubules reproduced from [24] with permission.

1.1 Biology of the cytoskeleton

All eukaryotic (animal, plant and fungal) cells have two things in common: membrane-bound organelles and a cytoskeleton. Organelles, such as the cell nucleus, are subunits of the cell which carry out specific functions. The cytoskeleton is responsible for giving the cell its shape and enabling the transport of necessary components. Here we introduce two cytoskeletal filaments: actin filaments and microtubules, as well as motor proteins. For a more extensive description see [6, 15, 124, 13].

1.1.1 Cytoskeletal filaments

Microtubules are crucial to the transport of proteins inside the cell and in the distribution of chromosomes to daughter cells during mitosis (cell division). As their name suggests, they assemble from tubulin dimers into long hollow tubes of diameter approximately 25nm. Microtubules are highly dynamic and consist of polarized proteins made up of alpha ($-$) and beta ($+$) tubulin. The inner chain of the microtubules consist of tubulin guanosine diphosphates (T.GDP) and the end protein is either a T.GDP or a tubulin guanosine triphosphate (T.GTP). The growth of mi-

crotubules ($0.1 - 0.4\mu$m/s [94]) is accounted for by GTP hydrolysis and shrinking is controlled by GDP dissociation. The filaments self-assemble if they contain the T.GTP end, via associating with another T.GTP to lengthen the inner chain by one tubulin subunit and keeping a T.GTP end in place for further possible growth. If the filaments are capped with T.GDP at the end of their chain then the microtubules dissociate. Due to this reason, T.GTP is known as the polymerising cap: its presence promotes growth and its absence causes shrinking. Microtubule dynamics are characterised by the process of "dynamic instability", where they grow until the microtubule cap is lost, at which point the dynamics undergo "catastrophe" as they fall into the depolymerising state. Yet, they are also potentially able to reacquire a cap during these dynamics in "rescue", returning to a polymerising state (see Figure 1.1). Microtubules are also able to "pause", such that their chain of tubulin subunits remains at a constant length for a period of time. Note that only one end of a microtubule has the ability to grow or shrink, as they only assemble radially out of "plus-ends"; their "minus-ends" ("seeds") remain intact throughout the dynamics.

The second cytoskeletal component of interest in this thesis are actin filaments (otherwise referred to as microfilaments). They are made out of actin: a multifunctional protein whose monomers form long, double helical chains. They are the smallest filaments in the network, with a diameter ranging between 7 and 9nm. Actin filaments are polarized, with both barbed (+) and pointed (−) ends. Moreover, actin can either form a branched network (mesh) of thin interconnected filaments (found in lamellipodia), or fibers containing either parallel or anti-parallel actin filaments (found in filopodia and contractile bundles). Due to their polarized ends, actin filaments are also highly dynamic, with growth dependant on adenosine triphosphate (ATP) hydrolysis at the barbed ends and shrinking based on adenosine diphosphate (ADP) dissociation at the pointed ends [15]. The transition between the growing state of actin filaments (ATP end) and the dissociating state (ADP end) is governed by phosphorylation. In this way the reversibility and growth resembles the dynamics of microtubules. However, actin filaments self assemble at a slower rate in comparison to microtubules ($0.005\,\mu$m/s [136]) and dynamics occur at both ends of the chain. Actin filaments are often found near cell boundaries, where "cortical actin" strongly interacts with membrane proteins in order for the cell to sense and respond to external stimuli [84].

The third type of cytoskeletal filament are intermediate filaments, measuring 10nm in diameter. Instead of playing a role in cell motility like the other two fil-

aments, intermediate filaments give cells their structural integrity. The dynamics of intermediate filaments are very different from the assembly of microtubules and microfilaments, using tubulin and actin respectively, since intermediate filaments are composed of many different proteins (currently over 50 proteins have been identified). In our study we do not model intermediate filaments because they are not located in our plane of interest where the microtubules self-organise in the *Drosophila* epithelial cells.

1.1.2 Motor proteins

Motor proteins are essential for the delivery of biologically required proteins to different parts of the cell. We can think of them as vehicles which transport cargo along the cytoskeleton through movement along actin filaments or microtubules. The basic function of motor proteins is to convert the chemical energy from ATP hydrolysis into mechanical energy, and then use this energy to move along a particular fibril. There are many types of motor proteins, for example kinesin, dynein and myosin. Actin filaments act as tracks for myosin motors which bind to and "walk" along them, while microtubules are tracks for kinesin and dynein motors. Specifically, kinesin binds to a vesicle or other organelle and moves along the microtubule from the minus towards the growing plus end, while dyneins move in the opposite direction.

1.1.3 Previous work

The geometry of microtubules in cells varies: in neurons they are parallel and point in the same direction of axons, they grow radially from centrosomes and, for the case under exploration in this thesis, they grow from the perimeter along the adhesion belt in *Drosophila* epithelium cell. Altering the microtubule dynamics in different geometries is shown to lead to pathologies such as neurological diseases and cancer.

In axons, microtubules play an essential role in axonal transport[2], travelling the length of the axon and providing tracks for the transport of crucial components [76]. It is hypothesised that several neurodegenerative diseases stem from disruptions to the cytoskeleton network within axons. Consequently, microtubules are currently seen as a new therapeutical target for combatting injury and disease of the nervous system, with the aim of neuronal therapy being to stop the degradation of microtubule dynamics [29, 1, 34]. This problem has been studied with various modelling

[2]Axonal transport involves the movement of necessary proteins to the synapse.

approaches, such as viscoelastic [139] or stochastic multiscale models [160]. The models are very different to our system because of the specific geometry of the axon.

Centrosomal microtubules play an important role within the field of cancer therapeutics over recent decades. During mitosis, microtubules are organised in two centrosomes to separate a line of chromosomes and, by controlling the highly dynamic mitotic spindle during cancer proliferation, the aim is to slow tumour proliferation [41]. Theoretical work on the mitotic spindle ranges from discrete to continuous models [141] with one major modelling approach exemplified with the foundation of Cyto-Sim [137]. This open source software allows users to model structures such as flexible polymers and spheres representative of microtubules and other cell components. While modelling via this software has allowed exploration of spindle function within various setups [103, 116], our system does not contain microtubule organising centres (centrosomes) and therefore demands a different modelling approach.

For our system many microtubules are seeded at the cell boundary and E-cadherin, the epithelial adhesion protein, is delivered to the adhesion belt. In previous studies by our experimental collaborators, it was observed that altering microtubule self-organisation altered the dynamics of cell-cell junctions and is therefore influencing cell motion in tissue [22]. It is hypothesised that this is essential for understanding such phenomena as wound healing.

Current research focuses on *in vitro* systems, where stabilised microtubules are placed on a dish and their dynamics are observed [49, 53, 107]. Theoretical models of microtubule dynamics have been studied since 1985 [28], yet many results (e.g. [122, 75, 9]) are only relevant to *in vitro* experiments and not *in vivo* systems. A system in live tissue could behave differently from microtubules stabilised in a dish. Furthermore, various scales of the cytoskeleton have been investigated using reaction diffusion models [57], simple mechanical elastic, viscoelastic, poroviscoelastic continuum, porous gel or soft glassy material models [84]. In mathematical modelling many continuous models have been developed for both microtubules and actin filaments. Mogilner and Oster developed models to capture the force-velocity relation of a single microtubule [111], Portet et al. constructed theories for microtubule self-organisation under the influence of gravity [110] whereas Mogilner and Edelstein-Keshet focused on work relating to actin protrusions self-organising to produce cell motility [126].

A differentiating aspect of this work is that we model an *in vivo* system. Cytoskeleton components have been studied over many years, yet surprisingly little is known about the networks they form inside cells *in vivo*. Biologically, experimental

Figure 1.2: Images taken during a visit to the Bulgakova fly lab at the University of Sheffield. Left hand side shows different types of *Drosophila* used for experiments and right hand side shows an image taken of several immobilised *Drosophila* through the lense of a microscope.

techniques have improved over the years due to the rise of new technology and recent experimental advances include inducing small perturbations to the cell in order to investigate the response in dynamics [84]. Amongst the biggest current limitations are measuring processes: for example, microscopy enables us to see bundles of microtubules but does not allow individual counting due to the insufficient image resolution. To our knowledge a similar modelling approach to our methods can only be found in [67, 35] to model plant microtubules.

1.1.4 Motivation and biological experiments

Our work on the self-organisation of the cytoskeleton forms part of an interdisciplinary project in collaboration with the group of Dr. Natalia Bulgakova (Department of Biomedical Science, University of Sheffield). The collaboration between the two groups is actively taking place at the University of Edinburgh and Sheffield University; some of the images taken during the lab visits can be seen in Figure 1.2. The iterative process in which modelling is discussed directly with experimentalists has helped ensure that our mathematical model is consistent with current biological assumptions and hypotheses. For useful models to be developed it is crucial to understand experimental approaches and their limitations.

Our model system is the *Drosophila* embryo during stages 12 to 15 of devel-

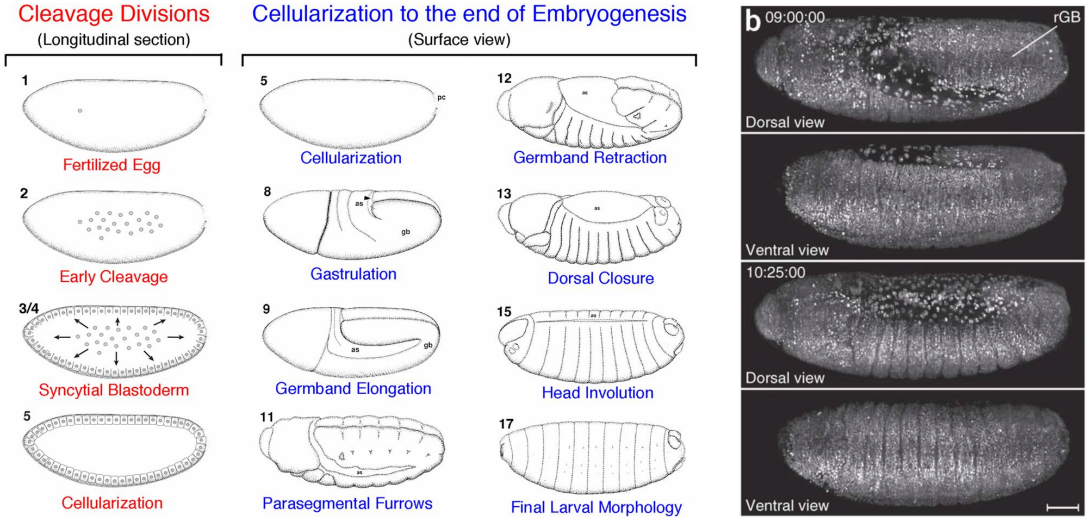

Figure 1.3: Left hand side: An illustration of the stages of development for the *Drosophila* embryo, reproduced from [64] with permission. Right hand side: The dorsal and ventral view of a *Drosophila* embryo during germband retration (stage 12), reproduced from [150] with permission.

opment. In this period the embryo undergoes germband retraction, dorsal closure and head involution, as seen in Figure 1.3. During development the volume of the *Drosophila* embryo remains the same. The embryo is under compression in the anterior-posterior plane[3] and stretches perpendicular to this axis. Therefore, as the embryo proceeds from stage 12 to stage 15, the apical (surface) epithelial cells elongate with respect to the dorsal-ventral axis[4]. Figure 1.3 demonstrates the experimental images of these stages.

Our model system is unique in comparison to standard experimental systems because we consider cortical microtubules that do not anchor at the centrosomes, but rather are seeded at the cell boundary along the thin layer $(1-2\mu m)$ near the top of the cell. A schematic of the cells can be seen in Figure 1.4 and representative data from a top view of the cells is given in Figure 1.5. Furthermore, the centrosome is not in the planar region of the cortical microtubule dynamics but in a much lower part of the cell. Since cortical microtubules are seeded along the adhesion band and their dynamics are restricted to a $1\mu m$ thin apical (top) layer of the cell we can reasonably model our system as a quasi 2D system, given that we are principally interested in microtubules within this slice of the epithelial cells. Note that the biological

[3]The anterior-posterior plane runs from the head to the tail of the *Drosophila*.
[4]The dorsal-ventral axis connects the belly of the *Drosophila* to its back.

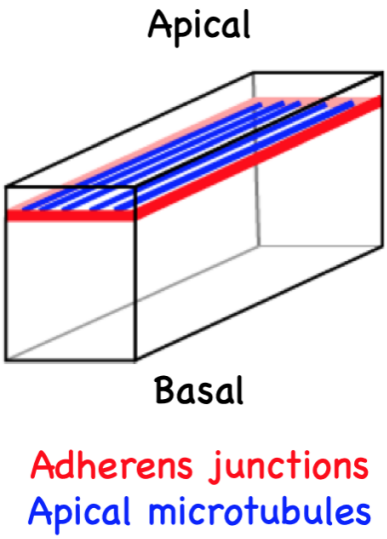

Figure 1.4: A schematic of our *Drosophila* embryo epithelial cells (courtesy of Natalia Bulgakova).

mechanism responsible for restricting the microtubule dynamics to the apical layer is not yet understood. The images in Figure 1.5 highlight a key experimental limitation: single microtubules cannot be imaged or counted, hence motivating a mathematical model that can describe the interaction of microtubules under varying geometries and biological parameters.

Previous work by the group explored certain aspects of cell-cell adhesion, in particular the transport of E-cadherin along microtubules to its needed location. Cell-cell adhesion is achieved when the transmembrane, calcium-dependent protein E-cadherin is delivered from the cell interior to the cell boundary, where it can bind to the corresponding transmembrane protein of neighbouring cells. Formation of stable adhesions between cells is necessary for tissue integrity and preventing them from falling apart. The group of Bulgakova has found that the distribution of E-cadherin on cell boundaries becomes asymmetric: while E-cadherin was uniformly distributed along the adhesion belt in early development stages, a shift of E-cadherin to the shorter sides of elongated cells is observed during the later stages of development [22]. It is hypothesised that, due to cell elongation, the increased amount of E-cadherin on the shorter sides (that are presumed to be pulled on) is required for regulatory tissue integrity. Using *Drosophila* cells from stages 12-15 of development (Figure 1.5), the group has carried out experiments and developed a mathematical model which demonstrates that geometry drives microtubule self-organisation in *Drosophila*

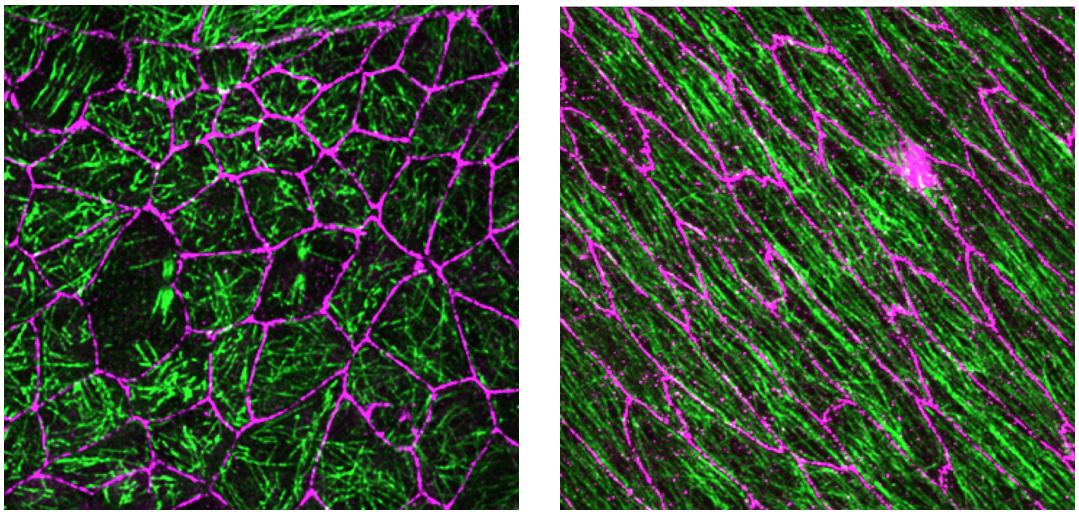

Figure 1.5: Images of epithelial tissue development of the *Drosophila* embryo from early state 12 (left) to stage 15 (right) courtesy of the Bulgakova lab. E-cadherin is stained using m-Cherry in magenta and microtubules are stained in green using GFP.

epithelium [58].

In this thesis, we have found not only that microtubule self-organisation is driven by cell geometry but that it is also highly robust on the tissue scale. In Chapter 2 we use stochastic simulations, as outlined in [58], to create a large parameter study for our model system. We further model the system using a simple probabilistic model in order to understand the effect of biological parameters on the self-organisation of microtubules in various tissues, and compare our data to experiments from the Bulgakova lab using image analysis techniques.

Chapter 3 introduces a non-homogeneous cell interior to investigate the dynamics of microtubules under various anisotropies of the cell, such as those generated by protein clusters, actin cables or flow generated in the cell by motor protein movement. Further, we adapt our stochastic simulations to include discrete barriers and calculate the microtubule bundling factor. This allows us to quantify the degree to which microtubules self-organise alongside each other. We hypothesise that bundled microtubules increase the rate of intracellular transport. We test our model on the *Drosophila* follicular epithelium tissues, where actin cables run throughout the cell bulk and compare the observed results to experimental data.

1.2 Animal navigation

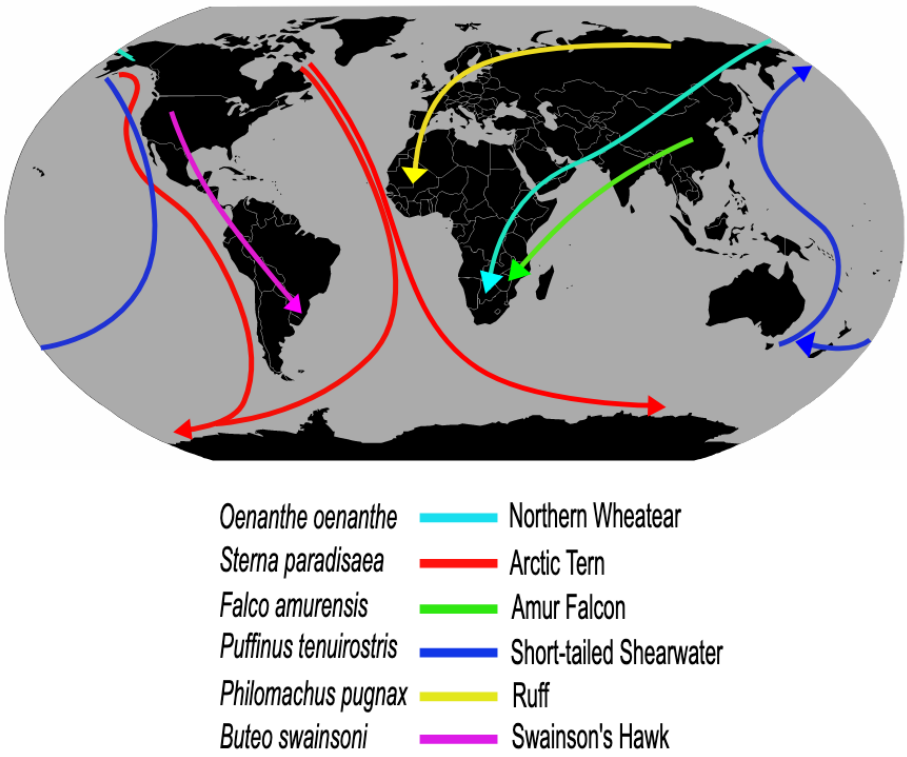

Figure 1.6: An example animal migration route map for several types of birds obtained from [30].

The entirely different question of animal migration is discussed in Chapter 4. Animal navigation is a remarkable biological phenomena and has fascinated scientists at least as far back as Aristotle. Examples of some of the migratory routes taken by birds can be seen in Figure 1.6. Charles Darwin marvelled about the ability of species to travel using "dead-reckoning" [33] whereas Von Wrangell wrote about his exposition to the polar sea in the 1820's, highlighting the ability of species "to keep a true course" [159]. Species and their corresponding methods of navigation vary greatly: the zig-zagging of moths as they follow odour plumes [90], the collective dynamics of honey bee swarms to new nesting sites [51], and the use of geomagnetic information in birds, turtles and other species [88, 44]. A main challenge persisting in the field of ecology is that of efficiently tracking animals to understand route determination. Although GPS trackers are readily available, there remain a number of challenges with using these technologies in the field: for example, equipment costs, battery lifespans or animals moving into untraceable regions (e.g. deep ocean) [156].

Consequently, there is need for further data as well as mathematical models to understand the co-ordinated and solitary movement of animal populations. To model the movement of species, researchers have therefore used various mathematical techniques, ranging from agent based models [129, 63, 121, 148] to macroscopic models [144, 8].

Chapter 4 discusses our modelling of animal navigation. We consider taxis-based navigators travelling as individuals during their foraging or nesting journeys. Our work expands on the approach discussed in [74]; we work with a PDE which describes the movement of an animal population scaled from an individual based velocity-jump process. To discuss various taxis-based cues we make use of the dynamical system found by looking at the characteristics of the PDE and investigate the resulting steady states and their nature. Further, we also discuss the use of an analogous position-jump process to derive the mean passage time of our system.

Chapter 2

Robustness of microtubule cytoskeleton self-organisation

This chapter has been submitted for publication and is a result of an interdisciplinary collaboration between Alexander Davie, Natalia Bulgakova, Lyuba Chumakova and myself. The *in vivo* manipulations in Section 2.3.1 and the biological methods covered in Section 2.6 were performed and written by Natalia Bulgakova. My contribution has been mathematical modelling of the system using stochastic simulations and probabilistic models.

2.1 Introduction

The correct positioning of intracellular components such as proteins and organelles is critical for correct cellular function [83, 134]. These components are transported to their biologically relevant locations by motor proteins moving along the cytoskeleton [50, 85, 52]. Therefore, the direction of cytoskeletal filaments guides intracellular transport, its direction and efficiency.

One common type of cytoskeleton used for transport is microtubules [50]. These are highly dynamic, unstable polymers, whose dynamic properties are influenced by a wide range of both internal and external factors. For example, dynamics and number of individual microtubules in a cell depend on the expression of particular plus-end and minus-end binding proteins [5]; interaction between microtubules is affected by the properties of the present cross-linking and motor proteins [86]; and, the stability of the microtubule network is affected by external factors e.g. temperature through

changing microtubule rigidity [87].

In this chapter we explore the self-organisation of microtubules in the epithelial cells in the model organism *Drosophila* embryo *in vivo*. Constrained to the thin $1\mu m$ apical layer of the cell, cortical microtubules grow in the plane of the adhesion belt, which allows us to model the system as quasi-2D *in silico*. To quantify the microtubule alignment we used the length-weighted microtubule angle distribution, which is more suitable than the $S2$ measure used in liquid crystals [67] in our case, since the microtubules are not dense in our system (see Figure 2.1A).

Various mechanisms of microtubule self-organisation have been studied in different tissues. However, many of them are specific to a particular tissue. In plants, it was shown that microtubule zipping strongly affects their self-organisation [67]; that tension can have a non-negligible effect on stabilizing microtubules [65]. In larger cells such as *Drosophila* oocytes, cortical microtubule nucleation was shown to be important [152]. Models that include the hydrodynamic effect of the cytoplasm and molecular motor effect on microtubules and their self-organisation is summarised in [141].

It was previously shown that microtubule self-organisation in *Drosophila* epithelia is guided by cell geometry to leading order both *in vivo* and *in silico* [58]. The authors discovered that the alignment of subapical microtubules in *Drosophila* epithelial cells increases with the cell elongation and confirmed this observation by quantifying the microtubule angle distribution in individual cells. Despite recent advances in super-resolution microscopy, no reliable high-throughput approaches exist to detect individual microtubules in dense networks, such as those present in epithelial cells. Therefore, our collaborator developed a method to quantify microtubule alignment from 3D-SIM microscopy images, where tubulin and cell boundaries were labelled with antibodies [58]. She extracts the microtubule direction at each pixel using signal intensity within its local neighbourhood, fitted the resulting histogram with von Mises distribution, and found that its standard deviation is a linear function of cell eccentricity. Smaller standard deviation values represented more aligned microtubules. Microtubule alignment was reduced when cells were not allowed to elongate, suggesting that this relationship is causal. The authors further developed a minimal *in silico* 2d-model which proved the causality of this relationship. In the model microtubules are seeded on the cell periphery, grow stochastically to capture dynamic instability (as in [122]), and follow geometric interaction rules between microtubules and cell boundaries upon collision (as in [67]).

One of the unexpected findings of the work was that the dependencies between microtubule alignment and cell eccentricity were exactly the same in two tissues where the microtubule dynamics is known to be different: pupal wing epithelium and embryonic epidermis. In the former, the microtubule growth speed is 0.15 μm/sec, and in the latter 0.27 μm/sec [22, 143]. Given the agreement between the *in silico* model and experiments in two different tissues, we hypothesized that the same microtubule organisation can be achieved under different conditions, ensuring robustness of intracellular transport and cellular functions.

In this chapter, we confirm an extreme robustness of microtubule self-organisation by both exploring parameter sensitivity of microtubule organisation using our *in silico* model, and altering microtubule dynamics and stability in *Drosophila* embryos. We start in Section 2.2.1 with a simple geometric *hairyball* model that accurately predicts the microtubule self-organisation, but does not explain the origin of self-organisation since it does not include microtubule dynamics. In Section 2.2.2 our stochastic simulations, which explore the large parameter space of microtubule dynamics parameterisations, suggest that microtubule self-organisation is robust. Our collaborator confirms this robustness *in vivo* via genetic manipulations in Section 2.3.1. In Section 2.2.3 we build a minimal probabilistic model that uncovers that the simple mathematical reason for robustness is the separation of time-scales of microtubule dynamics. It shows that details of microtubule dynamic instability are irrelevant for microtubule self-organisation within their biologically relevant ranges, and that only biological parameter beyond cell shape that affects microtubule alignment is the minus-end density. In Section 2.4.1 we obtain these two biological parameters from data and accurately predict the experimental results. We finish in Section 2.5 with the discussion.

2.2 Mathematical models

2.2.1 A simple geometric model accurately predicts *in vivo* microtubule alignment.

Cells of *Drosophila* epidermis elongate during the stages 12-15 of embryonic development, changing their eccentricity from 0.7 to 0.98 (Figure 2.1A and [58]). As cells elongate, initially randomly oriented microtubules become gradually aligned [58]. The simplest thought experiment to visualise how cell elongation translates

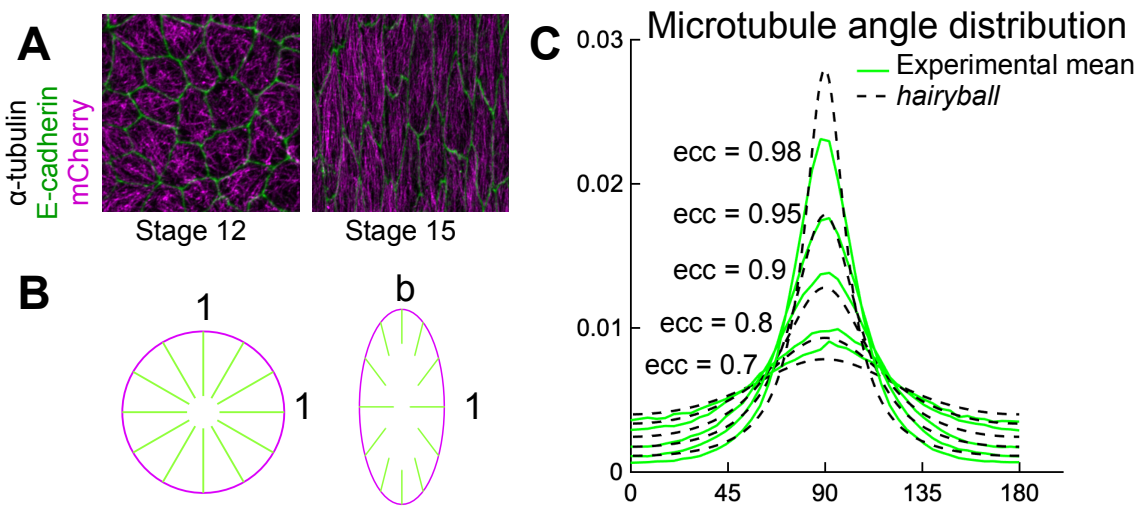

Figure 2.1: (A) *Drosophila* epithelial cells elongate between the stages of development 12 and 15, during which the microtubules become more organised. Duration of embryonic development in 25^{o}C for stages 12, 13, 14, 15 is approximately 120, 60, 60, 100 minutes respectively [48]. (B) Stretching a circular cell by a factor b deforms the initially uniform microtubule angle distribution into the *hairyball* distribution (2.1). (C) The experimental microtubule angle distribution (green) and the *hairyball* (2.1) (dashed black) are in good agreement up to eccentricity of 0.95.

into microtubule alignment is the following. Imagine a "hairy" unit-ball on the (x, y) plane, where "hairs" are microtubules. Turn it inside out (Figure 2.1B). The microtubules are randomly pointing inside the ball, representing absence of microtubule alignment in non-elongated cells; at each microtubule minus-end (*seed*) on the cell boundary, the mean microtubule direction is normal to the cell boundary. Stretching this cell uniformly in the y-direction by a factor b results in an ellipse with eccentricity $e(b) = \sqrt{1 - b^{-2}}$. The seed position will move proportionally to deformation, whereas the filament direction will point towards the cell center and its length will remain unaltered. Mathematically, the distribution $\rho(\theta)$ of microtubule angles $\theta \in [0, \pi]$ changes from the uniform $\rho(\theta) = 1/\pi$ to the angle distribution we call *hairyball* distribution, $\rho_{HB}(\phi)$, which is the inverse Jacobian of the stretching mapping $F : \theta \to \phi$, $\theta, \phi \in [0, \pi]$, given by $\tan(\phi(\theta)) = b \tan(\theta)$. Upon stretching a circular cell by a factor of $b > 1$ in one direction into an ellipse with eccentricity $e = \sqrt{1 - 1/b^2}$, the angles θ with uniform distribution $\rho(\theta) = 1/\pi$ are mapped to the angles ϕ with the distribution $\rho(\phi)$ such that $\rho(\theta) = J\rho(\phi)$, where J is the Jacobian

of the stretching map. Since $\rho(\theta) = const$,

$$\rho_{HB}(\phi) = \frac{1}{M}\frac{1}{\sin^2\phi + b^2\cos^2\phi}, \quad \phi \in [0, \pi], \tag{2.1}$$

where M is the normalization constant. This result gives a surprisingly good agreement with the experiment (Figure 2.1C), especially considering that this model does not take into account any of the underlying biological processes, e.g. microtubule dynamics. The *hairyball* angle distribution (2.1) is valuable as a short cut in the analysis of biological data and for parameterisations of microtubule angle distribution. However, there is a need to develop a more detailed mathematical model which includes parameterisation of the physical characteristics of microtubules to understand what controls their alignment. To do this we first explore the large parameter space using stochastic simulations.

2.2.2 Stochastic simulations demonstrate robustness of the microtubule self-organisation for a wide range of parameter values.

We now explore *in silico* how the microtubule self-organisation depends on the parameterisation of individual microtubule dynamics and their interactions, as individual microtubule dynamics and rigidity can vary significantly between organisms and is sensitive to the organism environment. We use an individual based model because we want to track the number of individual microtubules for an exact comparison to the experimental data available. The modelling framework allows for a degree of flexibility in terms of the modelling assumptions as we can easily change the microtubule interaction rules. We keep the cell shape fixed and the density of microtubule minus-ends on the cell boundary uniform, as *in vivo* these changes take hours comparing to order of 15 seconds required for a microtubule to grow the length of a cell and to order of minutes required for the microtubule network statistics to stabilize [58]. A sensitivity analysis enables us to see how variations in parameters affect the modelling results; if a parameter is sensitive then its small perturbation will lead to big changes in the results. We carry out a sensitivity analysis to understand which parameters in our model of microtubule dynamics affects the microtubule self-organisation measure of microtubule angle distribution.

To capture the dynamic instability, we model microtubules as follows (see Fig-

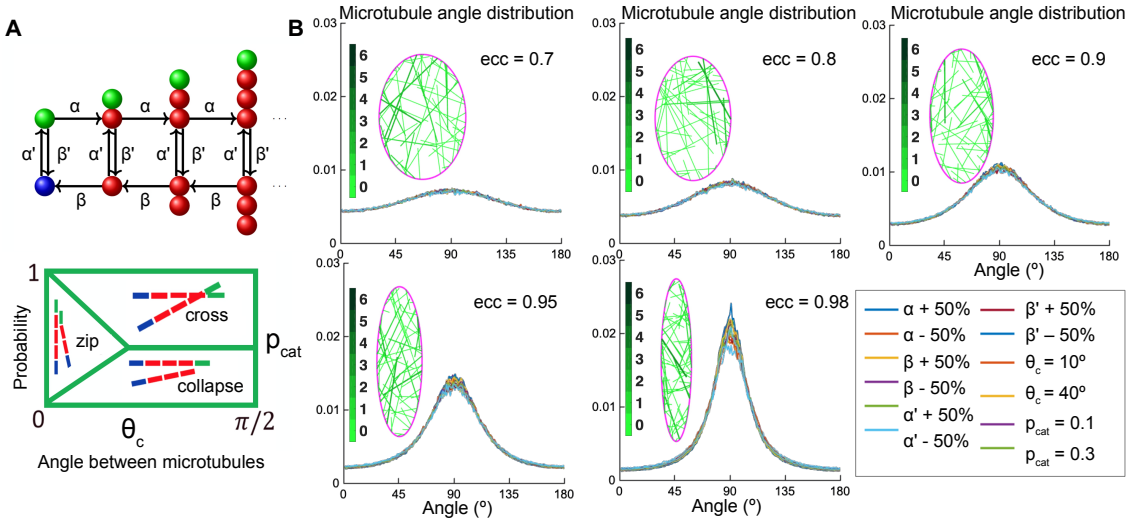

Figure 2.2: (A, top): Markov chain: microtubule grows from the seed (*blue*) at the rescue rate α', polymerises at the rate α if it is stable with a T.GTP cap (*green*), undergoes catastrophe β', depolymerises at the rate β, and can regain the T.GTP cap with the rescue rate α'. (A, bottom): the angle-dependent probabilities of microtubule interaction scenarios with the critical angle of zipping θ_{crit} and the probability of catastrophe p_{cat}. (B) Sensitivity analysis of the microtubule angle distribution. Left: Snapshots of zipping simulations (2.2) in cells of different eccentricities (*magenta*). Interacting microtubules form bundles, the colour bar indicates the number of microtubules in a bundle. Right: The microtubule angle distributions computed using (2.2) do not vary significantly in a wide parameter range, suggesting robustness of the microtubule self-organisation. The distributions are shown for the variations of $(\alpha, \beta, \alpha', \beta')$ as compared to $(1000, 3500, 4, 1)$, θ_c angle of zipping, and different values of the probability of catastrophe p_{cat}. The default parameters are given in Table 2.1.

ure 2.2A). Since the microtubule width ($24nm$) is much smaller than the typical cell size ($2 - 10\mu m$) [22], we model them as 1D filaments. They are composed of equal length segments, representing microtubule dimers, whose dynamics is governed by a continuous time Markov chain (see Figure 2.2A, [122, 58]). The microtubule grows (*polymerises*) at the rate α, and shrinks (*depolymerises*) at the rate $\beta > \alpha$; the *rescue* rate of switching from depolymerising to polymerising state α'; and the *catastrophe* rate of the reverse switching is β'. The rates of microtubule polymerisation and depolymerisation are kept constant, as we assumed that the concentration of tubulin did not vary significantly in the experiment. We set the same rescue rate at the *seed* state as from any non-zero length state, because in the epithelial cells of the

Drosophila embryo, the minus ends are fixed on the cell boundary. Finally, while the condition $\beta'\beta - \alpha'\alpha > 0$ is required for microtubules in unbounded domains to have a finite expected length [122], it is not necessary in our case, as the microtubules growth is often arrested by the collision with the cell boundary (see Section 2.5).

The self-assembly of microtubules follows a Markov Chain [106, 89, 55] of three distinct states, similar to [122, 21]. If the microtubule is in initial state (blue sphere) it can start self-assembly as it moves to a growing state of chain length one with probability 1. Further, if it is in the polymerising state, denoted by $X_{n,1}$ where $n \in \mathbb{Z}_{>0}$ signifies the number of dimers inside the inner chain, it can either grow by one tubulin dimer in its chain with probability $\alpha/(\alpha + \beta')$ or it can change to the corresponding shrinking state with probability $\beta'/(\alpha+\beta')$. Finally, if the microtubule is in the dissociating state, denoted by $X_{n,0}$ where $n \in \mathbb{Z}_{>0}$ is the number of dimers, then it can either shrink by one tubulin length with probability $\beta/(\alpha' + \beta)$ or change to a growing state with probability $\alpha'/(\alpha' + \beta)$.

We can construct the following transition matrix for the system

$$
\begin{array}{c}
 \\
X_{0,0} \\
X_{0,1} \\
X_{1,0} \\
X_{1,1} \\
X_{2,0} \\
X_{2,1} \\
X_{3,0} \\
\dots
\end{array}
\begin{array}{c}
\begin{array}{cccccccc} X_{0,0} & X_{0,1} & X_{1,0} & X_{1,1} & X_{2,0} & X_{2,1} & X_{3,0} & X_{3,1} \end{array} \\
\begin{pmatrix}
0 & 1 & 0 & 0 & 0 & 0 & 0 & 0 \\
\frac{\beta'}{\alpha+\beta'} & 0 & 0 & \frac{\alpha}{\alpha+\beta'} & 0 & 0 & 0 & 0 \\
\frac{\beta}{\alpha'+\beta} & 0 & 0 & \frac{\alpha'}{\alpha'+\beta} & 0 & 0 & 0 & 0 \\
0 & 0 & \frac{\beta'}{\alpha+\beta'} & 0 & 0 & \frac{\alpha}{\alpha+\beta'} & 0 & 0 \\
0 & 0 & \frac{\beta}{\alpha'+\beta} & 0 & 0 & \frac{\alpha'}{\alpha'+\beta} & 0 & 0 \\
0 & 0 & 0 & 0 & \frac{\beta'}{\alpha+\beta'} & 0 & 0 & \frac{\alpha}{\alpha+\beta'} \\
0 & 0 & 0 & 0 & \frac{\beta}{\alpha'+\beta} & 0 & 0 & \frac{\alpha'}{\alpha'+\beta} \\
\dots & \dots & \dots & \dots & \dots & \dots & \dots & \dots
\end{pmatrix}
\end{array}
\begin{array}{c}
 \\
\dots \\
\dots \\
\dots \\
\dots \\
\dots \\
\dots \\
\dots \\
\dots
\end{array}
, \qquad (2.2)
$$

but cannot obtain any information on the states being transient or recurrent so we use numerical simulations to model the microtubule behaviour.

We parameterise the angle-dependent microtubules interaction with other microtubules and cell boundaries based on the known interactions in plants [67] and *Drosophila* cells (Figure 2.2B, [58, 39]). Upon encountering another microtubule at an angle θ, for angles larger than a critical angle ($\theta \geq \theta_c$), the microtubule undergoes a catastrophe with probability p_{cat}, and crosses the microtubule otherwise; for smaller angles ($\theta \leq \theta_c$), the microtubule collapses with probability $p(\theta) = \frac{\theta}{\theta_c} p_{cat}$,

crosses with probability $p(\theta) = \frac{\theta}{\theta_c}(1 - p_{cat})$, and otherwise grows parallel to the existing microtubule (zipping effect, and the microtubule is said to *zip*). Upon reaching a cell boundary at an angle ($\theta \leq \theta_c$), the microtubule zips along the cell boundary with probability $p(\theta) = 1 - \frac{\theta}{\theta_c}$, and depolymerises otherwise [58].

The parameter space of this simple geometrical model allows us to investigate a broad range of biologically relevant microtubule dynamics scenarios: in an organism, the dynamic instability parameters (α, α', β, β') are linked to the expression of particular plus- and minus-end binding proteins and external factors as the organism temperature, while the interaction parameters $\theta_{critical}$ and p_{cat} are linked to how properties of the present cross-linking and motor proteins and microtubule rigidity (which is temperature dependent) affect microtubule interaction [87].

The simulations were run on cells of the eccentricities $(0.7, 0.8, 0.9, 0.95, 0.98)$, mirroring the experimental setup (Section 2.3). We demonstrate in Section 2.5 that the average cell shape is an ellipse, and hence the stochastic simulations are run on fixed elliptical cells. Along the cell boundary, discretized with 180 points, 200 microtubule seeds are placed uniformly. This high seed density (1 microtubule per $6 - 21nm$) is not unrealistic, as at any point in time due to the choices of the Markov chain rates, only about 30% of all the microtubules have non-zero length. The critical angle of the microtubule interaction $\theta_{critical}$ was varied between 0 and 40 degrees (10 and 40 degrees are reported in Figure 2.1B), and the probability of catastrophe p_{cat} was varied in the range $(0.01, 0.1, 0.2, 0.3)$ (0.1 and 0.3 reported in Figure 2.1B). We imposed that if a microtubule zipping along a cell boundary reaches the tip of the ellipse, it undergoes catastrophe. This mirrors the scenario *in vivo* that due to their high stiffness [56], microtubules undergo catastrophe upon reaching an acute cell corner (Figure 2.1A). At the start of each experiment all microtubule lengths were set to zero.

Here we link these parameters to their dimensional equivalents. The typical observed microtubule growth speed, α_{dim}, is $0.15\mu m/sec$ [58]. We non-dimensionalise our system by stating that

$$\alpha_{dim,speed} = \alpha_{non-dim} \times d \times R,$$

where $d = 8.2nm$ is the height of one dimer. We use $\alpha_{non-dim} = 1000$ as the non-dimensional base growth rate and $\alpha_{dim} = 0.15\mu m/sec$ to find that $R = 0.0183sec^{-1}$.

Parameter	Default parameter $(non-dim)$	Dimensional equivalent (dim)
α	1000	$0.15\mu m/s$
β	3500	$0.52\mu m/s$
α'	4	$0.07316s^{-1}$
β'	1	$0.01829s^{-1}$
p_{cat}	0.01	–
θ_c	30^o	–

Table 2.1: Summary of key parameters describing microtubule dynamics in our models.

The microtubule shrinking rate is given by

$$\beta_{dim,speed} = \beta_{non-dim} \times d \times R = 0.52\mu m/sec,$$

where $\beta_{non-dim} = 3500$. Next we consider the microtubule rescue and catastrophe rates which do not depend on the dimer heights. The microtubule rescue rate is given by

$$\alpha'_{dim} = \alpha'_{non-dim} \times R = 0.07316sec^{-1},$$

where $\alpha'_{non-dim} = 4$. The microtubule catastrophe rate is given by

$$\beta'_{dim} = \beta'_{non-dim} \times R = 0.01829sec^{-1},$$

where $\beta'_{non-dim} = 1$. All the experiments were run to the non-dimensional time $T = 10$, which corresponds to $T \div R = 550$ seconds. We binned the microtubule angles with respect to the horizontal in 180 bins of the size of one degree, and averaged these histograms in the last 2.5 non-dimensional time-units, which corresponds to 250 points.

In our research we chose the base parameters and varied them such that the base rates were tested in the range from half to double that of the base-rate. This gave the following dimensional range of parameters: the microtubule growth $\alpha_{dim,speed} = 0.075 - 0.225\mu m/sec$; shrinking $\beta_{dim,speed} = 0.26 - 0.78\mu m/sec$; rescue $\alpha'_{dim} = 0.0366 - 0.1097sec^{-1}$; and catastrophe $\beta'_{dim} = 0.0091 - 0.0274sec^{-1}$. *In vivo*, the parameters of microtubule dynamic instability widely depend on the cell type. The reported ranges of the rates of growth are $0.05-0.5\mu m/sec$; shrinking $0.13-0.6\mu m/sec$; rescue $0.01 - 0.17sec^{-1}$; and catastrophe $0.003 - 0.08sec^{-1}$ [22, 95, 131] and we were

close to representing sample points in the biologically relevant range. The default parameters are summarised in Table 2.1. The numerical simulations are performed in Matlab [108] and full details of the code are provided in [58].

The simulations give an unexpected result (see Figure 2.2B) that in this large parameter range, the microtubule angle distribution varied only slightly, suggesting that in this model the microtubule self-organisation is robust and does not depend on the details of dynamical instability and microtubule interaction parameterisation. This suggests that the *in vivo* system could be similarly robust with respect to variations in internal and external environment, the hypothesis we test in the next section.

2.2.3 Analytical model shows that microtubule self-organisation depends on cell geometry and seeds distribution.

Given that the microtubule angle distribution *in silico* only weakly depends on microtubule interaction, we propose a minimal mathematical model with non-interacting microtubules, which is analytically tractable. Here, independent microtubules, cross upon reaching another one, and fully depolymerise upon reaching a cell boundary. Their averaged long-time behaviour is the average of 1D behaviours of individual microtubules growing from different positions on the cell boundary.

Our model setup is as follows (Figure 2.3A). Consider a convex 2D cell with the boundary parameterised by the arclength-coordinate ζ increasing in a counterclockwise direction. From microtubule *seeds* distributed with density $\rho(\zeta)$ on the cell boundary, the microtubules grow into the cell interior at an angle θ to the tangent $T(\zeta)$ to the cell boundary, making the angle ϕ with respect to the horizontal. Note that the cell shape is fully determined by the function $a(\zeta, \theta)$ – the length of a cross-section that starts at ζ at an angle θ with respect to the boundary. When $a(\zeta, \theta)$ is considered as a function of (ζ, ϕ), we denote it by $\tilde{a}(\zeta, \phi)$ to avoid confusion. Microtubules undergo dynamic instability by switching between the states of growth, shrinking, catastrophe and rescue at the rates α, β, β', and α' respectively. After fully depolymerising, they regenerate at the rate α' from the same seed but in a new direction at an angle θ taken from a uniform distribution on $[0, 180]$. Thus, on a large fixed time interval $t \in [0, T]$ a microtubule undergoes a large number n of growth and shrinkage lifetimes separated by periods of average duration $1/\alpha'$ when it has zero length.

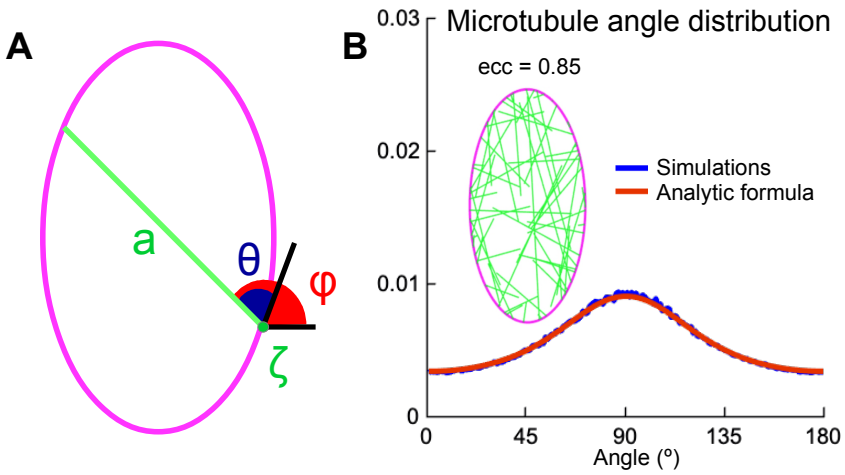

Figure 2.3: (A) Analytical model setup: the cell shape is parameterised by the arclength ζ along the cell boundary, where at the seed ζ a straight microtubule grows at an angle θ with respect to the tangent line to the cell boundary at ζ, with a maximum length a at the opposite cell side. (B) Left: snapshot the simulations with non-zipping independent microtubules for cells of eccentricity 0.85. Right: agreement between the microtubule angle distributions predicted by the analytical model (2.17) (*red*) and the stochastic simulations (2.2) (*blue*). The default parameters are given in Table 2.1.

The first quantity of interest is the microtubule mean survival time. Since in the *in vivo* and *in silico* experiments, the microtubule angle distribution is length-weighted, we include the general case of weighting the mean survival time by a function $\gamma(x)$ of microtubule length x i.e. we are interested in the sum of microtubule lengths pointing in a given direction and not just the time they spend in a given direction. Then the equations for the mean survival time $f(x)$ and $g(x)$ of respectively the polymerising and depolymerising microtubule of length x are

$$f(x) = \underbrace{(1-\beta' dt) f(x+\alpha dt)}_{\text{grow}} + \underbrace{\beta' dt g(x)}_{\text{switch}} + \underbrace{\gamma(x(t))dt}_{\text{weighted time increment}}, \tag{2.3}$$

$$g(x) = \underbrace{(1-\alpha' dt) g(x-\beta dt)}_{\text{shrink}} + \underbrace{\alpha' dt f(x)}_{\text{switch}} + \underbrace{\gamma(x(t))dt}_{\text{weighted time increment}}, \tag{2.4}$$

where dt is a small time-increment. Expanding (2.3-2.4) we obtain

$$f(x) = f(x) - \beta' dt f(x) + \alpha dt f'(x) - \beta' \alpha dt^2 f'(x) \ldots + \beta' dt g(x) + \gamma(x) dt \tag{2.5}$$

$$g(x) = g(x) - \beta dt g'(x) - \alpha' dt g(x) + \alpha' \beta dt^2 g(x) \ldots + \alpha' dt f(x) + \gamma(x) dt \,. \tag{2.6}$$

Next we neglect terms of second and higher order in dt and obtain that $f(x)$ and $g(x)$ are governed by

$$\frac{d}{dx}f(x) = \frac{\beta'}{\alpha}(f(x) - g(x)) - \frac{\gamma(x)}{\alpha}, \tag{2.7}$$

$$\frac{d}{dx}g(x) = \frac{\alpha'}{\beta}(f(x) - g(x)) + \frac{\gamma(x)}{\beta}. \tag{2.8}$$

Their difference $h(x) = f(x) - g(x)$ satisfies

$$\frac{d}{dx}h(x) = ph(x) - q\gamma(x), \tag{2.9}$$

where $p = \frac{\beta'}{\alpha} - \frac{\alpha'}{\beta}$ and $q = \frac{1}{\alpha} + \frac{1}{\beta}$. Finally, we assume that $g(a) = 0$, i.e. once the microtubule reaches the cell boundary at the length $a(\zeta, \theta)$, it quickly depolymerises, and for a zero-length microtubule $g(0) = 0$, and hence $h(0) = f(0)$. Note that the only quantity of interest is $f(0) = h(0)$, since it is the lifetime of a microtubule when it starts in a growing state with zero length. We first use $\gamma(x) = 1$ to find the solution for the not-weighted mean survival time, denoted by $f_{nw}(x)$. We integrate (2.9) with $\gamma(x) = 1$ to obtain that

$$h(x) = \frac{qe^{-px}}{pe^{-px}} + \frac{C_1}{e^{-px}}\,. \tag{2.10}$$

We now use the boundary condition $g(a) = 0$ to find that $C_1 = \frac{-q}{p}e^{-pa}$ and find that

$$f_{nw}(0) = h(0) = \frac{q}{p}(1 - e^{-pa}). \tag{2.11}$$

To find the length-weigthed mean survival time we now use $\gamma(x) = x$ and integrate (2.9) to find that

$$h(x) = \frac{q}{p^2}(px + 1) + \frac{C_2}{e^{-px}}\,. \tag{2.12}$$

Again, we use the boundary condition $g(a) = 0$ to find that $C_2 = -\frac{q}{p^2}(pa + 1)e^{-pa}$ and find the solution

$$f_w(0) = h(0) = \frac{q}{p^2}\left(1 - e^{-pa}(1 + pa)\right). \tag{2.13}$$

For each microtubule seed ζ, the average time between any two re-growths of a

microtubule is the sum of the averaged weighting time $1/\alpha'$ and the average of the non-weighted lifetime over all the growth angles θ

$$\frac{T}{n} \approx \left(\frac{1}{\alpha'} + \frac{1}{\pi}\int_0^\pi f_{nw}(0)\right) = \left(\frac{1}{\alpha'} + \frac{q}{\pi p}\int_0^\pi (1 - e^{-a(\zeta,\theta)p})d\theta\right). \tag{2.14}$$

Then the average number of lifetimes with direction $(\phi, \phi + \delta\phi)$ with respect to the horizontal is $n\delta\phi/\pi$, and that their contributions to the length-integral is

$$f_w(0)n\delta\phi/\pi = \frac{q}{p^2}\Big(1 - e^{-\tilde{a}(\zeta,\phi)p}(1 + \tilde{a}(\zeta,\phi)p)\Big)n\delta\phi/\pi. \tag{2.15}$$

Substituting (2.14) in (2.15) we obtain

$$\frac{\frac{q}{p^2}\Big(1 - e^{-\tilde{a}(\zeta,\phi)p}(1 + \tilde{a}(\zeta,\phi)p)\Big)}{\frac{1}{\alpha'} + \frac{q}{\pi p}\int_0^\pi (1 - e^{-a(\zeta,\theta)p})d\theta} T\delta\phi/\pi. \tag{2.16}$$

Here we denote the microtubule length as either $a(\zeta,\theta)$ and $\tilde{a}(\zeta,\phi)$ to avoid confusion depending on their arguments. Finally, the length-weighted microtubule angle distribution is given by integrating (2.15) over the cell boundary, along which the microtubules are distributed with density $\rho_{seed}(\zeta)$

$$\rho(\phi) \;=\; \frac{1}{M}\int \frac{1 - e^{-\tilde{a}(\zeta,\phi)p}(1 + \tilde{a}(\zeta,\phi)p)}{1 + \frac{q\alpha'}{\pi}\int_0^\pi \frac{1-e^{-a(\zeta,\theta)p}}{p}d\theta}\rho_{seed}(\zeta)d\zeta, \tag{2.17}$$

where M is the normalization constant. This analytical prediction matches the stochastic simulations (see Figure 2.3B).

The dependency of the resulting microtubule angle distribution on the biological rates reduces to two parameters

$$p = \frac{\beta'}{\alpha} - \frac{\alpha'}{\beta}, \quad \frac{q\alpha'}{\pi} = \frac{\alpha'}{\pi}\left(\frac{1}{\alpha} + \frac{1}{\beta}\right). \tag{2.18}$$

If both are small, $|p| \ll 1$ and $\frac{\alpha'}{\pi}\left(\frac{1}{\alpha} + \frac{1}{\beta}\right) \ll 1$, as is always observed in biological systems (see above), the microtubule angle distribution formula can be significantly simplified. In particular, for small p the distribution (2.17) reduces (using exponential

expansion) to

$$\rho(\phi) = \frac{1}{M} \int \frac{\tilde{a}^2(\zeta, \phi)}{1 + \frac{q\alpha'}{\pi} \int_0^\pi a(\zeta, \theta) d\theta} \rho_m(\zeta) d\zeta \tag{2.19}$$

to leading order, and to

$$\rho(\phi) = \frac{1}{M} \int \tilde{a}^2(\zeta, \phi) \rho_m(\zeta) d\zeta, \tag{2.20}$$

when, in addition, $\frac{q\alpha'}{\pi} \ll 1/\int_0^\pi a(\zeta, \theta) d\zeta$. This becomes exact in the limit of deterministic microtubules ($\beta = \infty$, $\beta' = 0$). Note that while p is required to be non-negative in models of microtubules on an infinite line [122], our setup does not have this restriction, as the microtubule lifetimes $f_w(0)$ and $f_{nw}(0)$ are positive even for negative p.

Furthermore, the analytical microtubule angle distribution (2.17) is independent of the multiplicative change in the minus-end density $\rho_m(\zeta)$, which would be absorbed into the normalization constant M. Only non-trivial changes to the density of minus-ends that vary along the cell boundary affect the microtubule angle distribution.

It is required that $\alpha' \ll \alpha$ and $\alpha' \ll \beta$ for the second parameter in (2.18) to be small, and $\beta' \ll \alpha$ for the first one to be small as well. Therefore, the microtubule angle distribution depends only on the cell geometry and the minus-end distribution, and the underlying reason for that is the separation of time-scales in microtubule dynamics: the rates of polymerization and depolymerization are much higher than those of catastrophe and rescue, which is always observed *in vivo*.

2.3 Experimental validation

The main part of the genetic manipulations involves overexpression of certain proteins which alter microtubule dynamics (described below). Overexpression relies on increasing the amount of a specific protein using an appropriate promoter. A promoter is a genetic sequence which encodes which proteins should be produced. For example to overexpress EB1-DN (as mentioned below) a promoter is introduced so that the cells make more EB1-DN which in turn increases the catastrophe rate as the microtubules are bound to this and cannot assemble.

2.3.1 *In vivo* manipulations of microtubule dynamics and stability alter microtubule density but not alignment.

Next, our collaborator sought to test *in vivo* the robustness of microtubule self-organisation predicted by the model. To this end, she examined how changes in microtubule dynamics and stability affect organisation of subapical microtubules in cells of *Drosophila* embryonic epidermis. These microtubules are confined to 1 μm-deep subapical plane in columnar epidermal cells, and become progressively aligned as the cell elongates during the embryo development [58]. Using genetic manipulations she could either increase the catastrophe rate β', simultaneously increase the catastrophe rate β' and shrinkage rate β, or reduce the number of seeds, therefore reducing density of the network and thus encounters and zipping between microtubules. In particular (see Figure 2.4A), β' was increased by overexpressing a dominant-negative variant of End Binding protein 1 (EB1-DN) [22], a form which increases the number of catastrophes without changing other parameters of microtubule dynamics, or β' and β were both increased by overexpressing the protein Spastin, which severs and disassembles microtubules [22, 132, 95]. These proteins were overexpressed using UAS-Gal4 system, in which the Gal4 protein expressed from a tissue-specific promoter induces overexpression of the protein of interest by binding the Upstream Activating Sequence (UAS) enhancer [19]. Specifically, *paired*::Gal4 was used, which drives expression in stripes along the dorsal-ventral axis of embryos. Finally, the number of seeds was reduced using null mutation of minus-end capping protein Patronin [113]. In this instance mild Spastin overexpression was used, so that few microtubules remain. Overexpression of a CD8-Cherry protein, which does not alter microtubules, was used as a control.

The above manipulations and altered organisation of microtubule network in cells were quantified by obtaining images of microtubules stained with antibody recognizing α-tubulin, and analysed on a cell-by-cell basis. From these images two types of information were obtained about microtubule organisation, namely about density and alignment of the network. First, to determine how the manipulations altered the amount of microtubules in cells, by the percent of the cell area covered by α-tubulin signal as a proxy for the number of microtubules in cells was quantified. Second, to determine if the genetic manipulations altered the microtubule alignment the direction and magnitude of change of the α-tubulin signal at each position within the cell was measured and produced the microtubule direction distributions.

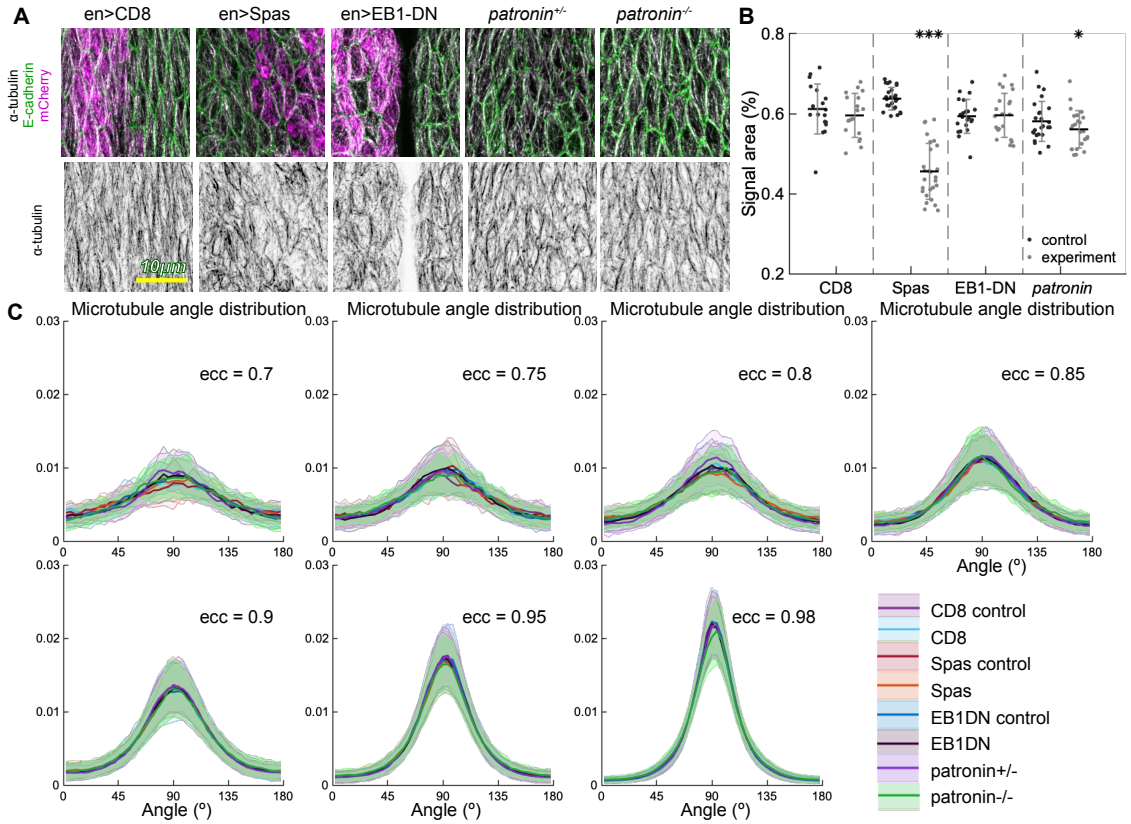

Figure 2.4: Changes to microtubule dynamics and stability do not affect their alignment. (A) Apical view of epidermis from control embryos and with altered microtubules. Left-to-right: embryos with CD8-Cherry (control), Spastin (Spas), and EB1-DN expressed using *paired*::Gal4, heterozygous *Patronin*$^{-/+}$, and homozygous *Patronin*$^{-/-}$ embryos. Cells expressing CD8-Cherry and EB1-DN are visualised by direct fluorescence of mCherry directly fused to respective proteins, whereas cells expressing Spastin are visualised by coexpression of CD8-Cherry (*magenta*, top raw). Cell outlines were visualised by immunostaining against E-cadherin (*green*, top raw), and microtubules by immunostaining against α-tubulin (*white*, top raw; *black*, bottom raw). Embryos were imaged across all developmental stages between stage 12 and 15. Scale bar - 10 μm. (B) Quantification of microtubule density in each genotype. Internal controls (cells not expressing *paired*::Gal4) were used for CD8-Cherry, Spastin, and EB1-DN overexpression. For *Patronin*, heterozygous and homozygous embryos were compared. *** - p-value$<$ 0.0001, * - p-value$<$ 0.05 in comparison to respective control. (C) The microtubule angle distributions for each eccentricity ($\pm$ 0.025) do not significally differ between all genotypes and relatively to controls.

To capture a wide range of eccentricities embryos at different stages of development were used during the developmental window when the epidermal cells progres-

sively elongate from eccentricities around 0.7 to 0.98 (stages 12 through 15). Overexpression of Spastin reduced α-tubulin signal area in comparison to both neighbouring cells, which did not express *paired*::Gal4, and control cells expressing CD8-Cherry (both p-values< 0.0001, Figure 2.4A-B), consistent with its function. Similarly, the α-tubulin signal area was reduced in embryos homozygous for *Patronin*$^{-/-}$ in comparison to heterozygous siblings (p-value$= 0.04$, Figure 2.4A-B), consistent with its role in protecting microtubule minus-ends. Overexpression of EB1-DN did not change the area covered by α-tubulin signal per cell (p-value$= 0.98$, Figure 2.4A-B), which can be explained by either weaker expression of *paired*::Gal4 in comparison to *engrailed*::Gal4 using which the phenotype was reported in the past [22], or lower amounts of Gal4 at earlier developmental stages than stage 15 used before [22]. The microtubule angle distributions for each eccentricity (binned at a particular eccentricity $\pm$ 0.025) did not significally differ between all genotypes and relatively to controls (Figure 2.4C), which supports robustness of microtubule self-organisation despite different microtubule dynamics and amount.

Although the above manipulations did not change the microtubule alignment, only two of them affected microtubule density, and the changes in the density were small. To prove that the microtubule alignment is indeed robust to changes in dynamics and density, an increase in the effects of our genetic manipulations was needed. Promoters, which are used to drive Gal4 expression, differ in the amounts of Gal4 and respectively the protein of interest, which are produced. To this end, a stronger *engrailed*::Gal4 driver was used to overexpress EB1-DN and Spas. Additionally, amounts of protein expressed using UAS-Gal4 system increases with time, whereas when using mutant embryos, amounts of protein supplied from mothers in eggs, the maternal contribution, decreases with time as they cannot produce their own protein. Therefore,the focus was on the late developmental stage of *Drosophila* embryo development (stage 15). In this case the overexpression of both Spastin and EB1-DN reduced the area of α-tubulin signal in cells (p-values< 0.0001 and p-value$= 0.003$, respectively, Figure 2.5A-B), and the changes were more pronounced as in the case of *paired*::Gal4. Additionally, the area of α-tubulin signal was reduced in heterozygous *Patronin*$^{+/-}$ embryos in comparison to wild-type controls (p-value$= 0.02$, Figure 2.5A-B), and even further reduced in homozygous *Patronin*$^{-/-}$ embryos (p-values$= 0.0003$ and 0.002 in comparison to wild-type control and heterozygous siblings, respectively, Figure 2.5A-B). This result is consistent with the dose-dependent protection of the microtubule minus-ends by Patronin. The differ-

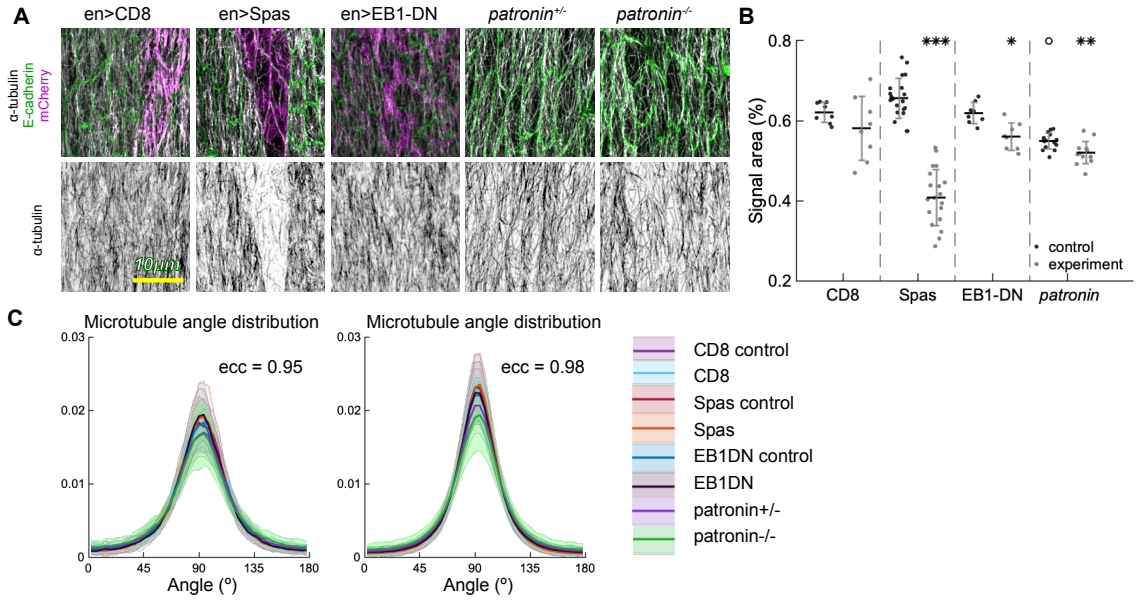

Figure 2.5: Changes to microtubule dynamics and stability also do not affect their alignment when strong *engrailed*::Gal4 driver is used. (A) Apical view of epidermis from conrtrol embryos and with altered microtubules. Left-to-right: embryos with CD8-Cherry (control), Spastin (Spas), and EB1-DN expressed using *engrailed*::Gal4, heterozygous *Patronin*$^{-/+}$, and homozygous *Patronin*$^{-/-}$ embryos. Cells expressing CD8-Cherry and EB1-DN are visualised by direct fluorescence of mCherry directly fused to respective proteins, whereas cells expressing Spastin are visualised by co-expression of CD8-Cherry (*magenta*, top raw). Cell outlines were visualised by immunostaining against E-cadherin (*green*, top raw), and microtubules by immunostaining against α-tubulin (*white*, top raw; *black*, bottom raw). Embryos were imaged at the stage 15 of embryonic development. Scale bar - 10 μm. (B) Quantification of microtubule density in each genotype. Internal controls (cells not expressing *paired*::Gal4) were used for CD8-Cherry, Spastin, and EB1-DN overexpression. For *Patronin*, heterozygous and homozygous embryos were compared. *** - p-value$<$ 0.0001, ** - p-value$<$ 0.001, * - p-value$<$ 0.01 in comparison to respective control; ^{o} - p-value$<$ 0.01 in comparison to CD8-Cherry control. (C) The microtubule angle distributions for each eccentricity ($\pm$0.025) do not significantly differ between all genotypes and relatively to controls.

ence between heterozygous *Patronin*$^{+/-}$ and wild type control observed here, but not when *paired*::Gal4 was used Figure 2.4A-B), might be due to use of narrower developmental time, which improves consistency in microtubule density between individual embryos and makes easier to detect small changes. Note, that *Patronin*$^{-/-}$ might have residual Patronin protein due to the maternal contribution. Despite greater changes

in microtubule density in this case, the microtubule angle distributions similarly did not significally differ between all genotypes and relatively to controls in this case Figure 2.5C).

2.4 Results

2.4.1 The analytical model accurately predicts microtubule-self organisation using experimental cell shape data and distribution of microtubule minus-ends

In order to validate our analytical model in its efficacy for prediction of microtubule organisation, the localization of microtubule minus-ends was determined. In the epidermal cells of *Drosophila* embryos, the subapical microtubules are acentrosomal and tend to grow from cell boundaries [81]. One of the best characterized proteins that protects microtubule minus-ends is Patronin [61]. Therefore, the distribution of Patronin was analysed in epithelial cells in the *Drosophila* embryonic epidermis using Patronin-YFP [113]. As expected, Patronin-YFP mostly localized at the cell boundaries with few speckles inside cells (Figure 2.6A). The distribution of Patronin-YFP was quantified at cell boundaries by measuring its asymmetry, namely the ratio of Patronin-YFP average intensity at dorsal-ventral borders and anterior-posterior borders (see materials and methods and [23]). The asymmetry of Patronin distribution $A(ecc)$ was a linear function of the cell eccentricity (Figure 2.6B), suggesting that Patronin becomes enriched at the dorsal-ventral boundaries as embryo develops and cells elongate. Additionally, when comparing boundaries in cells with similar eccentricities (Stage 15 embryos only), the intensity of Partonin-YFP was increasing with the border angle relatively to dorso-ventral axis of the embryo (Figure 2.6C).

To use this in our analytical model, we used least-squares to simultaneously fit the asymmetry data with a linear function of eccentricity, and the normalized intensity of Partonin-YFP with an exponential function of the cell border angle. We imposed a constraint that the asymmetry value at eccentricity at Stage 15 (eccentricity 0.98) is the same as the normalized intensity of Partonin-YFP at the border angle 90

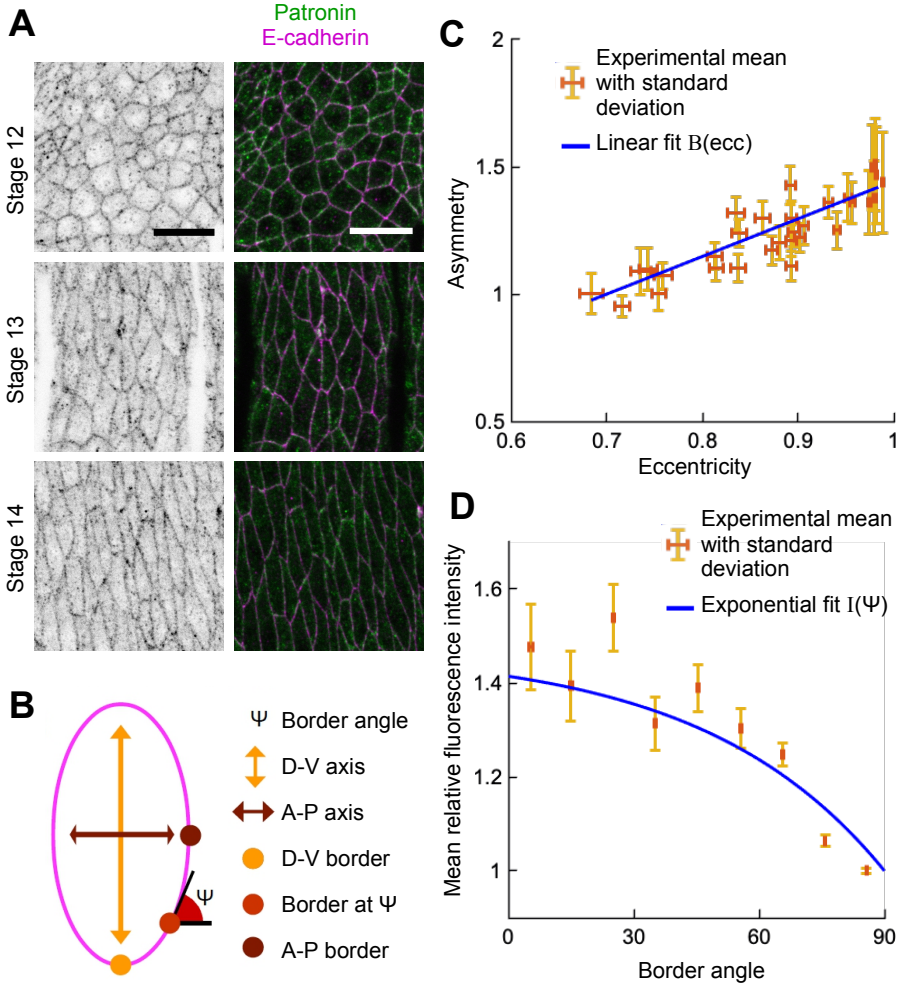

Figure 2.6: Localization of Patronin-YFP in the *Drosophila* embryonic epidermis. (A) Apical view of embryonic epidermis at stage 12 (top), 13 (middle), and 15 (bottom), visualized with Patronin-YFP (*grey*, left; *green*, right), and E-cadherin immuno-staining (*magenta*, right). Scale bar, 10 μm. (B) Schematic of a cell. (C) Asymmetry of Patronin-YFP localization increases linearly with eccentricity. Each dot represents average values of Patronin-YFP asymmetry and cell eccentricity in a single embryo. Error bars are SD. Solid line visualizes the linear fit of the form $B(ecc) = 1 + C_1(ecc - 0.7)/(0.98 - 0.7)$, $C_1 = 0.4144$. (D) Mean relative amounts of Patronin-YFP as a function of the border angle ψ in stage 15 (eccentricity 0.98) *Drosophila* embryonic epidermis, normalized by its value at the vertical long sides (0-10^o). Borders were binned at 10^o intervals relatively to embryonic anterior-posterior axis, and intensity was averaged for each bin (mean $\pm$ SD). The solid line represents the exponential fit for the intensity as $I(\psi) = 1 + (B(0.98) - 1)(1 - e^{-C_2(90-\psi)})/(1 - e^{-90C_2})$, $C_2 = 0.0231$.

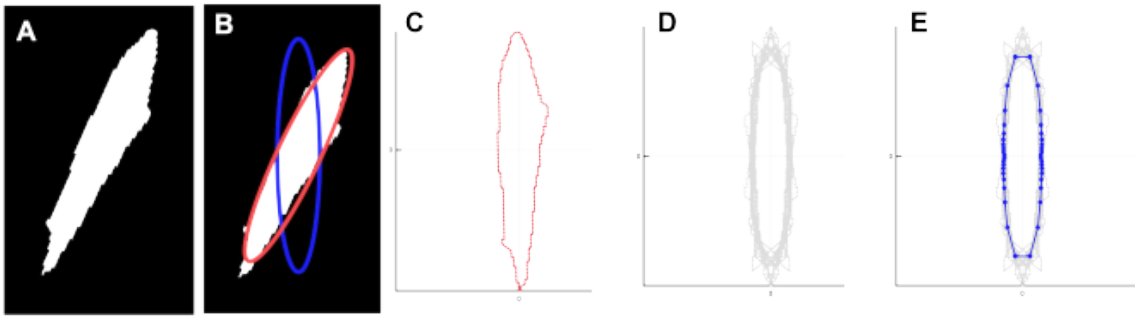

Figure 2.7: Schematic of finding the average shape from experimental cell shapes. (A) An experimental cell shape. (B) Singular value decomposition on top of experimental shape used to plot an ellipse with the major and minor axis plotted as the two eigenvectors used to describe the shape. Red ellipse includes rotation, blue ellipse shows the shape rotated so that the major axis lies at the y-axis. (C) Rotated and centred experimental cell shape with red dots showing evenly positioned points at the cell boundary. (D) Three experimental cell shapes rotated, centred and normalized by area. All points are reflected into positive (x,y) quadrant so that the cell is symmetric. (E) Three experimental cell shapes rotated, centred and normalized shown in grey and blue points show the average cell shape.

degrees. The resulting formula used in the analytical model is

$$Asymmetry(ecc, \psi) = 1 + C_1 \left(\frac{ecc - 0.7}{0.98 - 0.7} \right) \left(\frac{1 - \exp(-C_2(90 - \psi))}{1 - \exp(-90C_2)} \right), \quad (2.21)$$
$$C_1 = 0.4144, \quad C_2 = 0.0231,$$

where ψ is the cell border angle with respect to the horizontal.

We next sought to determine the average cell shape. In the tissue, each cell has a unique shape, and cells with same eccentricities may differ significantly in their geometry (Figure 2.8).

Therefore, to test and validate the analytical solution of microtubule self-organisation we generated masks of epithelial cells in the *Drosophila* embryonic epidermis, which provided us with coordinates of cell boundaries. To obtain the eccentricity of the cell given the cell boundary data, we use Singular Value Decomposition (SVD) as follows. We fill the cell shape with uniformly placed points with the density at least 1000 points in each direction (see Figure 2.7 A). Given the SVD of the resulting set of points, the eccentricity is computed as $ecc = \sqrt{1 - (a/b)^2}$, where $a < b$ are the singular values (illustrated by the use of ellipses in Figure 2.7 B). We divided all cell shapes

into groups by eccentricity ($ecc = 0.7 \pm 0.025, 0.8 \pm 0.025, 0.9 \pm 0.025, 0.95 \pm 0.025$ and 0.98 if $ecc > 0.975$). To compute the average cell shape for each eccentricity-group, we first re-centred the cell to have their centres of mass at the origin. We then rotated them so that they are elongated along the vertical axis (the direction of elongation is the first singular vector). Finally, we rescaled all the cells to have unit area (see Figure 2.7 C and D). All points for the cells were placed so that they lie in the first quadrant, i.e. we consider the absolute value of points (x_p, y_p). The average of distance to the cell boundary from the centre of mass in a particular direction traced the boundary of the averaged cell. We find the average cell shape by considering angle segments in this first quadrant i.e. we split our calculations so that we first find the mean of all points located in the first quadrant within an angle of 0^o to 10^o subtended from the origin and proceed to repeat the process with all other eight angle ranges e.g. 10^o to 20^o and so on. The corresponding average shape is calculated by mirroring the points into all other quadrants. Surprisingly, we found that the average cell shape for a given cell eccentricity is an ellipse (see Figure 2.8).

The resulting analytical microtubule angle distribution (2.17) computed for an elliptical cell using the fitted density of the microtubule minus-ends on the cell boundary (2.22) gives surprising agreement with experiment (see Figure 2.8A). Note that the analytical formula with the asymmetric microtubule-ends agrees better with the data than the one with uniform minus-end density. We use the L2 error to measure the difference between two distributions ρ_i and ρ_j defined by

$$L_2 \text{ error} = \sum_{k=1}^{n} ((\rho_i)_k - (\rho_j)_k)^2, \tag{2.22}$$

where n is the number of data points for the experimental distribution. The L_2 error for the experimental mean and the average of simulations with uniform seeding is 3.102×10^{-5} and the L_2 error for the experimental mean and the average of simulations with assymetric seeding is 7.835×10^{-6}. Finally, the *hairyball* distribution (2.1) gives a better agreement with the data up to eccentricity 0.95.

From this result we conclude that, on the one hand, our analytical model accurately predicts self-organisation of subapical microtubule arrays, and on the other hand, it clearly shows that the origin of robustness of the organisation in a wide range of microtubule behaviour regimes is the fact that this organisation only depends on the cell shape and distribution of microtubule minus-ends.

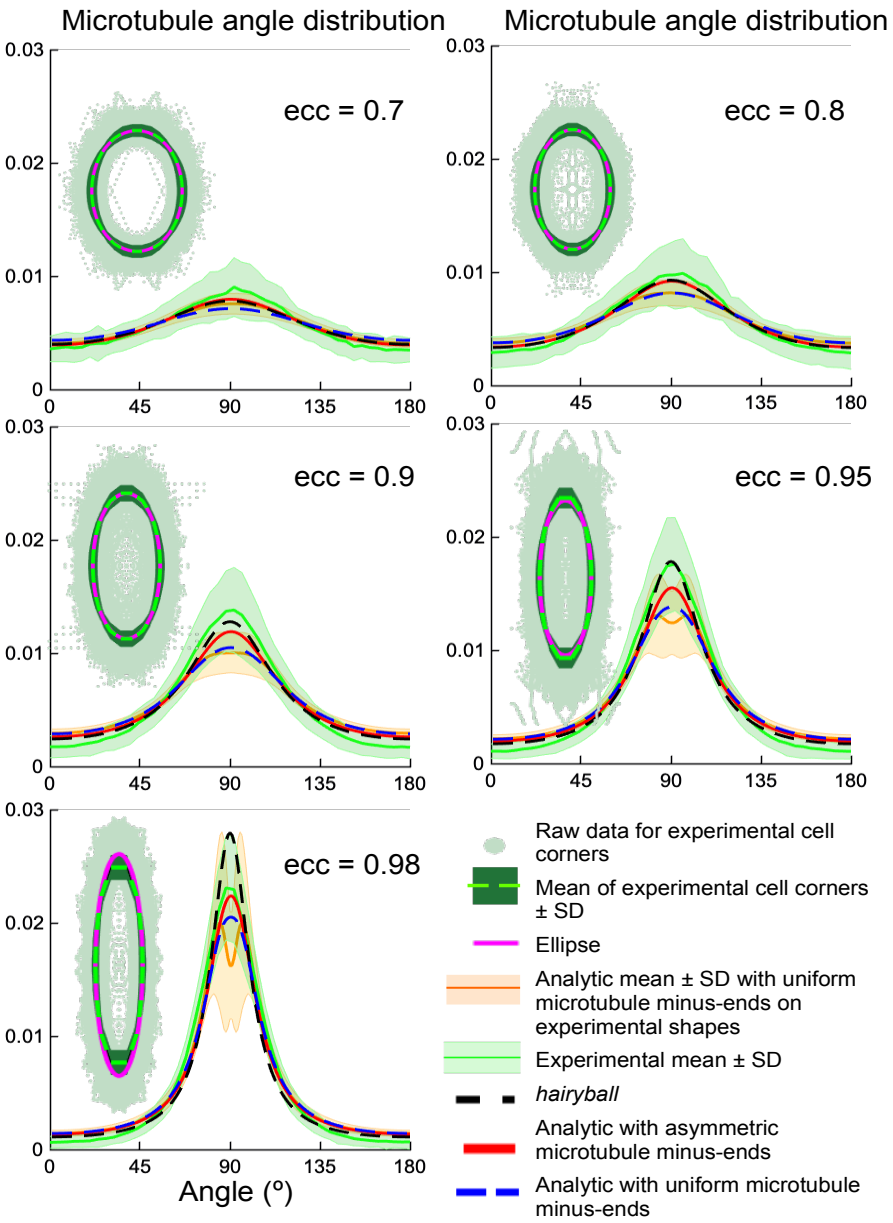

Figure 2.8: Top left of sub-figures: experimental cell shapes for different eccentricities. All the experimental cell boundary point data (*light green*), its standard deviation (*darker green cloud*) around the radial mean (*dark green line*). The analytical ellipse formula (*dashed magenta*) lays almost directly over the experimental mean curve. Bottom right of sub-figures: the corresponding microtubule angle distributions. The analytic model (2.17) with uniform seeding on all collected experimental cell shapes (*orange*). The standard deviation of the data is the light-orange envelope. The analytical model (2.17) with asymmetric seeding (*red*) predicts the experimental mean (*dark green*), and the *hairyball* (2.1) has good agreement up to eccentricity 0.95 with the experimental mean. The stochastic simulations (2.2) on a cell with uniform seeding are shown in (*dashed blue*). The standard deviation of the experimental data is the light-green envelope. The default parameters are given in Table 2.1.

2.5 Discussion

2.5.1 Summary

In this work we presented several novel findings describing the fundamental rules underlying self-organisation of microtubule networks in epithelial cells. Firstly, we have shown robustness of microtubule self-organisation both *in silico* and *in vivo*. Secondly, in addition to the known importance of cell shape to microtubule organisation [58], our minimal analytical model predicted the importance of the asymmetric seeding as the only other impactful parameter, which we then confirmed *in vivo* in *Drosophila* epidermal cells.

2.5.2 Robustness

Biologically, the discovered robustness of microtubule organisation makes perfect sense given the biological function of microtubules in a cell. Most of the intracellular trafficking events require microtubules for the delivery of various cellular components to their relevant biological locations by motor proteins [10, 66]. This process must be reliable, as mislocalization of cellular components leads to cell death or disease [11, 102, 97] despite the fact that the delivery mechanism is highly stochastic, given the nature of the microtubule dynamic instability and the dynamics of molecular motors [20, 60, 91]. We suggest that the overall organisation of the microtubule network is likely to guide the net outcomes of intracellular trafficking while minimizing the impacts of stochastic effects. Indeed, our mathematical model shows that while the dynamics is stochastic, the dependence of the microtubule self-organisation only on the slowly evolving parameters, such as the cell shape and the density of the minus-ends on the cell boundary, makes the average behaviour of the system deterministic on long time-scales. Averaging the cell shape over the cells of the same eccentricity brings us to the tissue level. Additionally, while most of the cells of given eccentricity in biological tissues are polygons, we found that their average cell shape is an ellipse. This suggests that though there might be differences in microtubule organisation in individual cells at a given point in time, on the tissue scale the average shape and hence microtubule organisation is robust.

One of the findings of our analytical model is that the robustness of microtubule self-organisation exists only as long as the microtubule dynamics exhibits a separation of time-scales, $\alpha', \beta' \ll \alpha, \beta$, a rule which is observed in all published data

about microtubule dynamic parameters [22, 131, 93, 92, 140, 138, 37, 162, 164]. Our mathematical model shows that if this rule is not observed, the microtubule organisation becomes sensitive to changes in these rates. As these rates depend on multiple internal and external factors, such as stochastic changes in gene expression and environment temperature, the microtubule organisation would be unpredictable at any certain time in a cell in a biological tissue. Therefore, breaking this rule will impair cellular function over time, which suggests that any mutations that led to such change were likely to cause cell lethality and did not fix in evolution.

2.5.3 *Hairyball* distribution

We have demonstrated that the microtubule angle distribution is accurately predicted by the *hairyball* distribution (2.1). The excellent agreement with the experimental data remains a mystery, as we were unable to show that *hairyball* (2.1) has any relation to the analytical distribution, neither as an approximation or a limiting case. We suggest that its best use is as a simple ad-hoc formula to parameterise the microtubule angle distribution in cells up to eccentricity 0.95.

2.5.4 The importance of microtubule-microtubule interactions

While we show that the microtubule self-organisation does not depend on the interaction of microtubules, we highlight that the measure of self-organisation we use is the time-averaged microtubule angle distribution. Such effects of microtubule-microtubule interactions as zipping and bundling disappear due to the time-averaging of the dynamics. From the biological point of view, what matters for the organism is the long-time behaviour, because most of the processes such as recycling occur at much longer time scales than microtubule network rearrangements [22, 81, 80]. Therefore, while bundling and zipping are aspects of the short-term behaviour, we hypothesize that it is the averaged microtubule angle distribution, which affects the tissue behaviour on the long time-scale with the long-term behaviour being more important than snapshots. However, we hypothesize, that these effects will affect short-term intracellular transport. For example, in [22] the presence of spastin, the microtubule severing protein, led to change in the delivery of the E-cadherin, the protein responsible for the cell-cell adhesion which is delivered along the microtubule network. A more detailed modelling approach that includes the effect of microtubule-microtubule interaction on the intracellular transport is outside the scope of this

article, and will be considered in future work.

2.5.5 Our system is a particular scenario, but we think it is general approach.

We suggest that our findings are applicable beyond apical microtubules in *Drosophila* embryonic epidermis, the dynamics of which is quasi-2D. Previously we have demonstrated that a similar relationship between microtubule organisation and cell shape is observed in other *Drosophila* epithelia, including cells in pupal wings and ovaries. These are only two of the examples where our findings are likely to hold true. There are multiple other instances, whereupon maturation and differentiation epithelial cells develop an apical microtubule meshwork, including cells of mammalian airways, and even cells in culture [54, 70, 147]. Furthermore, the same rules are likely to apply to squamous cells, where despite having a specialized apical microtubules, the cells depth is so small, that microtubules are constrained within a thin plane similar to that in our experimental model [59, 125]. The validation of our findings in other cell types and other evolutionary divergent organisms, as well as how the discovered robustness of microtubule self-organisation ensures reliability of intracellular transport are important questions for future research.

2.6 Materials and methods

2.6.1 Fly stocks

paired::Gal4, engrailed::Gal4, UAS::CD8-Cherry (Bloomington stock numbers1947, 32, and 27392, respectively), UAS::EB1-DN [22], UAS::Spastin [142], Patronin^{05252}, and Patronin-YFP [113]. The flies and embryos were kept at 18^oC.

2.6.2 Embryo fixation and antibody staining

The embryos were fixed as described in [58]. In brief, the staged embryos were dechorionated in 50% bleach for 4 min, and then fixed in 1:1 10% formaldehyde (methanol free, #18814, Polysciences Inc.) in PBS:heptane for $20min$ at room temperature (RT) and post-fixed/devitellinized for $45s$ in 1:1 ice-cold methanol:heptane. Finally, embryos were washed three times in ice-cold methanol, kept in methanol between 6 and $24h$ at 20^oC rehydrated in 1:1 PBS with 0.3% Triton X-100 (T9284,

Sigma): methanol and washed one time in PBS with 0.3% Triton X-100. Rehydrated embryos were blocked for $2h$ in 5% Native Goat Serum (ab7481, Abcam) in PBS with 0.3% Triton X-100. Primary antibody incubations were done overnight at 4^oC. Primary antibodies used were mouse anti-α-tubulin 1:1,000 (T6199, Sigma), and rat anti-E-cadherin 1:50 (DCAD2, Developmental Studies Hybridoma Bank). Incubation with secondary antibody was performed for $2h$ at 25^oC. Alexa Fluor fluorophore Alexa Fluor 488- and 647-coupled secondary antibodies (Jackson ImmunoResearch) were used in 1:300. Finally, embryos were mounted in Vectashield (Vector Laboratories).

2.6.3 Image acquisition

All images from fixed samples were acquired at RT ($20{,}22^oC$). For quantification of microtubule self-organisation, 16-bit depth images were acquired on the Zeiss AiryScan microscope, using 60x objective lens. A z-stack of 8 sections with $23.5px\mu m$ in XY resolution and $0.38\mu m$ distance between sections were taken. All processing was done at 6.5 power in the X software. For an analysis of Patronin-YFP distribution, an upright confocal microscope (FV1000; Olympus) using 60×1.42 NA oil PlanApoN objective lens was used. 16-bit depth images were taken at a magnification of 12.8pixel/μm with $0.38\mu m$ between z-sections. Image acquisition was done with FV10-ASW software for the upright confocal microscope (FV1000; Olympus).

The sub-apical domain of the cell was determined using the E-cadherin junctional signal as a reference for its basal limit, and the absence of α-tubulin signal as a reference for its apical limit. All imaging was done on dorso-lateral epidermal cells, with excluded the leading edge (first row) cells, given its different identity to the rest of the dorso-lateral epidermal cells.

Images were averaged for measuring signal area and Patronin-YFP distribution using Fiji (`www.fiji.sc`). Figures were assembled using Adobe CS3 Photoshop and Illustrator (`www.adobe.com`). Processing of images shown in figures involved adjusting of gamma settings.

2.6.4 Image analysis to quantify microtubule organisation

The same workflow as described in the [58] was used. In short, E-cadherin signal from a max intensity projection was used to obtain cell outlines using Packing Analyser V 2.0 software [2]. These cell outlines were used to identify each cell as an individual

object and fit it to an ellipse to calculate eccentricity and the direction of the ellipse major axis using a script in MATLAB R2017b (Mathworks, `www.mathworks.co.uk`). The α-tubulin signal within each cell was filtered using the cell outline as a mask, and the magnitude of the signal according to its direction analysed by convolving the filtered α-tubulin signal with two 5×5 Sobel operators [58]. The resulting magnitude gradient and direction gradient were integrated into a matrix to assign each pixel a direction and magnitude of change in the intensity of α-tubulin signal. To reduce the noise, the pixels with the magnitude less than 22% of the maximum change were discarded. The remaining pixels were binned with respect to their direction gradient (bin size= 4 degrees). The resulting histogram was normalized. The script is available at `https://github.com/nbul/Cytoskeleton`.

To calculate the area of α-tubulin signal within each cell, a custom-made MATLAB script was used. The average projected images were adjusted such that 0.5% of the data with lowest intensities were set to black and the 0.5% of the data with highest intensities were set to white in order to compare datasets across genotypes and compensate for potential variability of antibody staining and laser power. The threshold was then calculated using Otsu's method, and a binary image was created using the calculated threshold multiplied by 0.7. This multiplication parameter was determined empirically by testing images from different experiments. Finally, the per cent of pixels above threshold was calculated for each cell. The script is available at `https://github.com/nbul/Cytoskeleton`.

2.6.5 Image analysis to quantify Patronin-YFP distribution

The average projection of each z-stack was done using Fiji software, and segmented using Packing Analyzer v2.0. The resulting binary images with coordinates of cell-cell borders and vertices were used together with unprocessed average projection by a custom-made MATLAB scripts to extract the following values: apical cell area, cell elongation (ratio between long and short axes of the best fit ellipse), average cell orientation within the image (only in embryos), orientation of individual cell-cell borders relative to average cell orientation (embryos), and mean intensity of each individual border. Only the cells that were completely within the image were taken for quantification. Bristle cells were excluded by their size. Only the borders that are between two cells that were completely within the image were quantified, and the borders adjacent to bristle cells were excluded. The background signal was

determined by binarizing images with an adaptive threshold, which uses local first-order image statistics around each pixel, which is very efficient in detecting puncta. The mean background signal of cells that were completely within the image was subtracted from mean intensities of cell-cell borders as background. The values for each type of border within single embryos were averaged, and the average intensity of borders with $40 - 90^o$ orientation was divided by the average intensity of borders with $0 - 10^o$ orientation to produce a single value of distribution asymmetry for each embryo. Finally, to produce distribution of signal intensity by angle, borders of all embryos at stage 15 of development were pulled and binned using 10^o bins. The script is available at `https://github.com/nbul/Intensity`.

2.6.6 Statistical analysis

All data was analysed using Graphpad Prism 6.0c (`www.graphpad.com`). Samples from independent experiments corresponding to each genotype were pooled and tested for normality with the Shapiro-Wilk test. The effects of manipulation on α-tubulin signal area were analysed using ANOVA with post-hoc t-test.

Chapter 3

Self-organisation of microtubules in cells with dense cytoplasm

This chapter is being developed for a publication in collaboration with Lyuba Chumakova and Natalia Bulgakova. Natalia Bulgakova contributed to the section by performing experiments on the *Drosophila* follicular epithelium.

3.1 Introduction

In order for organelles to be delivered to their corresponding biologically relevant locations, they are transported via motor proteins along the microtubule cytoskeleton. Thus the directionality of the microtubule cytoskeleton is essential for maintenance of correct cell function. The microtubule cytoskeleton consists of highly dynamic polarised filaments. Their "plus ends" undergo dynamic instability, in particular, microtubules are in either growing or shrinking states and switch between these two states infrequently. The microtubules polymerise into a cylinder, adding dimers through the binding of two tubulin guanine tri-phosphates (T.GTPs) to their plus ends. In the process of catastrophe the microtubule cap (GTP) changes to a tubulin guanine di-phospate (T.GDP). The resulting unstable microtubule analogue continues to depolymerise until all tubulin is lost or GTP is recovered in the process of rescue.

To establish the large-scale direction of transport inside cells microtubules self-organise. This is often driven by cell-scale features, e.g. geometry [58]. The self-organisation measure that we use is the length-weighted microtubule angle distribu-

tion. To extract this distribution from cell images (Figure 3.1), we use singular value decomposition (SVD) to define the cell eccentricity $ecc = \sqrt{1 - \frac{a^2}{b^2}}$, where a is the minor and b is the major axes of the cell. We then rotate the cell so that the major axis of the cell lies at 90^o to the horizontal. The microtubule angle distribution $\rho(\varphi)$ is defined as a length-weighted distribution of microtubule angles φ with respect to the horizontal; note that $\varphi \in [0\,, \pi)$ as we do not distinguish the directionality of microtubules. Finally, the microtubule angles for every image pixel are computed (see materials and methods in [58]). We have previously shown that in *Drosophila* epithelium cells microtubule cytoskeleton self-organisation is driven by cell geometry alone [58] and is robust at the tissue scale (see Chapter 2).

However, in general, cells are densely packed with organelle and macromolecules which makes their interior either isotropic or anisotropic. Such barriers include macromolecules and mitochondria [43, 163, 104, 155]. Inside the densely packed cells the polymerisation of microtubules may not be able to occur freely, since organelles such as mitochondria or vacuoles that crowd the cytoplasm could act as potential barriers to growing microtubules. The significance of cytoplasmic crowding can be seen through the example of protein folding, where varying concentrations of macromolecular crowding were shown to lead to a speed up of transition-limited reactions but a slowing down of diffusion-limited reactions [163], [38]. To our knowledge, there are no existing models of microtubule cytoskeleton self-organisation in cells with cytoplasmic crowding, and the only model that involves microtubules and macromolecular crowding discusses that kinesin-8 creates traffic jams [96] whereas the effects on microtubules themselves remain unknown.

Our collaborator measures the microtubule self-organisation in our model system – epithelial cells in the *Drosophila* embryo between stages 12-15 of development. These cortical microtubules are located in the subapical ("top") layer, which is 1 μm, deep along the adhesion band of the cell, making the problem quasi-2D (as introduced in Chapter 2 Figure 1.4). Unlike the typical studied problems where the microtubules are seeded in one location (e.g. the centrosome), in our system the microtubule minus ends are seeded on the cell boundary along the adhesion band. The epithelial tissue in *Drosophila* exhibit different scenarios of cell crowding. In the embryonic epidermis and the pupal wing there are no distinct anisotropic barriers, while in the follicular epithelium actin cables are present throughout the subapical cell section where the microtubule dynamics occur (see Figure 3.1). Note that actin cables are not unique to the follicular epithelium, as they also exist in budding yeast and intestinal

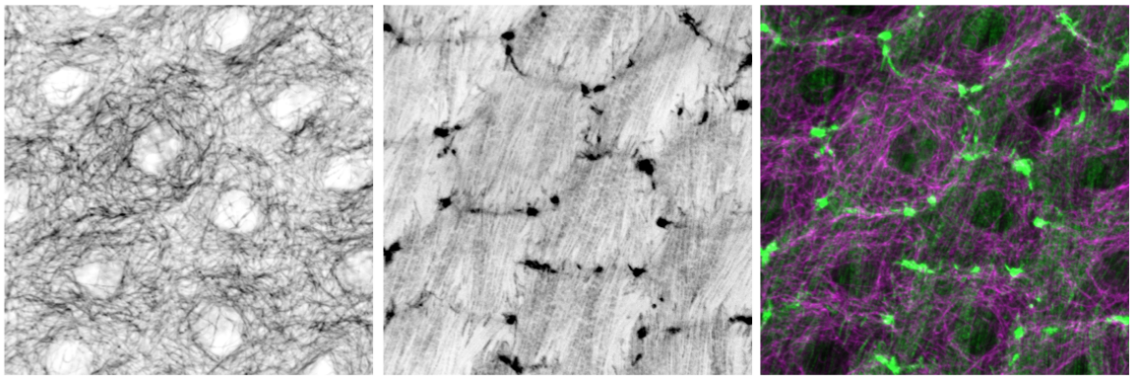

Figure 3.1: The above experimental image show tissue from *Drosophila* follicular epithelium during stage 12. The panels from left to right show i) the microtubules, ii) the actin cables and iii) microtubules (magenta) and actin cables (green). The image is provided courtesy of Dr. Natalia Bulgakova.

epithelial cells [161]. The anisotropy introduced by subapical actin cables can lead to different microtubule organisations through microtubule-actin interactions. In particular, actin cables can change the direction of a growing microtubule through cross-linking proteins, whereas cortical actin can act as a barrier for microtubule growth or provide microtubules with anchoring sites through microtubule stabilizing complexes [40]. Here we build a model that includes microtubule interactions with subapical actin and discuss how our works relates to the experimental results.

Another focus of this work is the degree of the microtubule bundling, which occurs where two or more microtubules zip along each other, polymerising in the same direction due to the presence of cross-linking proteins. Bundling occurs in many experimental systems [67]. We hypothesise that it is essential to cell function, as bundled microtubules make the intracellular transport directions persistent. Microtubules in a bundle influence the direction of any microtubules that come into contact with them and once the original bundle microtubule collapses, the newly established bundle continues to polymerise in the bundle direction. Here we show how bundling depends on the parameterisation of the microtubule dynamic instability, microtubule interaction and cytoplasmic barriers.

In this Chapter we investigate the fundamental question of how microtubule self-organisation is affected by the anisotropy of the crowded cytoplasm as follows. We start by introducing the model for individual microtubules and their interactions with various barriers in Section 3.2. Next, we study microtubule self-organisation using stochastic models and probabilistic descriptions in Section 3.3. We explore

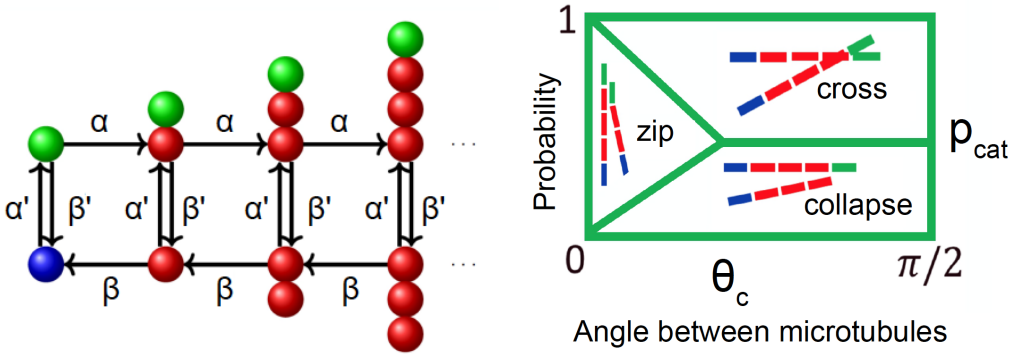

Figure 3.2: The schematic for the mathematical model of microtubule self-organisation: the left hand side illustrates a model of dynamic instability via a Markov chain, while the right hand side illustrates the parametrisation of the collision dynamics.

bundling in Section 3.4 and conclude with a discussion in Section 3.5. Finally, we use our model to hypothesise which type of interactions occur between microtubules and actin cables in various stages of development in *Drosophila* follicular epithelium.

3.2 Modelling a single microtubule

In this model we represent microtubules as 1D and each model dimer represents 13 real dimers which make up one subunit of the microtubule cylinder. To model the dynamic instability of microtubules we use a Markov chain (2.2) (Figure 3.2) where microtubules begin in a seeded state. The seed (blue sphere) can gain a polymerising T.GTP cap (green sphere) which subsequently continues to polymerise at a rate α or undergoes catastrophe at a rate β'. In the depolymerising state (red spheres) the microtubule shrinks at the rate β or undergoes rescue at a rate α' . Although epithelial cells are 3D, our system is quasi-2D because cortical microtubule dynamics are in the subapical $1\mu m$ thin layer of the cell, where the microtubules are seeded along the adhesion belt, which in the model we refer to as the cell boundary. It remains an open question in cell biology as to why the subapical microtubules remain in this plane.

In our model the collision between two microtubules is angle-dependent. We measure where the angle between two growing microtubule θ_{MT} falls with respect to the critical angle θ_c (see Figure 3.2). If $\theta_{\mathrm{MT}} > \theta_c$, the approaching microtubule

undergoes catastrophe with probability p_{cat} or crosses otherwise. If $\theta_{\mathrm{MT}} < \theta_c$, the approaching microtubule collapses with probability $\frac{\theta_{\mathrm{MT}}}{\theta_c} p_{cat}$, crosses with probability $\frac{\theta_{\mathrm{MT}}}{\theta_c}(1 - p_{cat})$ and zips (changes its direction to grow alongside the microtubule it encounters) otherwise. In summary, these are the outcomes for microtubule interactions

$$p_{catastrophe} = \begin{cases} p_{cat} & if \quad \theta_{MT} > \theta_c; \\ 1 - p_{cat} & if \quad \theta_{MT} \leq \theta_c. \end{cases} \tag{3.1}$$

$$p_{cross} = \begin{cases} 1 - p_{cat} & if \quad \theta_{MT} > \theta_c; \\ \frac{\theta_{MT}}{\theta_c}(1 - p_{cat}) & if \quad \theta_{MT} \leq \theta_c. \end{cases} \tag{3.2}$$

$$p_{zip} = \begin{cases} 1 - \frac{\theta_{MT}}{\theta_c} p_{cat} & if \quad \theta_{MT} \leq \theta_c. \end{cases} \tag{3.3}$$

where $p_{catastrophe}$ or p_{cat} is the probability of collapse, p_{cross} is the probability of crossing, p_{zip} is the probability of zipping, θ_{MT} is the angle between two colliding microtubules and θ_c is the critical collision angle. Parameters p_{cat} and θ_c are set by us in the simulations as outlined in Section 3.2.2.

3.2.1 Modelling cytoplasmic barriers

We study cell crowding for two different scenarios: *isotropic* and *anisotropic* cytoplasm. We define an isotropic cytoplasm as one where barriers have statistical properties that do not vary based on a given direction inside the cell (as described by Taylor in the context of isotropic turbulence [149]). In the anisotropic cytoplasm, the barriers are aligned with the angle θ_b with respect to the horizontal. The anisotropy describes the barrier strength being affected by the microtubule angle. We further define *homogeneous* barriers as ones where the strength of the barrier does not change for a microtubule growing in a given direction. *Discrete* barriers introduce two catastrophe parameters: when a microtubule does not encounter a barrier, it has a base value for the probability of catastrophe; when it encounters a barrier, this base probability for catastrophe is increased.

The self-assembly of microtubules follows a Markov Chain as seen in (2.2). If the microtubule is in initial state (blue sphere) it can start self-assembly as it moves to

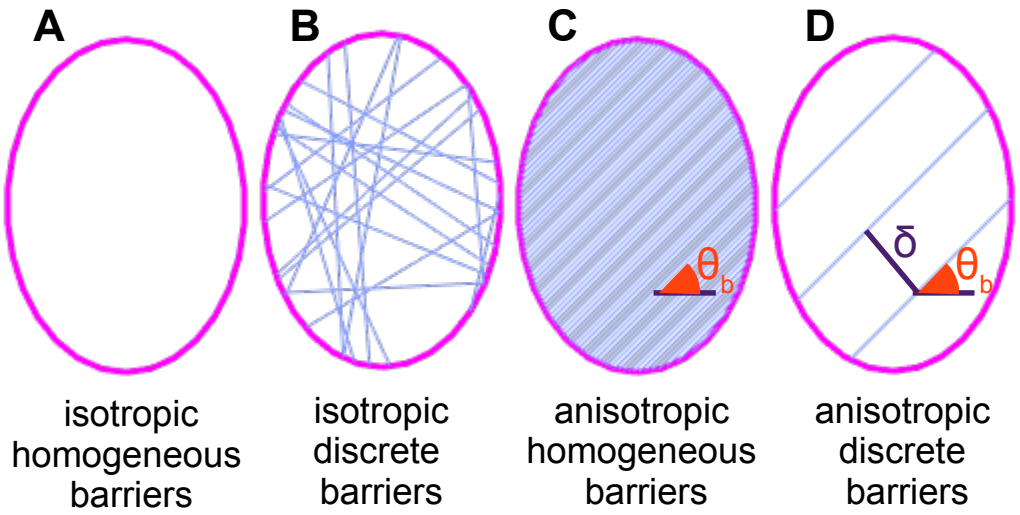

Figure 3.3: A schematic showing the four models for cytoplasmic crowding inside the cell: A) isotropic homogeneous barriers, B) isotropic discrete barriers (e.g. actin mesh), C) anisotropic homogeneous barriers placed at an angle θ_b with respect to the horizontal and D) anisotropic discrete barriers placed at an angle θ_b with respect to the horizontal with spacing δ between each other (e.g. actin cables).

a growing state of chain length one with probability 1. Further, if it is in the polymerising state, denoted by $X_{n,1}$ where $n \in \mathbb{Z}_{>0}$ signifies the number of dimers inside the inner chain, it can either grow by one tubulin dimer in its chain with probability $\alpha/(\alpha+\beta')$ or it can change to the corresponding shrinking state with probability $\beta'/(\alpha+\beta')$. Finally, if the microtubule is in the dissociating state, denoted by $X_{n,0}$ where $n \in \mathbb{Z}_{>0}$ is the number of dimers, then it can either shrink by one tubulin length with probability $\beta/(\alpha'+\beta)$ or change to a growing state with probability $\alpha'/(\alpha'+\beta)$. However whenever the microtubule encounters a barrier it has a higher probability of collapse p_b. For example when barriers cross a growing microtubule

every second dimer we can construct the following transition matrix for the system

$$
\begin{array}{c}
 \\
X_{0,0} \\
X_{0,1} \\
X_{1,0} \\
X_{1,1} \\
X_{2,0} \\
X_{2,1} \\
X_{3,0} \\
X_{3,1} \\
\dots
\end{array}
\begin{array}{c}
\begin{array}{cccccccc} X_{0,0} & X_{0,1} & X_{1,0} & X_{1,1} & X_{2,0} & X_{2,1} & X_{3,0} & X_{3,1} \end{array} \\
\left(\begin{array}{cccccccc}
0 & 1 & 0 & 0 & 0 & 0 & 0 & 0 \\
\frac{\beta'}{\alpha+\beta'} & 0 & 0 & \frac{\alpha}{\alpha+\beta'} & 0 & 0 & 0 & 0 \\
\frac{\beta}{\alpha'+\beta} & 0 & 0 & \frac{\alpha'}{\alpha'+\beta} & 0 & 0 & 0 & 0 \\
0 & 0 & p_b & 0 & 0 & \frac{\alpha}{\alpha+\beta'} & 0 & 0 \\
0 & 0 & \frac{\beta}{\alpha'+\beta} & 0 & 0 & \frac{\alpha'}{\alpha'+\beta} & 0 & 0 \\
0 & 0 & 0 & 0 & \frac{\beta'}{\alpha+\beta'} & 0 & 0 & \frac{\alpha}{\alpha+\beta'} \\
0 & 0 & 0 & 0 & \frac{\beta}{\alpha'+\beta} & 0 & 0 & \frac{\alpha'}{\alpha'+\beta} \\
0 & 0 & 0 & 0 & 0 & 0 & p_b & 0 \\
\dots & \dots & \dots & \dots & \dots & \dots & \dots & \dots
\end{array}\right)
\end{array}
\begin{array}{c}
\\ \\ \\ \\ \\ \\ \\ \\ \\

oriented at, θ_b, with respect to the horizontal. In this case, the microtubule dynamics depend on how aligned the microtubule is with respect to the angle of the anisotropy. Microtubules parallel to θ_b undergo catastrophe at an unchanged rate β', whereas for microtubules perpendicular to θ_b the catastrophe rate is increased to $\left(\frac{\alpha p_b}{1-p_b}\right)$ where p_b denotes the probability of collapse at a barrier and α and β' are the default rates of growth and catastrophe respectively (see Figure 3.3 C).

- **Anisotropic discrete barriers:** This final case is inspired by the case of discrete actin cables oriented at an angle θ_b with respect to the horizontal and separated by a distance δ (see Figure 3.3 D). In this case the microtubule collapses if it encounters a barrier with probability p_b.

We model the barriers as stationary, since actin cables undergo self-assembly at a much slower rate than microtubules and hence can be considered to remain stationary on the time-scales of microtubule self-organisation (see Section 3.2.2 for further discussion). This is however, a first order model and future work could potentially be extended to involve dynamic barriers. The numerical simulations are performed in Matlab [108].

3.2.2 Parameter ranges studied

In the previous work we have shown that the cell geometry and the distribution of microtubule minus ends determine the microtubule cytoskeleton self-organisation (see Chapter 2). Here we present the results of stochastic simulations on an elliptical cell, which is the average of experimental cell shapes (see Section 2.4.1). We use two cell eccentricities: $\{ecc = 0.7\,, 0.98\}$ which cover the experimental range of eccentricities which are obtained for stages 12-15 of *Drosophila* development, as discussed in Chapter 2.

The microtubule dynamics parameters $\alpha\,, \beta\,, \alpha'\,, \beta'$ were chosen to roughly correspond to experimental parameter ranges (see Section 2.2.2 for a full discussion on parameter estimation and Figure 3.1). The base value of p_{cat} was chosen to be 0.01, since in our experiment the microtubules rarely underwent catastrophe. In the barrier cases it is varied as described below. We set $\theta_c = 30^o$ as it gives simulations for microtubule dynamics that closely resemble experimental images; we note that due to the limitations of super-resolution microscopy, experimental values of θ_c are not

Parameter	Default parameter	Dimensional equivalent
α	1000	$0.15\mu m/s$
β	3500	$0.52\mu m/s$
α'	4	$0.07316s^{-1}$
β'	1	$0.01829s^{-1}$
p_{cat}	0.01	–
θ_c	30^o	–

Table 3.1: Summary of key parameters describing microtubule dynamics in our models.

known. Setting $\theta_c = 30^o$ also takes into account microtubule rigidity, since they are able to bend but by too much. The default parameters used are summarised in Table 3.1. The microtubule minus-ends have not been imaged inside the *Drosophila* follicular epithelium, and we use 200 seeds inside our stochastic simulations, distributed uniformly across the cell boundary.

We study the following ranges of parameter values across the four models:

- **Isotropic homogeneous barriers:** $p_{cat} \in \{0.1, 0.2, 0.3\}$ and $\theta_c \in \{10^o, 20^o, 30^o, 40^o\}$;
- **Isotropic discrete barriers:** strength of barriers $p_b \in \{0.1, 0.2, 0.3\}$ and number of barriers $N_b \in \{50, 100, 150\}$;
- **Anisotropic homogeneous barriers:** strength of barriers $p_b \in \{0.1, 0.2, 0.3\}$ and angle of barriers $\theta_b \in \{0^o, 45^o, 90^o\}$;
- **Anisotropic discrete barriers:** strength of barriers $p_b \in \{0.1, 0.2, 0.3\}$, angle of barriers $\theta_b \in \{0^o, 30^o, 60^o, 90^o\}$ and spacing between barriers $\delta \in \{5, 10, 20\}$.

The statistics of stochastic simulations were collected as follows. Simulations were run on the server up to a non-dimensional time 10 (in dimensional terms this is equivalent to 550s). For each parameter combination we run 500 simulations. The time-averaging of the microtubule angle distribution was performed over the last 7.5 non-dimensional time units, therefore taking account of microtubule dynamics once the network has stabilised (for more information on the convergence of the measure of microtubule self-organisation see [58].)

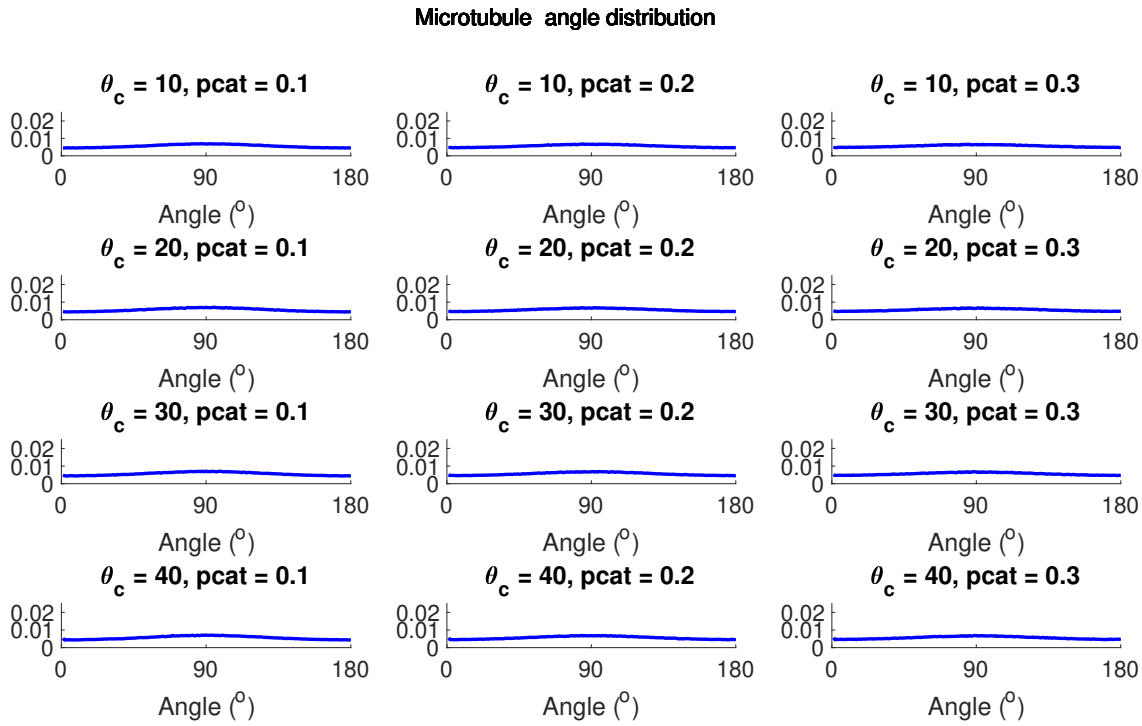

Figure 3.4: The microtubule angle distributions (blue lines) for the case of isotropic homogeneous barriers computed via numerical simulations (2.2) with varying microtubule interaction parameters and $ecc = 0.70$. The corresponding control microtubule angle distribution (dashed black lines) of the isotropic homogeneous barriers with default parameters. Other parameters remain at their default value (see Table 3.1).

3.3 Models of cytoplasmic crowding

We model microtubule self-organisation in the four models of dense cytoplasm by considering: homogeneous isotropic, discrete isotropic, homogeneous anisotropic and discrete anisotropic barriers (see Figure 3.3). We explore homogeneous isotropic, homogeneous anisotropic and discrete anisotropic cases[1] analytically. As the discrete isotropic case is not analytically tractable, we explore it via stochastic simulations.

[1]For discrete anisotropic barriers we can only obtain a solution and agreement between the analytical solution and stochastic simulation's in a particular range of barrier strengths and spacings.

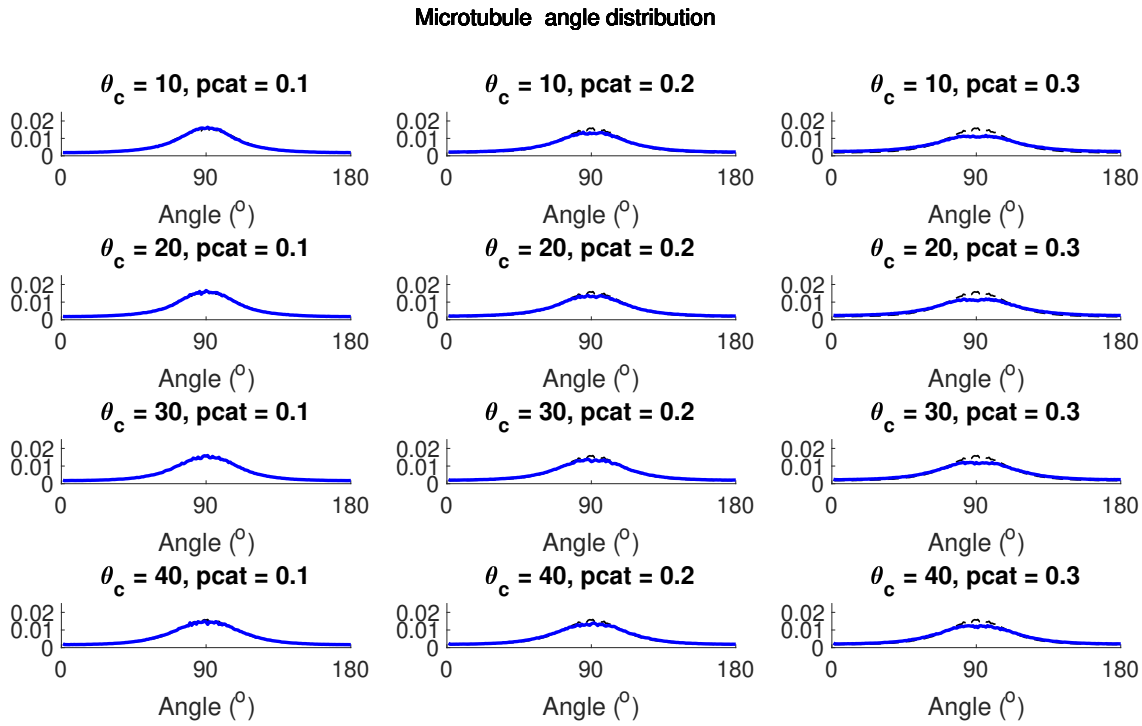

Figure 3.5: The microtubule angle distributions (blue lines) for the case of isotropic homogeneous barriers computed via numerical simulations (2.2) with varying microtubule interaction parameters and $ecc = 0.98$. The corresponding control microtubule angle distribution (dashed black lines) of the isotropic homogeneous barriers with default parameters. Other parameters remain at their default value (see Table 3.1).

3.3.1 Isotropic homogeneous barriers

Our first study considers isotropic homogeneous barriers by varying the probability of catastrophe β' in the Markov chain that represents microtubule dynamics. The microtubules can encounter barriers uniformly across the cell and therefore have a higher probability of losing a T.GTP cap.

Figures 3.4 and 3.5 show the microtubule angle distributions obtained from stochastic simulations for varying $\theta_c = [10\,, 20\,, 30\,, 40]$ and $p_{cat} = [0.1\,, 0.2\,, 0.3]$. We see that these parameters do not significantly affect the microtubule angle distribution which depends only on cell eccentricity.

This result can be explained using the analytic derivation of the microtubule angle distribution, see Chapter 2 Section 2.2.3. We summarise the derivation using

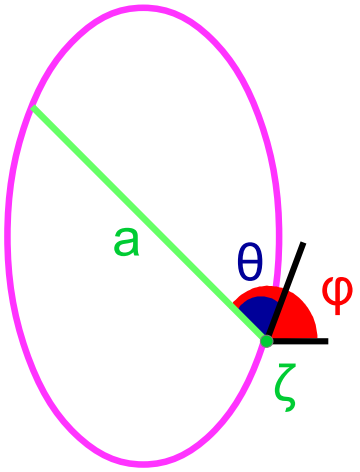

Figure 3.6: Schematic of a cortical microtubule in an epithelial cell. The cell boundary is parameterised by the coordinate ζ. A microtubule is seeded at the point ζ and grows at an angle φ with respect to the horizontal and angle θ with respect to the cell boundary. The microtubule can grow length a until it reaches the cell boundary.

Figure 3.6. We calculate the length-weighted mean survival time of a single microtubule placed at position ζ at the cell boundary that can grow into a direction $\theta \in [0, \pi)$ uniformly. We use the assumptions that it undergoes dynamic instability and collapses upon hitting the boundary when its length reaches a. We note the cell cross-section as $a(\zeta, \theta)$ and $\tilde{a}(\zeta, \phi)$ depending on if we describe the angle of the microtubule growth with respect to the cell boundary or the horizontall. We then consider the distribution of microtubule angles with respect to the horizontal by integrating over the length-weighted mean survival time of all microtubules seeded at the boundary. The microtubule angle distribution (see Chapter 2 Section 2.2.3 for full details) is

$$\rho(\phi) = \frac{1}{M} \int \frac{1 - e^{-\tilde{a}(\zeta,\phi)p}(1 + \tilde{a}(\zeta,\phi)p)}{1 + \frac{q\alpha'}{\pi} \int_0^\pi \frac{1 - e^{-a(\zeta,\theta)p}}{p} d\theta} \rho(\zeta) d\zeta \,, \tag{3.5}$$

where $p = \frac{\beta'}{\alpha} - \frac{\alpha'}{\beta}$, $q = \frac{1}{\alpha} + \frac{1}{\beta}$, $\rho(\zeta)$ is the microtubule seed distribution, $\tilde{a}(\zeta, \phi)$ (or $a(\zeta, \theta)$) is the length of a microtubule growing from seed ζ at an angle ϕ(or θ) with respect to the cell boundary (or the horizontal), and M is the normalising constant.

In our simulations, microtubules are seeded uniformly so the microtubule minus

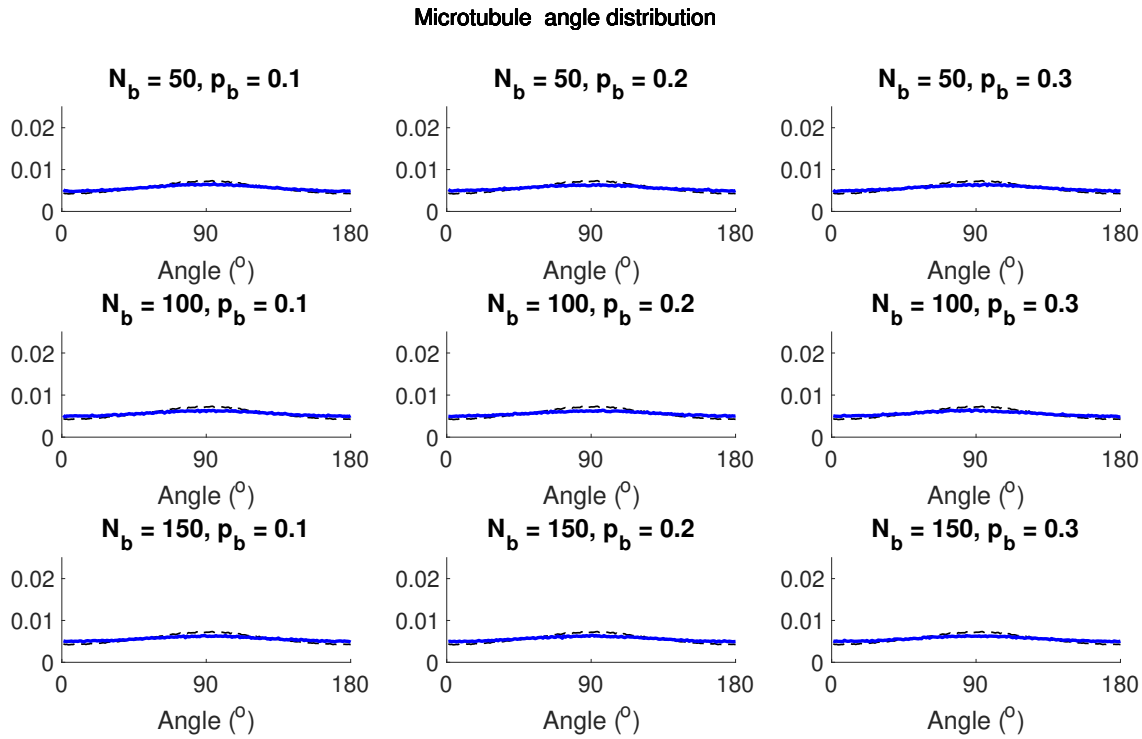

Figure 3.7: The microtubule angle distributions (3.4) (blue lines) for the case of isotropic discrete barriers with $ecc = 0.7$. The corresponding control microtubule angle distribution (dashed black lines) of the isotropic homogeneous barriers with default parameters. Other parameters remain at their default value (see Table 3.1).

end distribution considered in this Chapter is $\rho(\zeta) = 1$. Hence,

$$\rho(\phi) = \frac{1}{M} \int \frac{1 - e^{-\tilde{a}(\zeta,\phi)p}(1 + \tilde{a}(\zeta,\phi)p)}{1 + \frac{q\alpha'}{\pi} \int_0^\pi \frac{1-e^{-a(\zeta,\theta)p}}{p} d\theta} d\zeta \,. \tag{3.6}$$

We recall from Chapter 2 that the microtubule self-organisation is robust with respect to changes in β'. Therefore, we expect that the distribution is robust to changes in $p_{cat} = \frac{\beta'}{\beta'+\alpha}$ as well, which is demonstrated in the stochastic simulations reported in Figure 3.4. The barriers in this formula are included through changes in the parameter p which is constant. Increasing p increases the probability of catastrophe in any given direction in the cell.

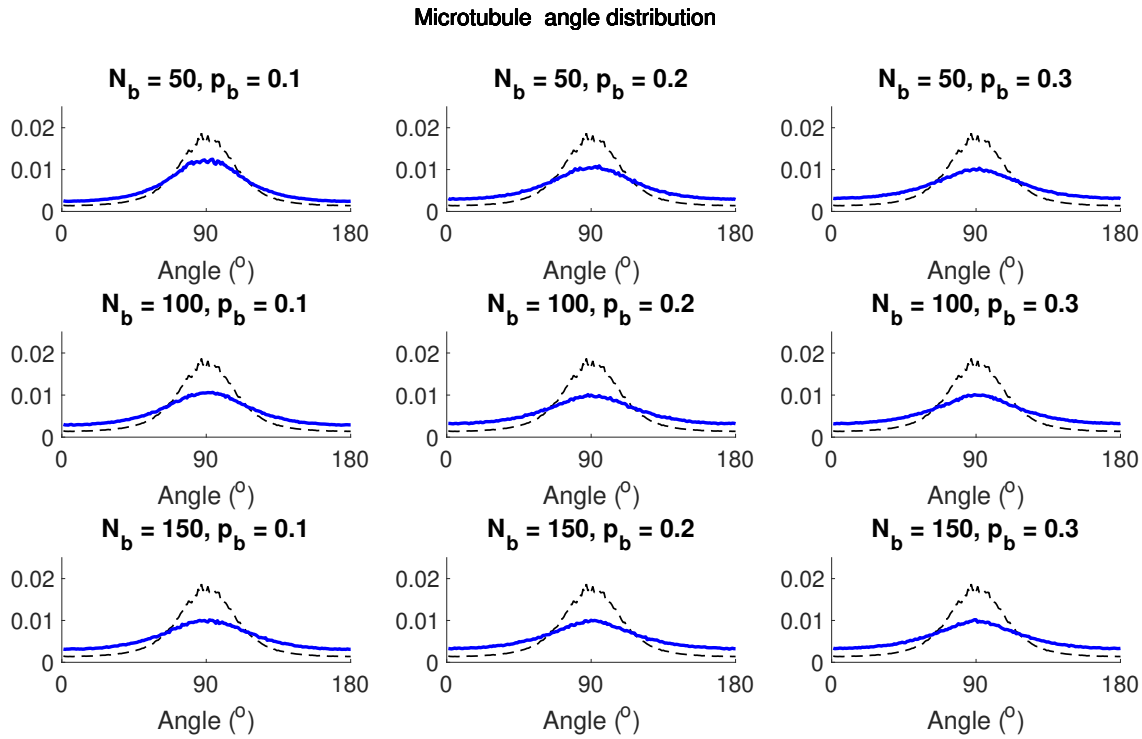

Figure 3.8: The microtubule angle distributions (3.4) (blue lines) for the case of isotropic discrete barriers with $ecc = 0.98$. The corresponding control microtubule angle distribution (dashed black lines) of the isotropic homogeneous barriers with default parameters. Other parameters remain at their default value (see Table 3.1).

3.3.2 Isotropic discrete barriers

We continue the study of isotropic barriers by considering randomly oriented discrete barriers, similar to an actin mesh, using stochastic simulations. We vary the number of barriers, N_b, and the probability of collapse at the barriers, p_b, for two different cell eccentricities.

We find that increasing the effective barrier strength (either by increasing the number of barriers or by increasing the corresponding p_b) does not alter the distributions. Note that the level of noise increases, since microtubule lifetimes are generally shorter due to frequent collisions (see Figures 3.7,3.8). Overall, for either case of isotropic barriers there is no influence on the mean of the microtubule angle distribution.

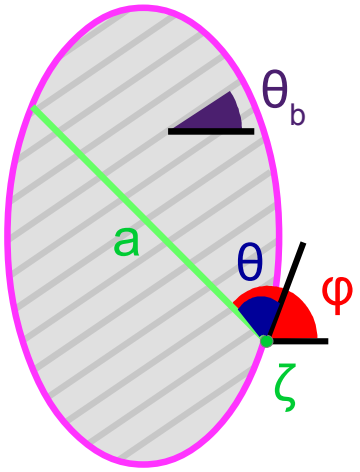

Figure 3.9: Schematic of a cortical microtubule in an epithelial cell. The cell boundary is parameterised by the coordinate ζ. A microtubule is seeded at the point ζ and grows at an angle φ with respect to the horizontal and angle θ with respect to the cell boundary. The angle θ_b denotes the angle of the dense barriers with respect to the horizontal. The microtubule can grow length a until it reaches the cell boundary.

3.3.3 Anisotropic homogeneous barriers

The next model we consider is an idealisation of anisotropy, where barriers are densely packed and oriented at an angle θ_b (see Figure 3.9). We study the microtubule angle distribution by modifying our model in Section 3.3.1 and the resulting formula (3.6).

For the anisotropy angle, θ_b, let the catastrophe rate be β' in the direction of the anisotropy and $\left(\frac{\alpha p_b}{1-p_b}\right)$ in the direction perpendicular to θ_b, where p_b is the barrier strength and α is the growth rate.

We can now describe the microtubule angle distribution using

$$\rho(\phi) = \frac{1}{M}\int \frac{p(\zeta,\psi)^{-2}(1-e^{-\tilde{a}(\zeta,\phi)p(\zeta,\psi)}(1+\tilde{a}(\zeta,\phi)p(\zeta,\psi)))}{1+\frac{q\alpha'}{\pi}\int_0^\pi \frac{1-e^{-a(\zeta,\theta)p(\zeta,\psi)}}{p(\zeta,\psi)}d\theta}d\zeta\,, \tag{3.7}$$

where $p(\zeta,\psi) = \frac{\tilde{\beta}'(\zeta,\psi)}{\alpha} - \frac{\alpha'}{\beta}$, $q = \frac{1}{\alpha} + \frac{1}{\beta}$, $\tilde{a}(\zeta,\phi)$ (or $a(\zeta,\theta)$) is the length of a microtubule growing from seed ζ at an angle ϕ (or θ) with respect to the horizontal (or the cell boundary), and M is the normalising constant.

Note that to model a varying catastrophe rate with the angle of anisotropy homogeneously we now have the dependence $p(\zeta,\psi)$. In the original model we had that

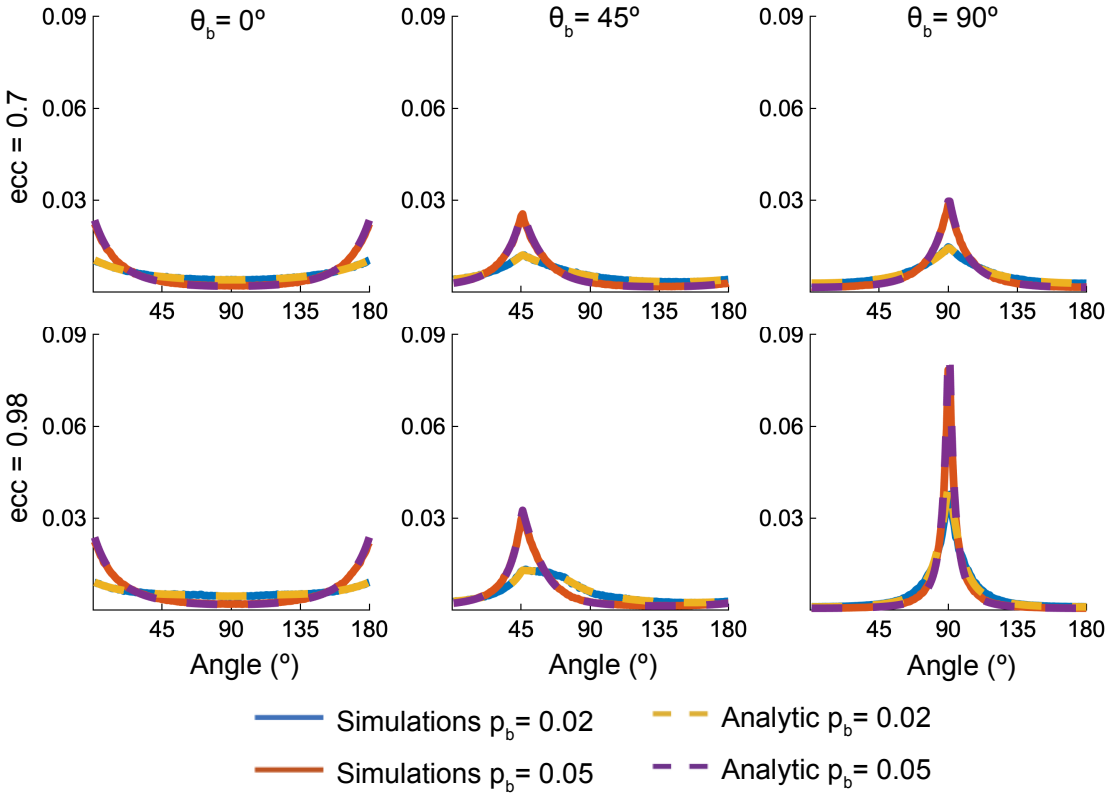

Figure 3.10: The microtubule angle distributions for the case of anisotropic homogeneous barriers (obtained from (3.7)) and using stochastic simulations. Parameters not specified in the figure remain at their default value (see Table 3.1).

p was constant, whereas now we consider barriers inside the cell which change the probability of catastrophe based on angle of the growing microtubule. We propose to parameterise the dependence of the catastrophe rate $\tilde{\beta}'$ on the angle between the microtubule and the anisotropy as follows:

$$\tilde{\beta}'(\zeta, \psi) = |\cos(\psi)|\beta' + |\sin(\psi)| \left(\frac{\alpha p_b}{1 - p_b} \right) , \tag{3.8}$$

where $\psi = \varphi - \theta_b$, see Figure 3.11. This choice describes that the catastrophe rate switches between two values based on the microtubule orientation with respect to the anisotropy of the cell. Since we don't know the strength of anisotropic barriers in cells, we choose to vary the catastrophe rate so that up to 30% of microtubules will collapse upon hitting barriers as defined in our parameter choices.

The stochastic simulations and the analytic formula (3.7) for anisotropic homogeneous barriers agree as seen in Figure 3.10.

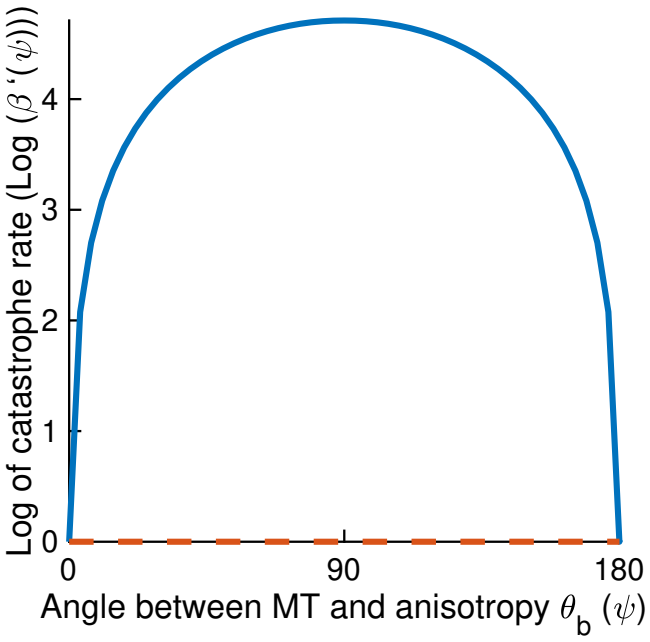

Figure 3.11: The blue line shows $Log(\tilde{\beta}'(\psi)) = Log\left(|\cos(\psi)|\beta' + |\sin(\psi)|\left(\frac{\alpha p_b}{1-p_b}\right)\right)$, with $\beta' = 1$, $\alpha = 1000$ and $p_b = 0.1$. The orange dashed line shows a constant catastrophe rate $\beta' = 1$.

Cell geometry versus barrier strength

Our first study focuses on cell geometry versus barrier strength. We vary the strength of the barriers (p_b) for three anisotropy angles $\theta_b = \{0^o, 45^o, 90^o\}$ and for eccentricities $= 0.7$ and 0.98, see Figure 3.12. We find that with increasing barrier strength p_b, microtubules progressively align with the angle of anisotropy but the extent of the alignment strongly depends on the cell geometry and the barrier strength.

Since we observed in Chapter 2 that geometry drives microtubule self-organisation, we expect that an almost-circular cells ($ecc = 0.7$) will not greatly impede the microtubule alignment against the anisotropy angle θ_b, while the geometry of elongated cells ($ecc = 0.98$) should have a stronger effect on microtubule self-organisation, and lower the impact of the anisotropy. We see that this indeed happens in our system (Figure 3.12): for the anisotropy angle distinct from the major axis of the cell, the mean microtubule direction for almost circular cells ($ecc = 0.7$) shifts to the anisotropy angle faster than in elongated cells, where we see a longer transition period.

To demonstrate how microtubule angle distribution changes with geometry, anisotropy

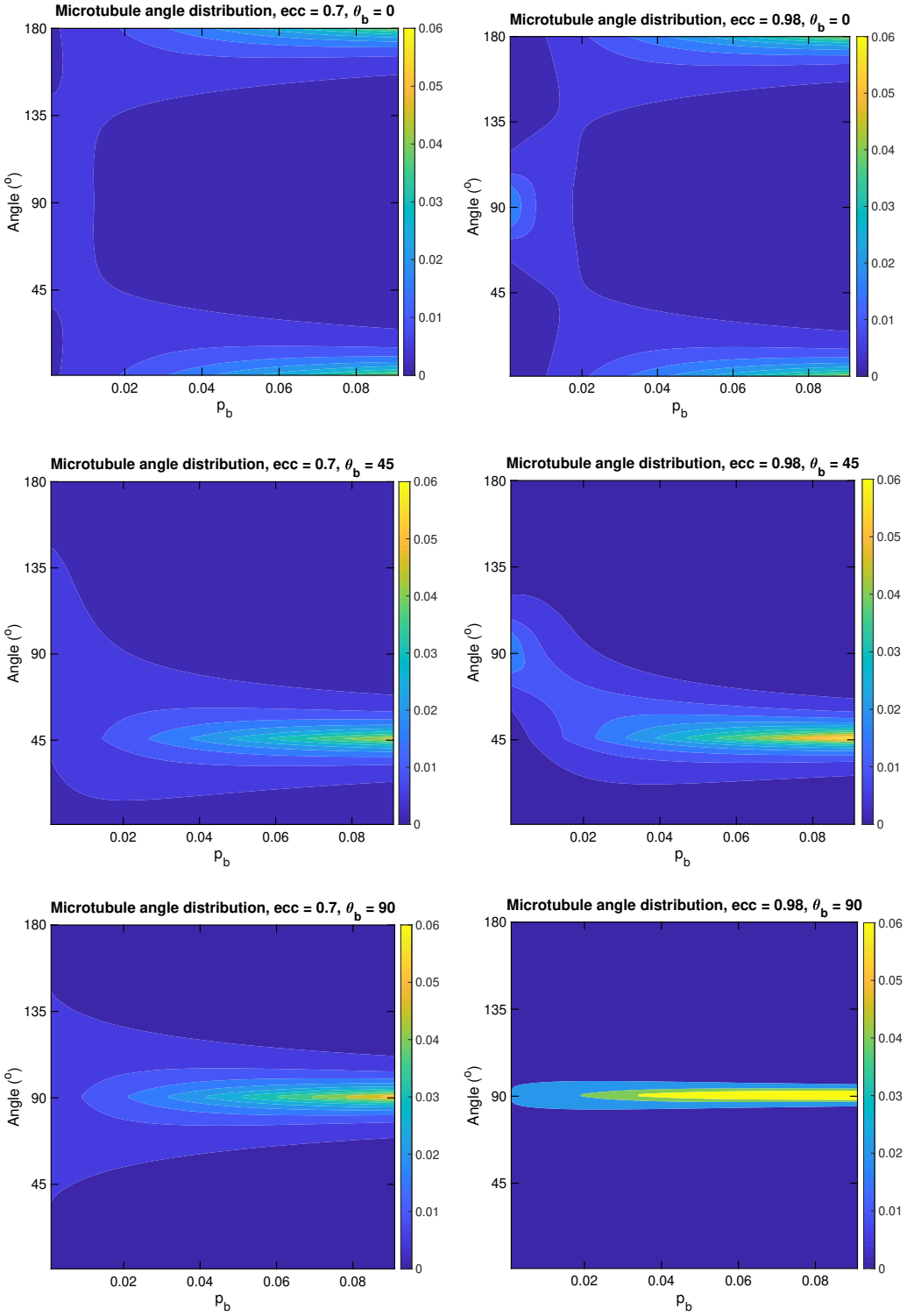

Figure 3.12: The microtubule angle distributions for the case of anisotropic homogeneous barriers (obtained from (3.7)). Left hand side shows cells of $ecc = 0.7$ and right hand side shows cells of $ecc = 0.98$. Parameters not specified in the figure remain at their default value (see Table 3.1). From top to bottom, the anisotropy angle is $0^o, 45^o$ and 90^o.

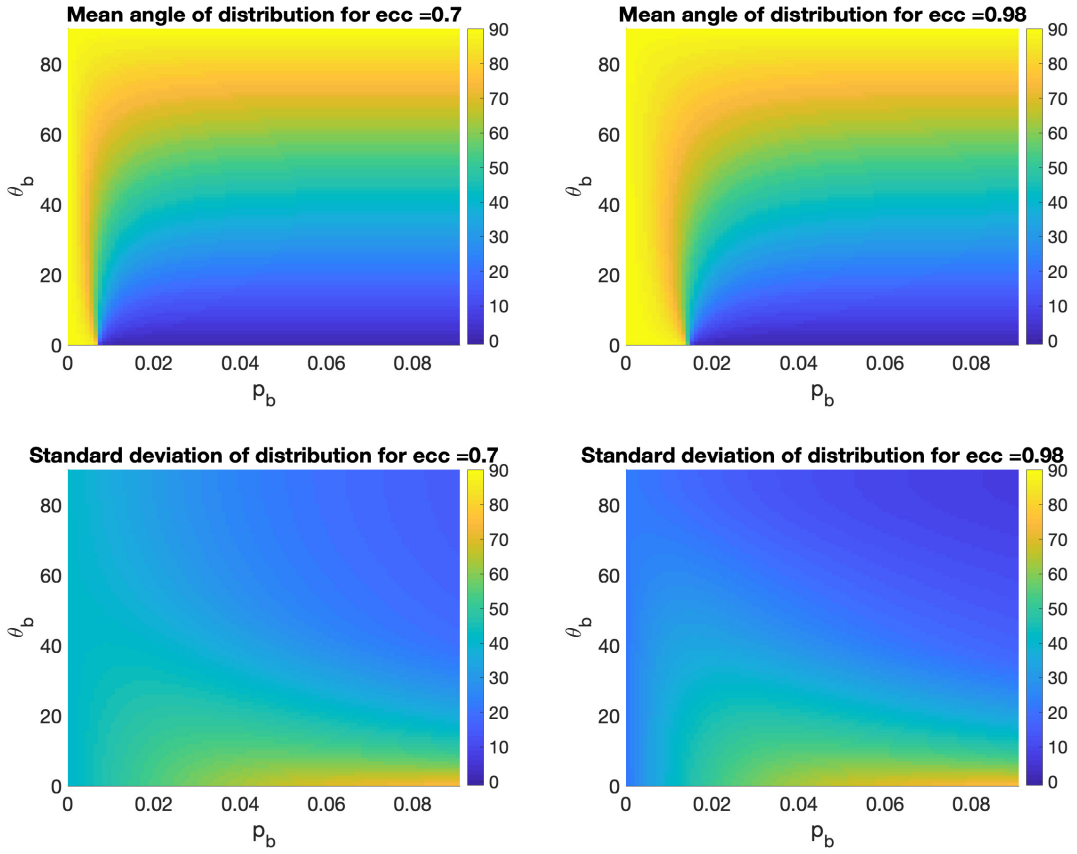

Figure 3.13: The mean (top row) and standard deviation (bottom row) of the microtubule angle distributions for the case of anisotropic homogeneous barriers (obtained from (3.7)). Left hand side shows cells of $ecc = 0.7$ and right hand side shows cells of $ecc = 0.98$. Parameters not specified in the figure remain at their default value (see Table 3.1).

angle θ_b and barrier strength p_b we plot the mean and the standard deviation as a function of θ_b and p_b. We calculate the mean direction of the distribution μ by using the circular mean function in Matlab from Circular Statistics toolbox [14]. The standard deviation is calculated using the Matlab circshift function to circularly shift the microtubule angle distribution $\rho(\phi)$ and calculate

$$var(i) = \sum (\rho(\phi)_i \times abs(\phi - \mu)) \,, \tag{3.9}$$

where $\phi \in [1\,, 180]$ and index i denotes the circular shift index $i \in [1\,, 180]$. We define the standard deviation measure as the $\min_{i\in[1\,,180]} var(i)$. Indeed, we see that geometry affects the point of transition where the microtubule distribution shifts the

mean direction. From Figure 3.13 we see that when barriers are placed perpendicular to the main axis of the cell ($\theta_b = 0$), the mean direction of the distribution changes from the major cell axis direction (90^o) to θ_b at $p_b \approx 0.01$ for cells of eccentricity 0.7 and at $p_b \approx 0.018$ for cells of eccentricity 0.98 .

Although this model serves as an idealisation of anisotropic barriers, we conclude that cell geometry plays an important role on how strongly microtubule alignment responds to anisotropic barriers. In particular, the new important parameter is the angle between the anisotropic barriers and the main axis of the cell. When barriers are aligned along the major cell axis, they will aid organisation, whereas when barriers lie perpendicular to the major cell axis they cause their most disruptive effect on self-organisation. Therefore, for a biological system, it is crucial to consider the angle between the major axis of the cell and the angle of anisotropy to determine whether the barriers will aid or disrupt microtubule self-organisation. The barrier strength parameter demonstrates that the barrier width also impacts the degree to which the anisotropy angle is followed by microtubules. Moreover, weak barriers can provide a transition where microtubule self-organisation is disrupted only slightly and increasing their strength increases the alignment according to the anisotropy of the cell. We hypothesise that the effects of anisotropic barriers are elemental in understanding intracellular transport as the anisotropy and its strength strongly influence the overall transport direction.

3.3.4 Anisotropic discrete barriers

We now consider anisotropic discrete barriers, which we use to model the effect of actin cables in *Drosophila* follicular epithelium. We begin by deriving our final microtubule angle distribution for cells which now include discrete barriers oriented at an angle θ_b and separated by a distance δ (see Figure 3.14).

To derive the mean angle distribution we follow the derivation in Chapter 2 Section 2.2.3. Consider a microtubule seeded at ζ . Our goal is to obtain the length-weighted mean survival time of the microtubule, given that it undergoes dynamic instability, collapses with a higher probability upon reaching a barrier and collapses once it hits the boundary (at length a).

Following (Section 2.2.3 Formula (2.9)), note that the difference $h(x) = f(x) - g(x)$ between the the mean expected survival time of the growing and shrinking state

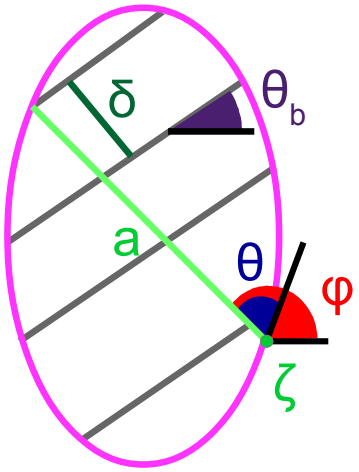

Figure 3.14: Schematic of a cortical microtubule in an epithelial cell. The cell boundary is parameterised by the coordinate ζ. A microtubule is seeded at the point ζ and grows at an angle φ with respect to the horizontal and angle θ with respect to the cell boundary. The angle θ_b denotes the angle of the barrier with respect to the horizontal and δ denotes the spacing between barriers. The microtubule can grow length a until it reaches the cell boundary.

satisfies the ODE

$$\frac{dh(x)}{dx} = p(x)h(x) - q\gamma(x)\,, \tag{3.10}$$

where $q = \frac{1}{\alpha} + \frac{1}{\beta}$, $\gamma(x)$ is the time weighting function and we now define the catastrophe as a function of x, by stating that $p = \frac{\beta'(x)}{\alpha} - \frac{\alpha'}{\beta}$. To model anisotropic discrete barriers we use

$$p(x) \;=\; p_0 + p_1 \sum_{k=1}^{N(x,0,\zeta,\theta)} (H(x - kL(\zeta,\theta) + \varepsilon) - H(x - kL(\zeta,\theta) - \varepsilon)). \tag{3.11}$$

where $p_0 = \left(\frac{\beta'}{\alpha} - \frac{\alpha'}{\beta}\right)$ and $p_1 = A\frac{\beta'}{\alpha}$. We note that

$$\begin{aligned}
\int_0^x p(s)ds &= p_0 x + p_1 \sum_{k=1}^{N(x,0,\zeta,\theta)} 2\varepsilon, && (3.12)\\
&= p_0 x + 2\varepsilon p_1 N(x,0,\zeta,\theta), && (3.13)\\
&= p_0 x + p_2 N(x,0,\zeta,\theta), && (3.14)
\end{aligned}$$

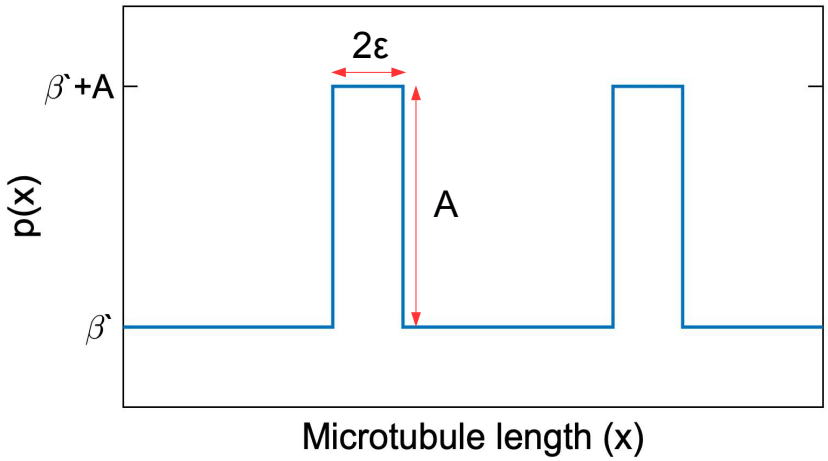

Figure 3.15: Function $p(x)$ (3.11) for modelling anisotropic discrete microtubule shows how the barrier strength changes the parameter p with increasing microtubule length x. Here the width of a barrier is 2ϵ and changes the probability of catastrophe from β' to $\beta' + A$.

where $p_0 = \left(\frac{\beta'}{\alpha} - \frac{\alpha'}{\beta}\right)$ and $p_2 = 2\epsilon A\frac{\beta'}{\alpha}$. $N(b, a, \zeta, \theta) = \lceil b/L(\zeta, \theta\rceil - \lceil a/L(\zeta, \theta\rceil$ counts how many barriers have been passed for a seed ζ at angle θ with a microtubule growing from length a to length b along that segment, hence we consider $N(x, 0, \zeta, \theta)$ as how many barriers are encountered by a microtubule in its length x. We can plot the function $p(x)$ (3.11) as seen in Figure 3.15. Hence, we calculate that for a given barrier strength p_b the corresponding catastrophe rate is defined as

$$\frac{rate_{catastrophe}}{rate_{catastrophe} + \alpha} = \frac{p_b}{1 - p_b}, \tag{3.15}$$

and hence

$$A = \frac{\alpha p_b}{1 - p_b} - \beta'. \tag{3.16}$$

Using (3.11) and (3.16) we can now derive the microtubule angle distribution for discrete anisotropic barriers. First, including no length weighting (by using $\gamma(x) = 1$

in (3.10)) we find that the mean survival time is given by:

$$\frac{dh(x)}{dx} = p(x)h(x) - q, \quad h(a) = 0, \tag{3.17}$$

$$h(x) = -q\int_0^x e^{\int_y^x p(s)ds}dy + c_1 e^{\int_0^x p(s)ds} \tag{3.18}$$

We can now use the boundary condition that $h(a) = 0$ to obtain

$$c_1 = e^{-\int_0^a p(s)ds} q\int_0^a e^{\int_y^a p(s)ds}dy\,, \tag{3.19}$$

$$= q\int_0^a e^{-\int_0^y p(s)ds}dy\,. \tag{3.20}$$

Therefore, we find that

$$h(x) = q\int_x^a e^{\int_y^x p(s)ds}dy\,, \tag{3.21}$$

and hence we can use (3.14) to obtain

$$h(0) = q\int_0^a e^{-\int_0^y p(s)ds}dy\,, \tag{3.22}$$

$$= q\int_0^a e^{-p_0 y - p_2 N(y,0,\zeta,\theta}dy\,. \tag{3.23}$$

The average lifetime (not length-weighted) of a microtubule seeded at the position ζ, averaged over the angles $\theta \in (0,\pi)$ of microtubule dimers at the seed, is

$$T_{ave,0} = \frac{q}{\pi}\int_0^\pi \int_0^a e^{-p_0 z - p_2 N(z,0,\zeta,\theta)}\,dz\,d\theta. \tag{3.24}$$

To include length-weighting (by using $\gamma(x) = x$ in (3.10)) into the lifetime of a microtubule we solve

$$h'(x) = p(x)h(x) - qx, \quad h(a) = 0, \tag{3.25}$$

$$h(x) = -q\int_0^x e^{\int_z^x p(s)ds} z dz + c_2 e^{\int_0^x p(s)ds} \tag{3.26}$$

We can use the boundary condition, $h(a) = 0$, to obtain

$$c_2 = q \int_0^a e^{\int_z^a p(s)ds} e^{\int_a^0 p(s)ds} z dz, \tag{3.27}$$

$$= q \int_0^a e^{\int_z^0 p(s)ds} z dz. \tag{3.28}$$

We are only interested in $f(0) = h(0)$ and we use (3.14) again to obtain

$$f(0) = q \int_0^a e^{-\int_0^z p(s)ds} z dz, \tag{3.29}$$

$$= q \int_0^a e^{-p_0 z - p_2 N(z,0,\zeta,\theta)} z dz. \tag{3.30}$$

Thus the average contribution of the length-weighted microtubule lifetime in one lifetime is:

$$T_{ave,1} = q \int_0^a e^{-p_0 z - p_2 \mathbf{N}(z,0,\zeta,\theta)} z \, dz. \tag{3.31}$$

Finally, we combine the previous results to derive the full microtubule angle distribution. In a large enough time T, the microtubule grows a large number of times $n >> 1$ in various directions, separated by gaps of length $1/\alpha'$ when the microtubule has zero length. We are interested in the time integral $\int_0^T l(t)dt$ of the length $l(t)$ of a microtubule weighted by the length x at time t in the direction $(\phi, \phi + \delta\phi)$.

Hence the average time spent for lifetime and waiting in the zero state is

$$\frac{T}{n} \approx \left(\frac{1}{\alpha'} + T_{ave,0} \right). \tag{3.32}$$

The contribution of microtubules growing in the direction $(\phi, \phi + \delta\phi)$ is proportional to n and the length-weighted lifetime $T_{ave,1}$:

$$\rho(\phi)\delta\phi \sim \int n \frac{\delta\phi}{\pi} T_{ave,1} \, d\zeta, \tag{3.33}$$

$$= \int \frac{T}{\frac{1}{\alpha'} + T_{ave,0}} \frac{\delta\phi}{\pi} T_{ave,1} \, d\zeta, \tag{3.34}$$

Hence, the microtubule angle distribution, $\rho(\phi)$, is given by

$$\frac{1}{M}\int \frac{\int_0^{\tilde{a}(\zeta,\phi)} e^{-p_0 z - p_2 \tilde{\mathbf{N}}(z,0,\zeta,\phi)} z\, dz}{1+\frac{q\alpha'}{\pi}\int_0^{\pi}\int_0^{a(\zeta,\theta)} e^{-p_0 z - p_2 N(z,0,\zeta,\theta)}\, dz\, d\theta}\, d\zeta, \tag{3.35}$$

where M is the normalization constant. The constants $p_0 = \left(\frac{\beta'}{\alpha} - \frac{\alpha'}{\beta}\right)$ and $p_2 = 2\epsilon A\frac{\beta'}{\alpha}$ where $A = \frac{\alpha p_b}{1-p_b} - \beta'$. The function $N(x,0,\zeta,\theta)$ counts the number of barriers a microtubule has intersected growing length x from its seed state situated at ζ with angle θ. Note that here, $\tilde{a}(\zeta,\phi)$ is length of a cross-section of the cell that starts at the point ζ on the boundary of the cell and has angle ϕ with respect to the horizontal, so the length-weighted microtubule survival time is calculated with respect to ϕ. However for the not length-weighted mean survival time we consider the time spent by microtubules growing uniformly between $[0,\pi]$ with respect to the boundary so $a(\zeta,\theta)$ defines the length of a cross-section of the cell that starts at point ζ on the boundary of the cell and has angle θ with respect to the cell boundary.

To study the dependence of microtubule orientation on discrete anisotropic barriers inside the cell we vary the cell geometry, the angle of anisotropy θ_b, the barrier strength p_b and the spacing between barriers δ . The results (Figures 3.16, 3.17, 3.18, 3.19, 3.20, 3.21) mimic observations drawn from the case of anisotropic homogeneous barriers. We note the agreement between the stochastic simulations and the analytic formula under the full parameter regime. Further, we see that increasing the barrier strength p_b shifts the mean of the microtubule angle distribution to θ_b and decreases the standard deviation of the distribution. Finally, we observe the same transition in which the effect of geometry on driving microtubule self-organisation is overcome when the oriented barriers reach a critical strength. The biggest effect on the microtubule angle distributions occurs when the cell major axis lies perpendicular to the angle of anisotropy θ_b .

Comparison with experiments

Our collaborator compared our results to an experimental system using tissue from the *Drosophila* follicular epithelium. Here actin cables lie throughout the adhesion plane of the cells where the microtubules are located. The microtubule angle distribution is measured for cells from the *Drosophila* follicular epithelium and then actin cables are removed with the use of $2\mu M$ of Latrunculin A applied for 15 minutes and the microtubule angle distribution is measured. Applying Latrunculin A for 15

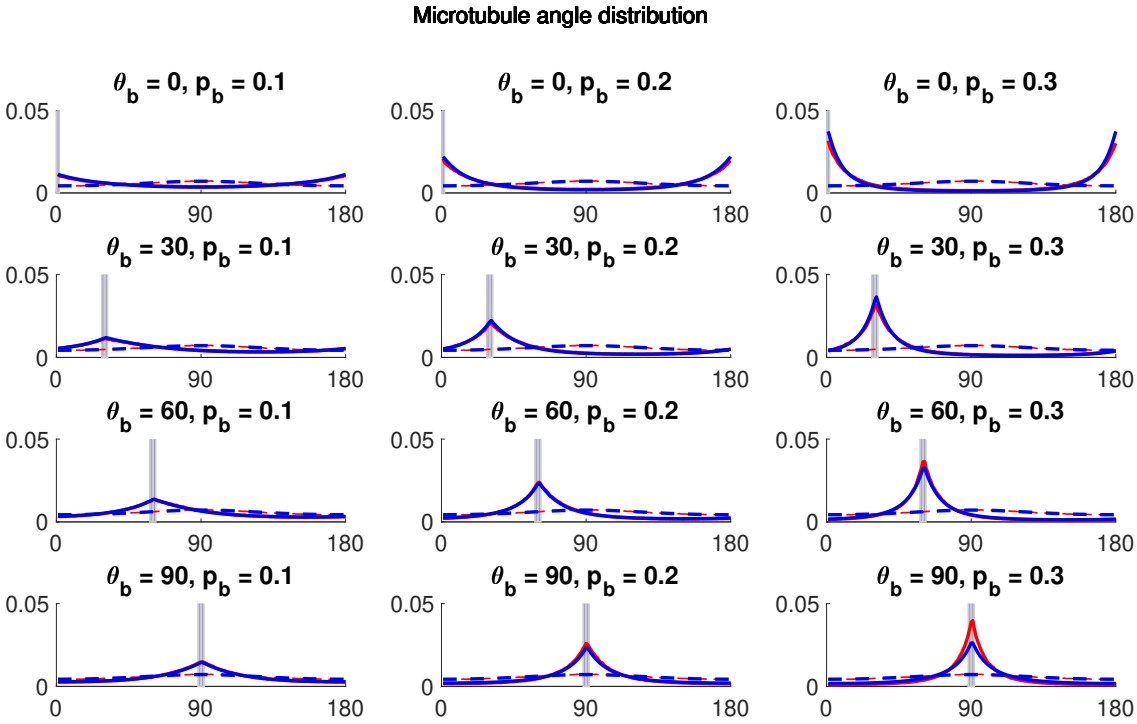

Figure 3.16: Microtubule angle distributions for the case of discrete barriers of strength p_b at an angle θ_b with respect to the horizontal and with spacing $\delta = 5$ between the barriers. Results of stochastic simulations (2.2) (red lines) for $ecc = 0.7$ and analytic results (blue lines), using (3.35). The corresponding control microtubule angle distribution with stochastic simulations (dashed red lines) and analytic results (dashed blue lines) are also computed using the isotropic homogeneous barriers with default parameters. Vertical grey lines demonstrate the angles of anisotropy. Parameters not specified in the figure remain at their default value (see Table 3.1).

minutes results in the removal of actin cables in the cell interior without breaking the cortical actin at the cell boundary. These experiments are very fragile since applying a higher drug concentration or exposing the cell to the drug over a longer time might result in the removal of cortical actin and the cell would break. The experimentally obtained microtubule angle distribution from cells with actin cables in *Drosophila* follicular epithelium suggest that actin cables can act as weak barriers for polymerising microtubules (see Figure 3.22). In early stages of development ($ecc = 0.7\,, 0.8$), actin does not have much influence on the microtubule cytoskeleton. At these stages the actin cables lie at 45^o to the minor axis of the cell and therefore neither improve nor weaken organisation. However, during later stages of development ($ecc = 0.9\,, 0.98$)

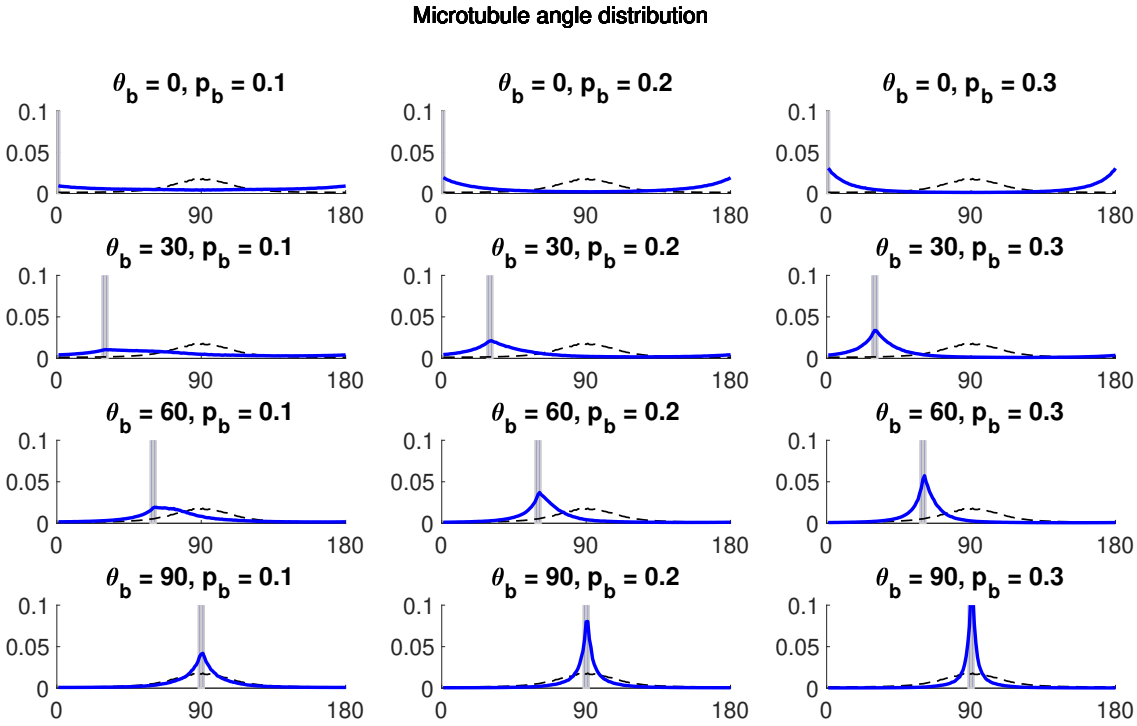

Figure 3.17: Microtubule angle distributions for the case of discrete barriers of strength p_b at an angle θ_b with respect to the horizontal and with spacing $\delta = 5$ between the barriers. Results of stochastic simulations (2.2) (blue lines) for $ecc = 0.98$. The corresponding control microtubule angle distribution with stochastic simulations (dashed black lines) are computed using the isotropic homogeneous barriers with default parameters. Vertical grey lines demonstrate the angles of anisotropy. Parameters not specified in the figure remain at their default value (see Table 3.1).

actin cables lie perpendicular to the major axis of the cell and therefore weaken the organisation of the microtubule cytoskeleton: we see the standard deviations of the distributions increase (see Figure 3.22).

3.4 Bundling factor

3.4.1 Setup

In vivo, a growing microtubule can change its direction and continue to grow along another microtubule upon their crossing in the presence of cross-linking proteins. When several microtubules grow along each other in the same direction we say that

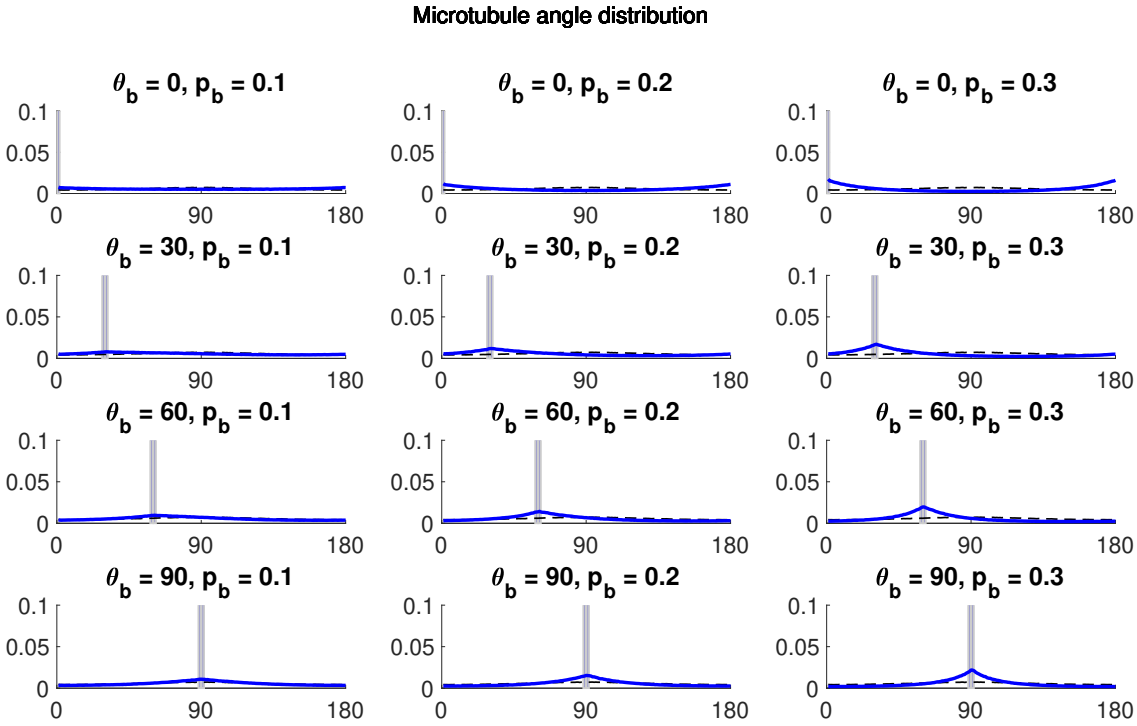

Figure 3.18: Microtubule angle distributions for the case of discrete barriers of strength p_b at an angle θ_b with respect to the horizontal and with spacing $\delta = 10$ between the barriers. Results of stochastic simulations (2.2) (blue lines) for $ecc = 0.7$. The corresponding control microtubule angle distribution with stochastic simulations (dashed black lines) are computed using the isotropic homogeneous barriers with default parameters. Vertical grey lines demonstrate the angles of anisotropy. Parameters not specified in the figure remain at their default value (see Table 3.1).

they form a bundle, see Figure 3.23. Since intracellular transport is achieved via molecular motors trafficking cargo along microtubules, we hypothesise that bundling strongly affects transport through prolonging its direction. In our simulations, the time-scale for the lifetime of an individual microtubule is much shorter than the time-scale of a bundle, which can be up to an order of magnitude longer.

We study bundling in the following cases of anisotropic cytoplasm: isotropic homogeneous barriers, isotropic discrete barriers and anisotropic discrete barriers. To study bundling, we calculate two new quantities: the microtubule bundles angle distribution and the bundling factor, which we define as the percentage of length of microtubules in bundles over the total length of microtubules.

To numerically calculate which microtubules are in a bundle we make use of the

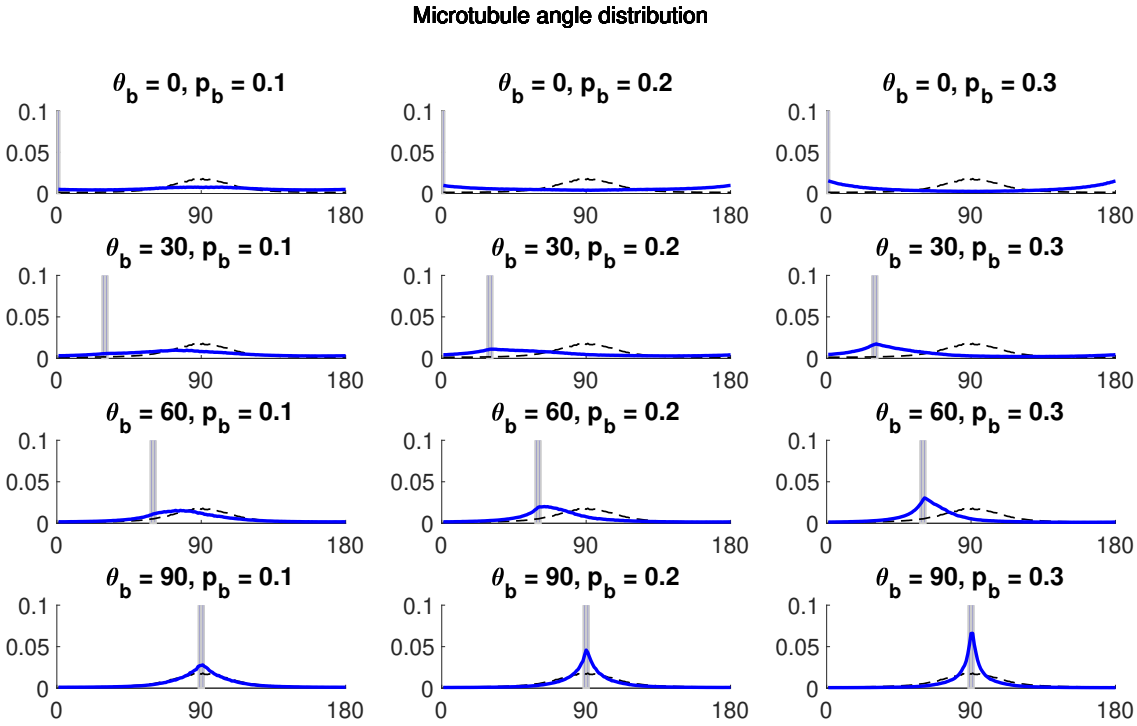

Figure 3.19: Microtubule angle distributions for the case of discrete barriers of strength p_b at an angle θ_b with respect to the horizontal and with spacing $\delta = 10$ between the barriers. Results of stochastic simulations (2.2) (blue lines) for $ecc = 0.98$. The corresponding control microtubule angle distribution with stochastic simulations (dashed black lines) are computed using the isotropic homogeneous barriers with default parameters. Vertical grey lines demonstrate the angles of anisotropy. Parameters not specified in the figure remain at their default value (see Table 3.1).

assumptions we made for microtubules to zip in the code. If a microtubule A zips along another microtubule B we add a new segment to microtubule A that has the same angle as the microtubule B. In this way we can check that microtubules are part of the same bundle by first considering if they have the same angle and then introducing a small measure ϵ. We go through all microtubule segments and count how many other microtubules dimers are within a distance ϵ to the microtubule segment. We construct the microtubule angle distribution by counting how many microtubule dimers which are part of bundles are at a given angle. We further calculate the bundling factor by counting the number of dimers in bundles over the total number of microtubules.

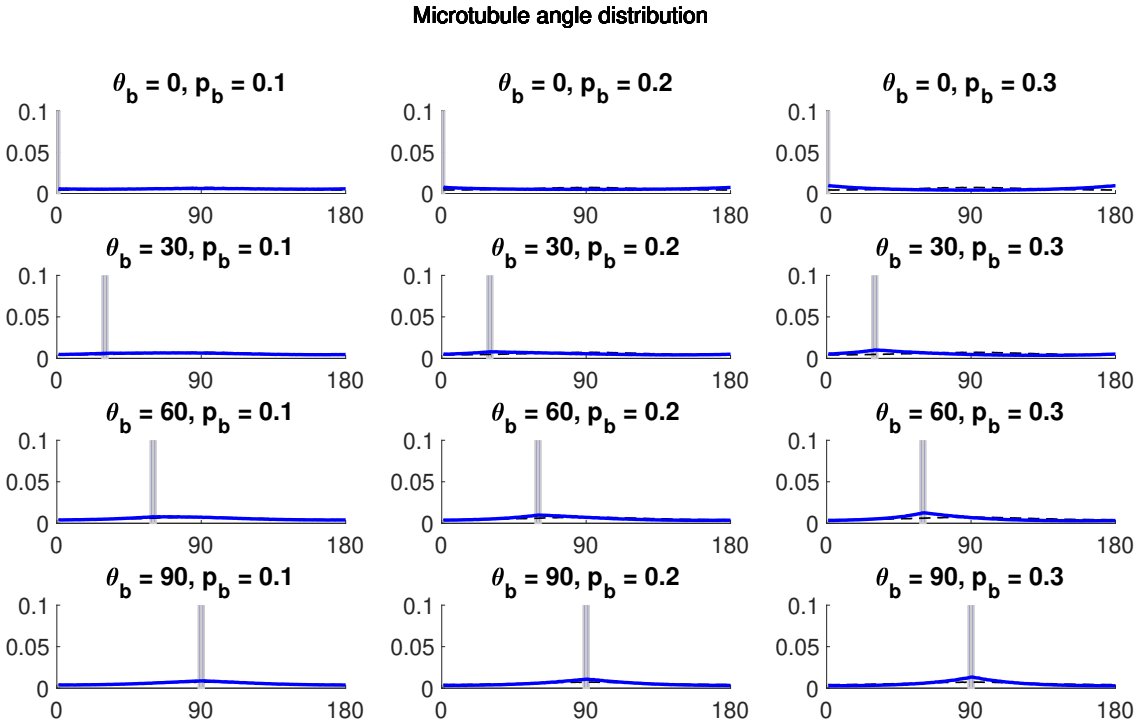

Figure 3.20: Microtubule angle distributions for the case of discrete barriers of strength p_b at an angle θ_b with respect to the horizontal and with spacing $\delta = 20$ between the barriers. Results of stochastic simulations (2.2) (blue lines) for $ecc = 0.7$. The corresponding control microtubule angle distribution with stochastic simulations (dashed black lines) are computed using the isotropic homogeneous barriers with default parameters. Vertical grey lines demonstrate the angles of anisotropy. Parameters not specified in the figure remain at their default value (see Table 3.1).

3.4.2 Isotropic homogeneous barriers

First we study bundling in isotropic homogeneous barriers, modelled by changing the collision parameters between microtubules: the critical collision angle θ_c and the probability of catastrophe p_{cat} (3.3 A). We find that these changes only slightly affect the microtubule bundles angle distribution (see Figures 3.24,3.25). As the critical collision angle θ_c decreases, the distribution gets more peaked, while increasing the probability of catastrophe p_{cat} adds noise to the distribution. However, the mean direction remains the same and the standard deviation changes only slightly. Furthermore, the bundling factor decreases with increasing p_{cat} and decreasing θ_c (see Figure 3.26). Figure 3.26 shows that increasing p_{cat} and decreasing θ_c decreases the

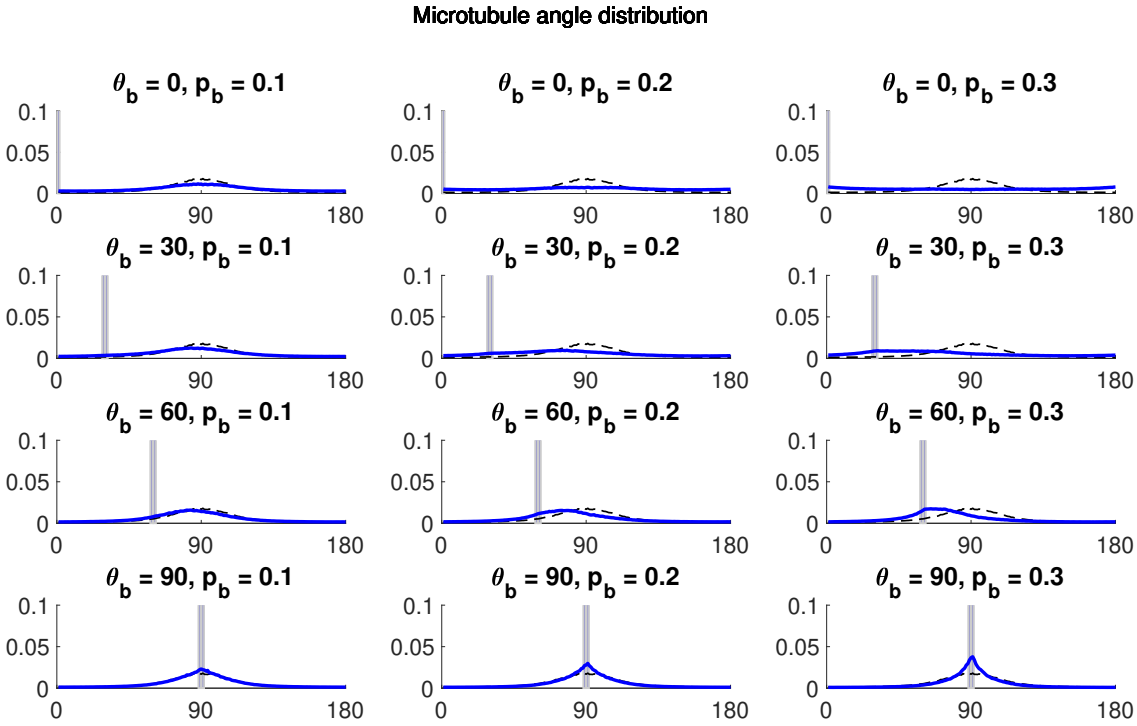

Figure 3.21: Microtubule angle distributions for the case of discrete barriers of strength p_b at an angle θ_b with respect to the horizontal and with spacing $\delta = 20$ between the barriers. Results of stochastic simulations (2.2) (blue lines) for $ecc = 0.98$. The corresponding control microtubule angle distribution with stochastic simulations (dashed black lines) are computed using the isotropic homogeneous barriers with default parameters. Vertical grey lines demonstrate the angles of anisotropy. Parameters not specified in the figure remain at their default value (see Table 3.1).

percentage of total microtubule lengths in bundles.

3.4.3 Isotropic discrete barriers

Next we consider the isotropic case, where N_b barriers are placed randomly inside the cell (see Figure 3.3B). Here we vary the number of barriers N_b and the probability of collapse at the given barrier p_b. Increasing N_b and p_b adds noise to the distribution, whereas the mean direction and standard deviations do not significantly change (see Figures 3.27, 3.28). Furthermore, the bundling factor is decreased for increasing N_b and p_b (see Figure 3.29).

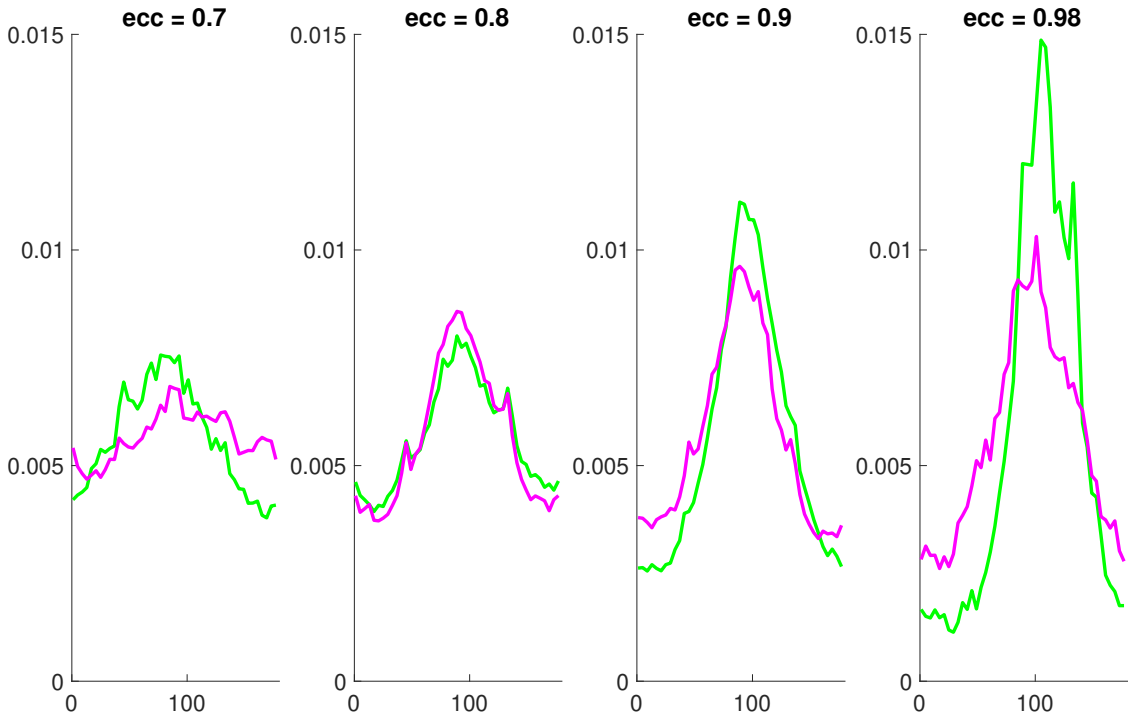

Figure 3.22: Microtubule angle distribution calculated from experiments on various cell eccentricies of the *Drosophila* follicular epithelium with no actin (green) and actin cables (magenta).

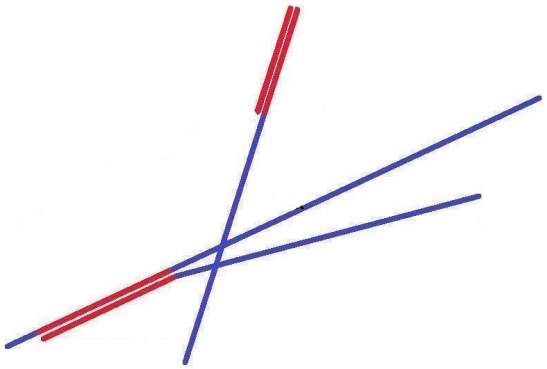

Figure 3.23: The schematic shows single microtubule filaments (blue) forming microtubule bundles (red). Only the parts of the microtubules which are growing alongside a neighbouring microtubule (either due to zipping or proximity) are included in the computation of a bundle.

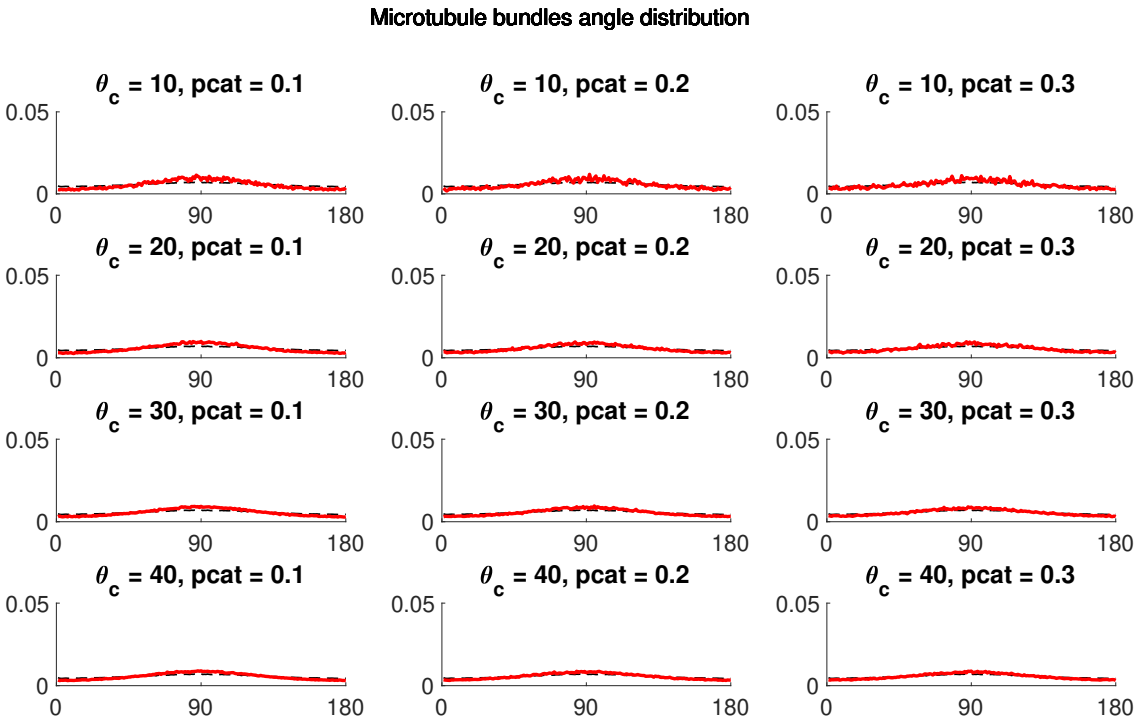

Figure 3.24: The microtubule bundles angle distribution (2.2) (red line) for the case of isotropic homogeneous barriers in cells of $ecc = 0.7$. The corresponding control microtubule angle distribution (dashed black line) of the isotropic homogeneous barriers with default parameters. Parameters not specified in the figure remain at their default value (see Table 3.1).

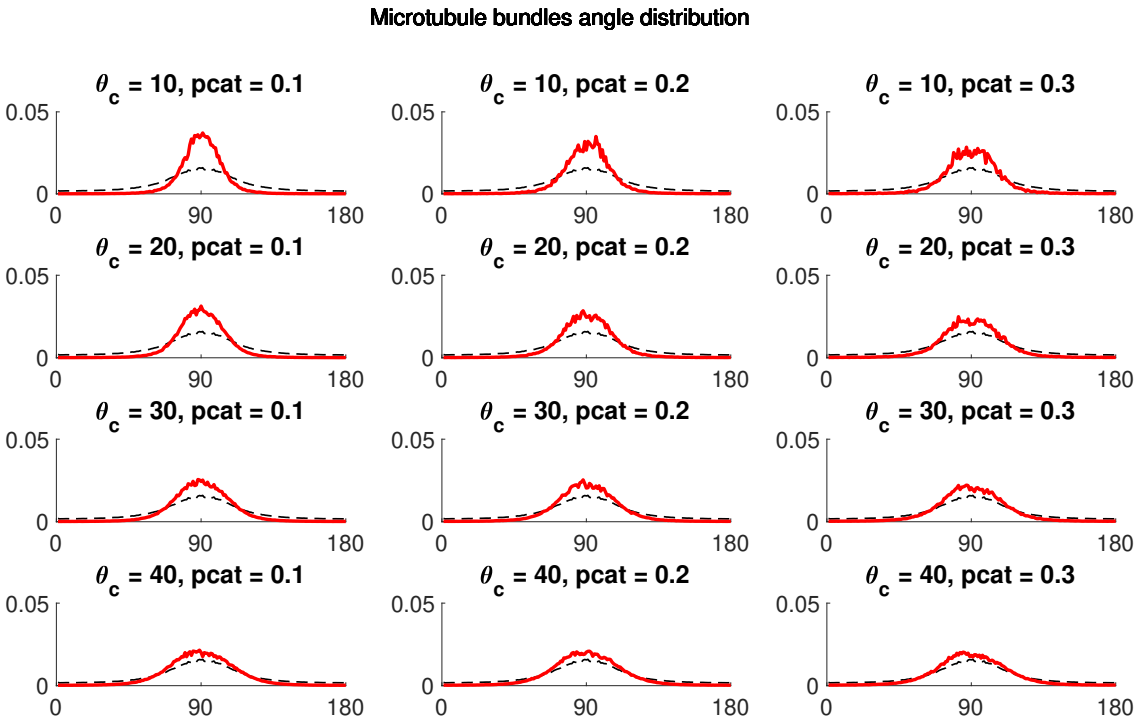

Figure 3.25: The microtubule bundles angle distribution (2.2) (red line) for the case of isotropic homogeneous barriers in cells of $ecc = 0.98$. The corresponding control microtubule angle distribution (dashed black line) of the isotropic homogeneous barriers with default parameters. Parameters not specified in the figure remain at their default value (see Table 3.1).

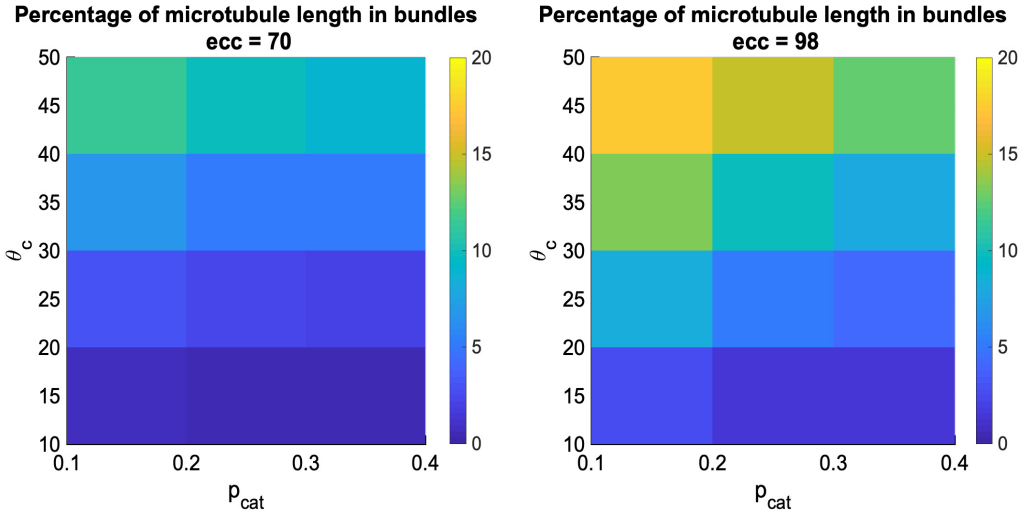

Figure 3.26: The bundling factor for the case of isotropic homogeneous barriers in cells using stochastic simulations with $ecc = 0.7$ (left) and 0.98 (right) computed using (2.2). Parameters not specified in the figure remain at their default value (see Table 3.1).

3.4.4 Anisotropic discrete barriers

Finally, we consider the case of anisotropic barriers inside the cell, of strength p_b placed at an angle θ_b with respect to the horizontal and separated by a distance δ. Increasing the strength of the barriers p_b and decreasing their spacing δ skews the microtubule bundle distribution, so that the mean direction of bundles is now in the anisotropy direction (see Figures 3.30, 3.31, 3.32, 3.33, 3.34, 3.35). Decreasing δ and shifting angle θ_b from 90^o to 0^o decreases the bundling factor (see Figure 3.36, 3.37, 3.38).

To summarise, our results show that given the same barrier strength p_b anisotropic barriers have a much bigger impact on the self-organisation of microtubule bundles than isotropic barriers. While isotropic barriers do not change the mean direction or the standard deviation of the distributions, anisotropic barriers redirect microtubules in the direction of the barrier. Thus, we hypothesise that the direction of anisotropic barriers inside the cell strongly influences the direction of the microtubule bundles and, therefore, transport.

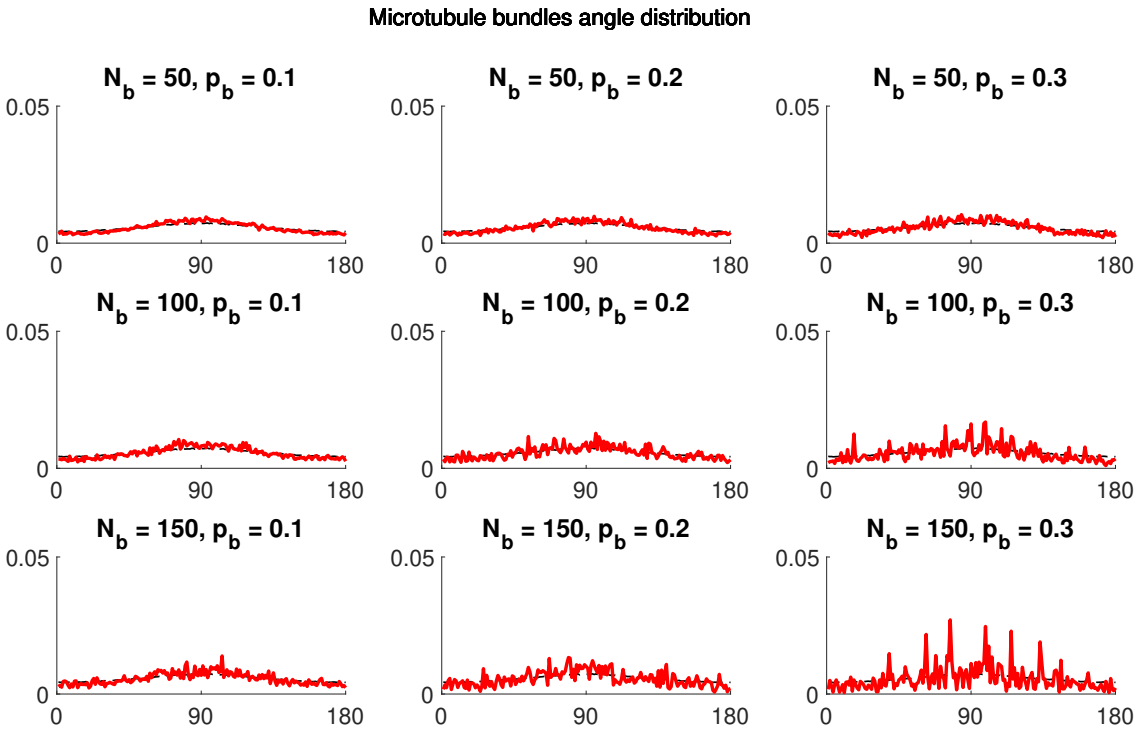

Figure 3.27: The microtubule bundles angle distribution (3.4) (red line) for the case of isotropic discrete barriers in cells with $ecc = 0.7$. The corresponding control microtubule angle distribution (dashed black lines) of the isotropic homogeneous barriers with default parameters. Parameters not specified in the figure remain at their default value (see Table 3.1).

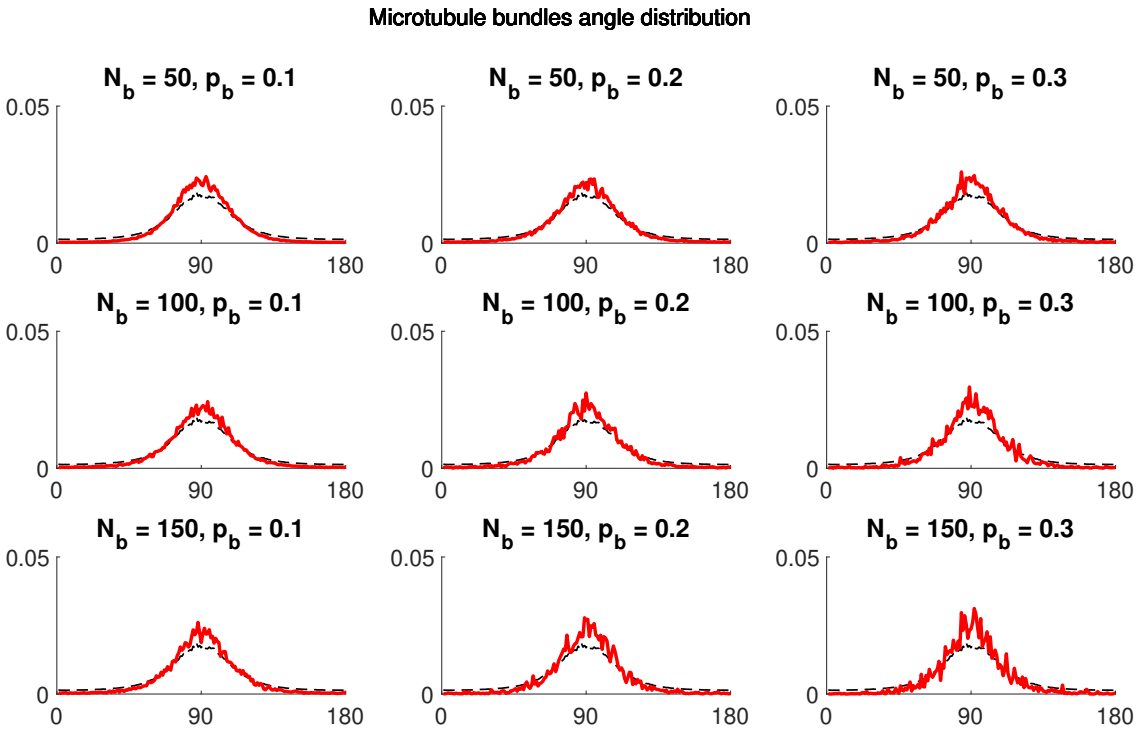

Figure 3.28: The microtubule bundles angle distribution (3.4) (red line) for the case of isotropic discrete barriers in cells with $ecc = 0.98$. The corresponding control microtubule angle distribution (dashed black lines) of the isotropic homogeneous barriers with default parameters. Parameters not specified in the figure remain at their default value (see Table 3.1).

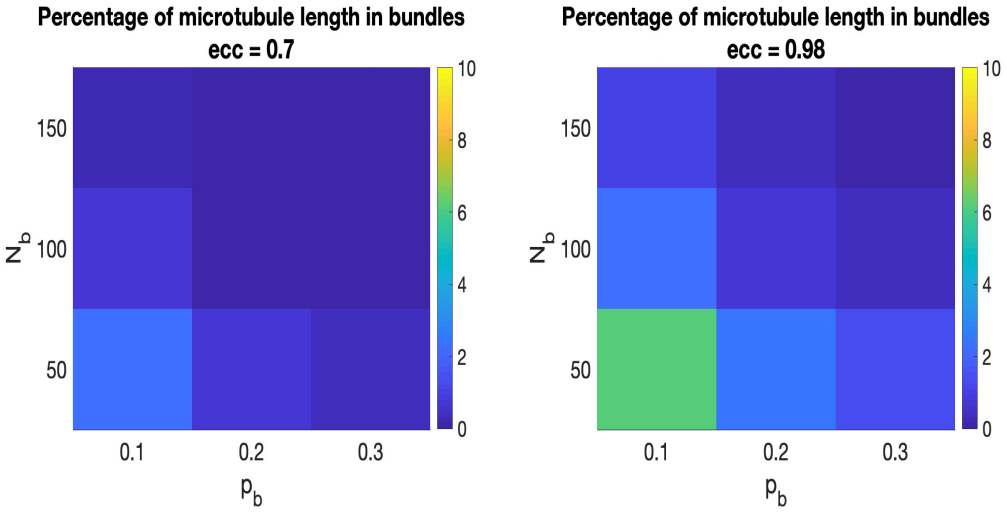

Figure 3.29: The bundling factor for the case of isotropic discrete barriers in cells with $ecc = 0.7, 0.98$ (3.4). Parameters not specified in the figure remain at their default value (see Table 3.1).

3.5 Discussion

3.5.1 Summary

In this Chapter we have discussed the often overlooked question of the effect of a crowded cytoplasm on microtubule self-organisation. We explored various strengths of isotropic and anisotropic barriers using both probabilistic models and stochastic simulations, taking into account homogeneous and discrete barriers. We created a new measure of microtubule self-organisation by measuring microtubule bundles: counting microtubules which have zipped along each other due to the presence of cross-linking proteins. We note that the dynamics of cross-linking proteins or their amount is not modelled as we focus on modelling the resulting outcome of cross-linking proteins but we do not focus on their behaviour. Finally, we have discussed how our model relates to *in vivo* tissue by considering experimental results on the *Drosophila* follicular epithelium. Our model is a simplification of the effects of cell crowding on the self-organisation of microtubules. One of its biggest advantages is that the simplified model gives clear conclusions: anisotropy in cells aligns microtubules to the direction of anisotropy and barriers decrease microtubule bundles. These conclusions can help predict the existence of barriers in a system or their direction. However, one of the biggest limitation of this model is its 2D nature; to

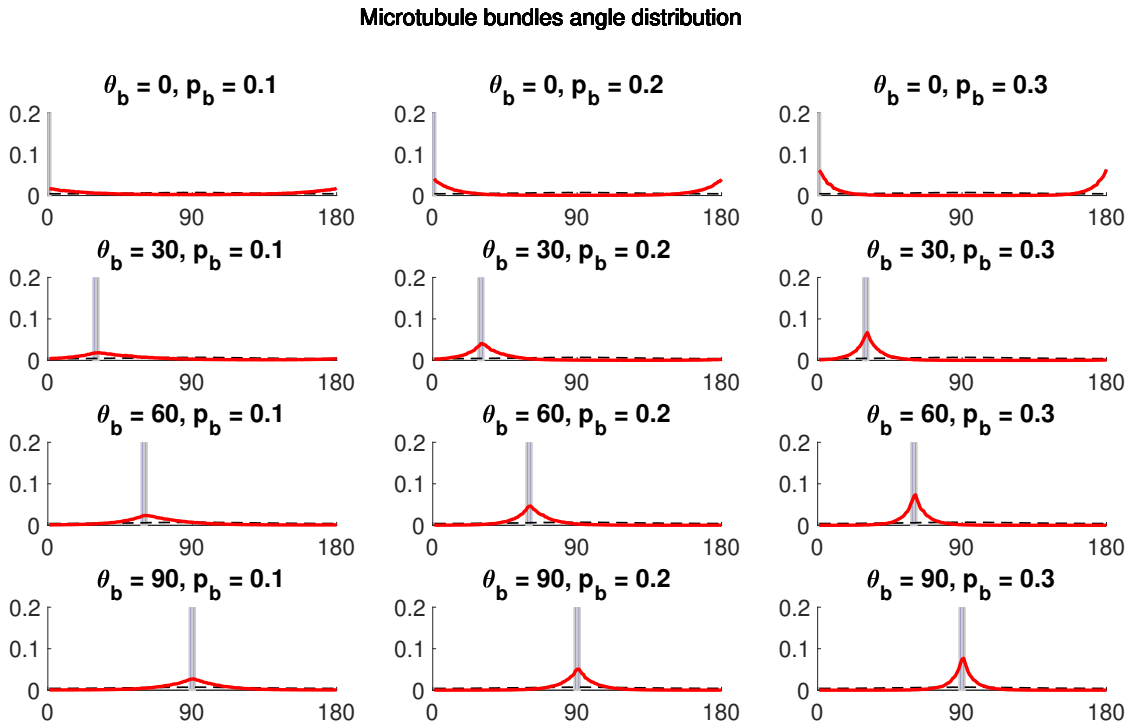

Figure 3.30: The microtubule bundles angle distribution (3.4) (red line) for the case of anisotropic discrete barriers in cells with $ecc = 0.7, \delta = 5$. The corresponding control microtubule angle distribution (dashed black lines) of the isotropic homogeneous barriers with default parameters. Vertical grey lines demonstrate the angles of anisotropy. Parameters not specified in the figure remain at their default value (see Table 3.1).

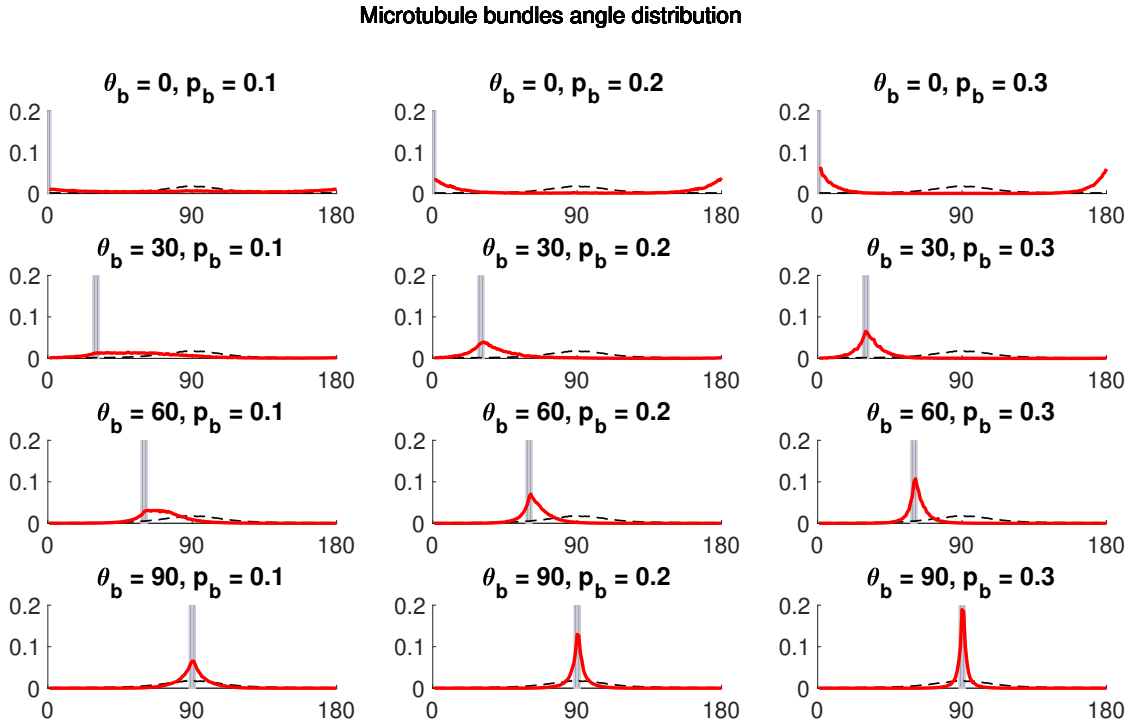

Figure 3.31: The microtubule bundles angle distribution (3.4) (red line) for the case of anisotropic discrete barriers in cells with $ecc = 0.98, \delta = 5$. The corresponding control microtubule angle distribution (dashed black lines) of the isotropic homogeneous barriers with default parameters. Vertical grey lines demonstrate the angles of anisotropy. Parameters not specified in the figure remain at their default value (see Table 3.1).

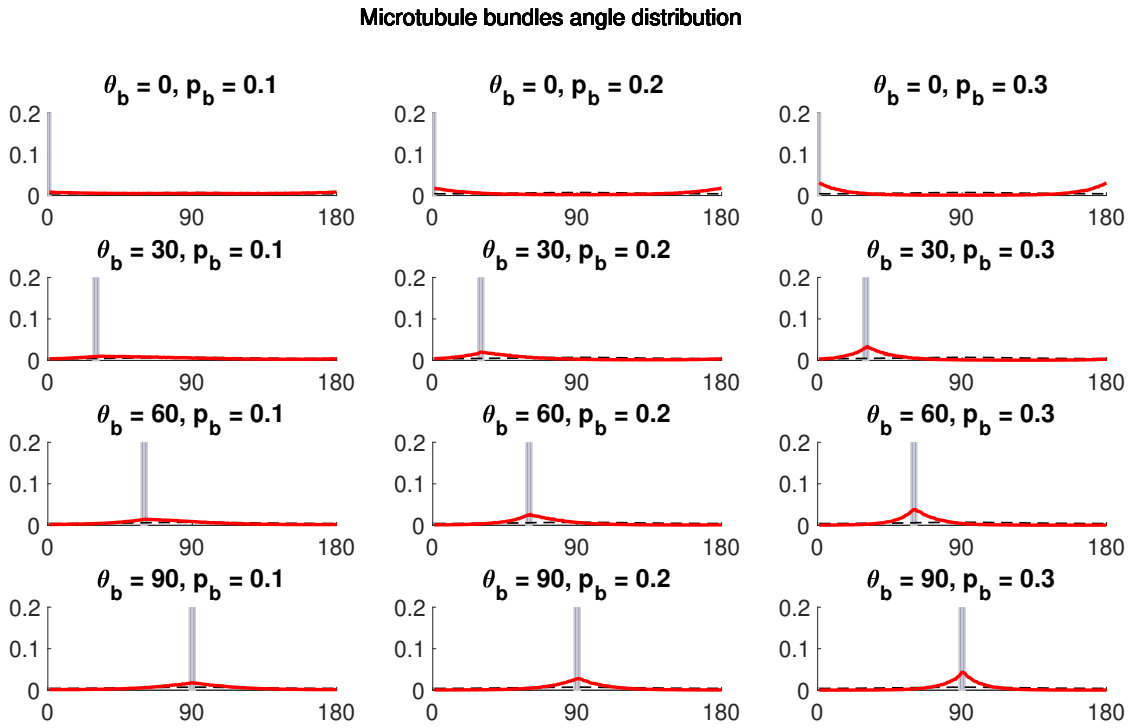

Figure 3.32: The microtubule bundles angle distribution (3.4) (red line) for the case of anisotropic discrete barriers in cells with $ecc = 0.7, \delta = 10$. The corresponding control microtubule angle distribution (dashed black lines) of the isotropic homogeneous barriers with default parameters. Vertical grey lines demonstrate the angles of anisotropy. Parameters not specified in the figure remain at their default value (see Table 3.1).

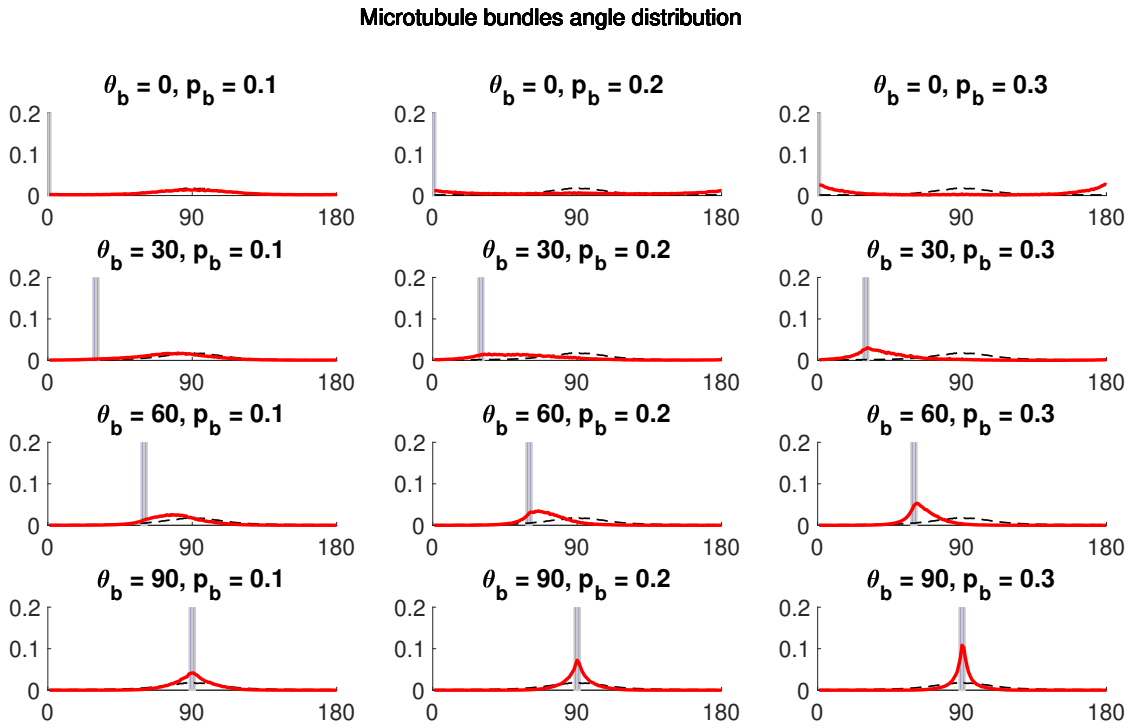

Figure 3.33: The microtubule bundles angle distribution (3.4) (red line) for the case of anisotropic discrete barriers in cells with $ecc = 0.98\,, \delta = 10$. The corresponding control microtubule angle distribution (dashed black lines) of the isotropic homogeneous barriers with default parameters. Vertical grey lines demonstrate the angles of anisotropy. Parameters not specified in the figure remain at their default value (see Table 3.1).

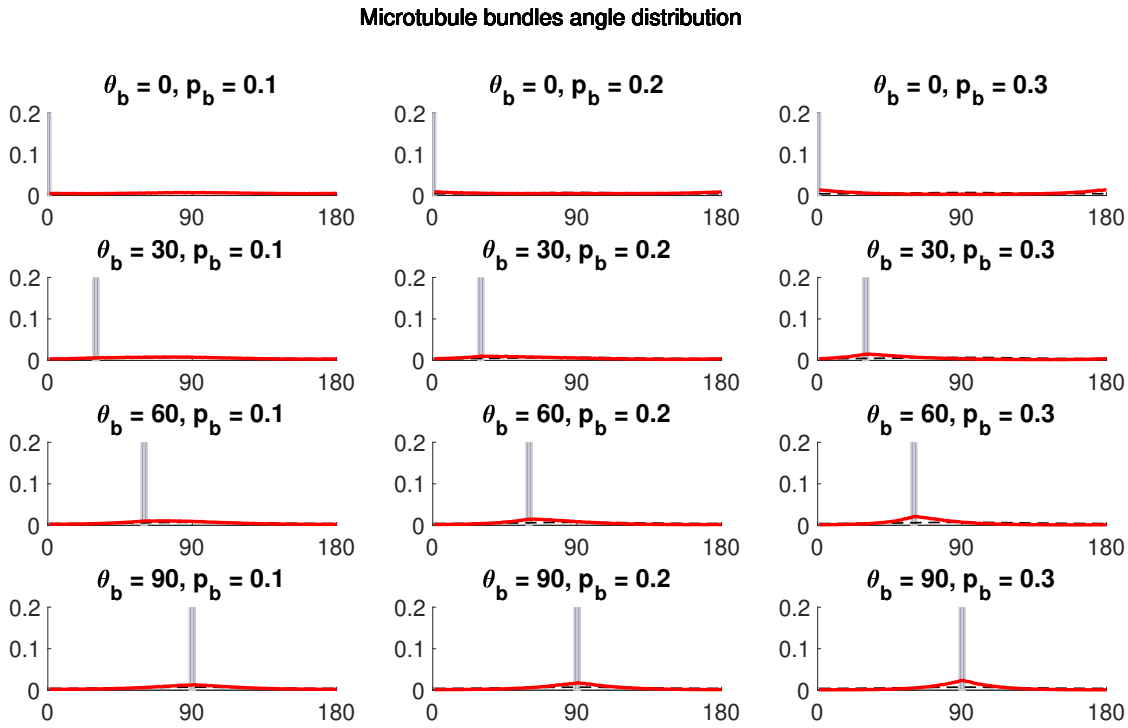

Figure 3.34: The microtubule bundles angle distribution (3.4) (red line) for the case of anisotropic discrete barriers in cells with $ecc = 0.7, \delta = 20$. The corresponding control microtubule angle distribution (dashed black lines) of the isotropic homogeneous barriers with default parameters. Vertical grey lines demonstrate the angles of anisotropy. Parameters not specified in the figure remain at their default value (see Table 3.1).

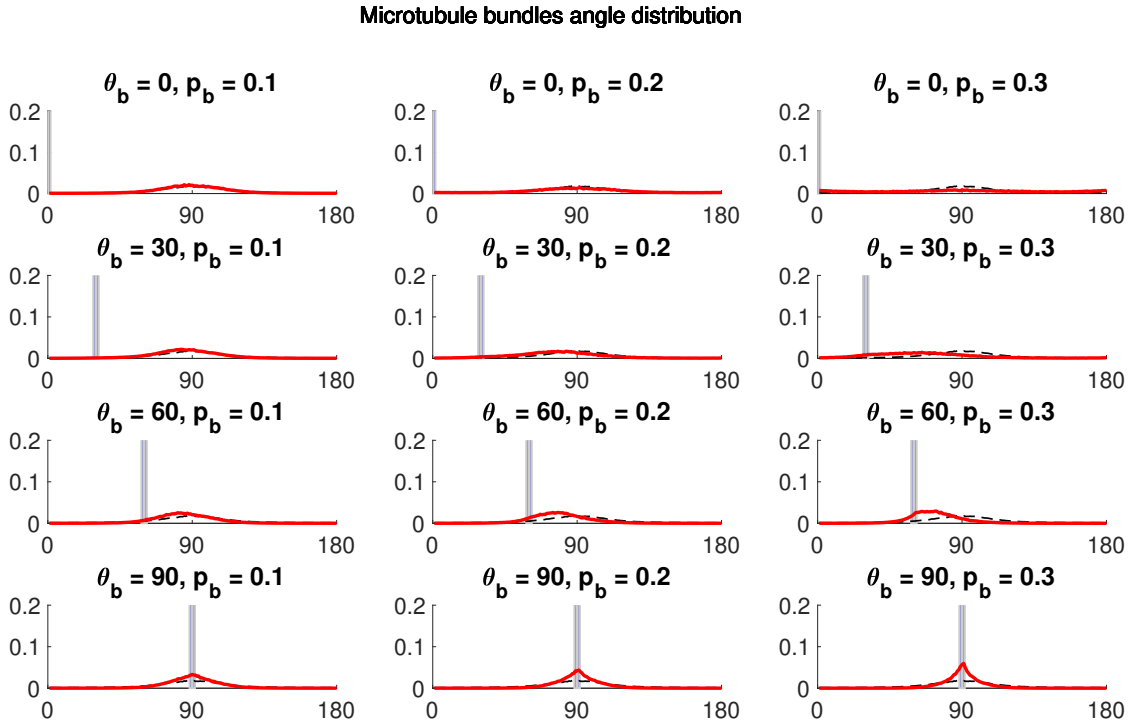

Figure 3.35: The microtubule bundles angle distribution (3.4) (red line) for the case of anisotropic discrete barriers in cells with $ecc = 0.98\,, \delta = 20$. The corresponding control microtubule angle distribution (dashed black lines) of the isotropic homogeneous barriers with default parameters. Vertical grey lines demonstrate the angles of anisotropy. Parameters not specified in the figure remain at their default value (see Table 3.1).

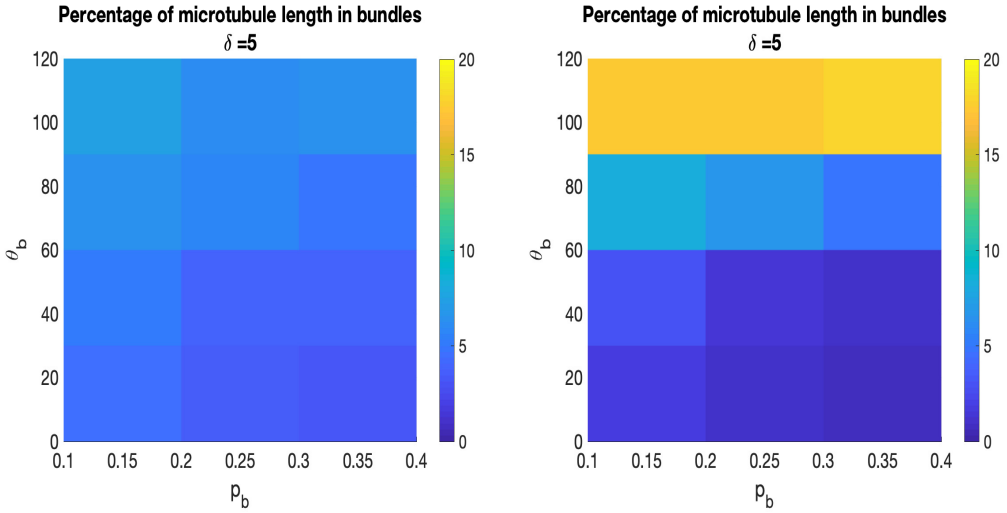

Figure 3.36: The bundling factor for the case of isotropic discrete barriers in cells with $ecc = 0.7(left), 0.98(right)$ and $\delta = 5$ computed using (3.4). Parameters not specified in the figure remain at their default value (see Table 3.1).

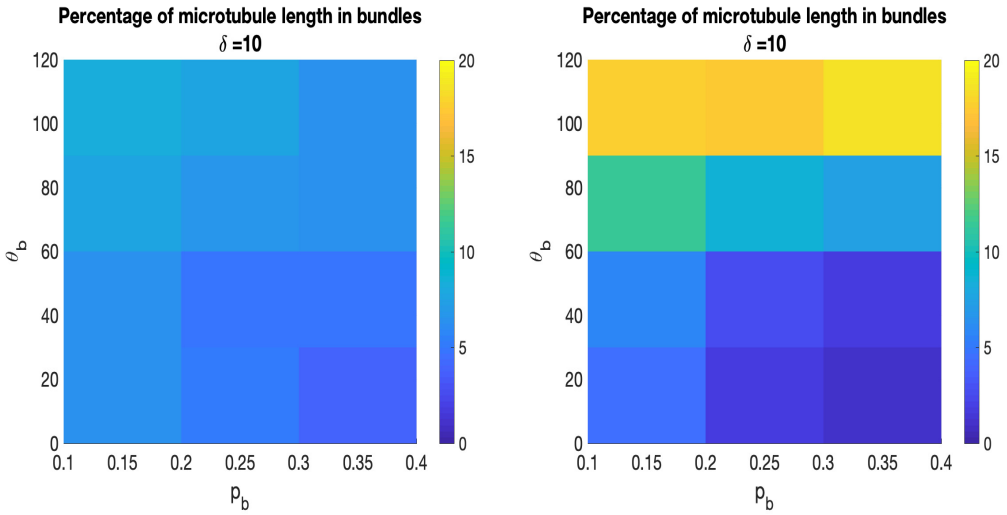

Figure 3.37: The bundling factor for the case of isotropic discrete barriers in cells with $ecc = 0.7(left), 0.98(right)$ and $\delta = 10$ computed using (3.4). Parameters not specified in the figure remain at their default value (see Table 3.1).

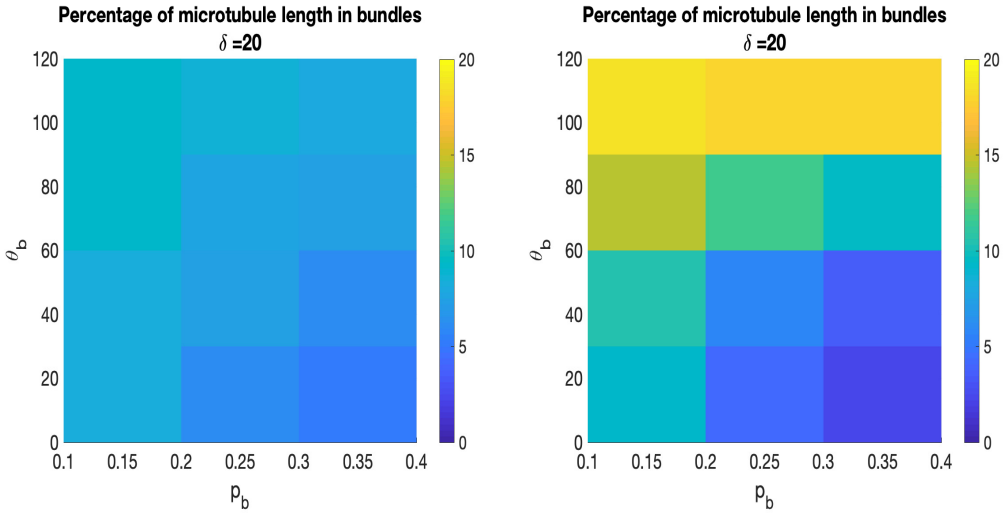

Figure 3.38: The bundling factor for the case of isotropic discrete barriers in cells with $ecc = 0.7(left), 0.98(right)$ and $\delta = 20$ computed using (3.4). Parameters not specified in the figure remain at their default value (see Table 3.1).

better relate the model to the experimental data we could move to the next hierarchy of modelling our system by introducing three dimensions as discussed in Section 5.

3.5.2 Anisotropy aligns

In this study we explored the effects of isotropic and anisotropic barriers on the microtubule self-organisation. We found that isotropic barriers do not affect the microtubule angle distribution and the mean direction of microtubules persists, primarily governed by geometry [58]. Furthermore, in Chapter 2 we have shown that self-organisation is robust on the tissue scale. However, including anisotropic barriers in the cell can have a large effect on microtubule self-organisation. Placing anisotropic barriers at a given angle proceeds in three distinct stages. First, with a very low barrier strength there is no change to the microtubule angle distribution. Next, we enter a transition period where the mean microtubule direction shifts from the major cell axis (i.e. 90^o for the aforementioned ellipses) to the angle of the anisotropic barrier. We note that the cell geometry determines the size of the transition period in the strength of the barrier parameter range: barriers are struggling to overcome the influence of cell geometry in highly elongated cells compared to almost circular ones. Finally, at the third stage we obtain that the mean direction of the microtubule angle distribution is given by the angle of the anisotropic barriers and

the standard deviation of the distribution decreases with increasing barrier strength, as the microtubules become more and more aligned.

3.5.3 Homogeneous vs. discrete

We studied homogeneous barriers since they form analytically tractable cases for analysis. However, in real life, barriers such as an actin mesh, actin cables or mitochondria, resemble discrete barriers. We saw that the results from the discrete and homogeneous studies illustrated the same trends. Increasing the probability of collapse in isotropic homogeneous barriers is analogous to increasing the number of barriers, or the barrier strength in case of the isotropic discrete barriers. Moreover, as we consider a smaller spacing between discrete anisotropic barriers we approach the limiting case of anisotropic homogeneous barriers (although we have not formally investigated the correspondence between approaches in this limiting scenario). The analytical models enabled us to understand the behaviour of the system without running a large stochastic parameter study. As microscopy improves in the future, it would be interesting to measure the angle of anisotropic cables in a cell along with the spacing between cables. Then, stochastic simulations could be used to suggest the values of biological parameters that we cannot directly measure *in vivo* like p_{cat} or p_b .

3.5.4 Barriers decrease bundling

Including barriers in our cells always decreases microtubule bundling. With isotropic barriers, increasing the strength and number of barriers decreases microtubules bundles. For anisotropic barriers, increasing the strength and number of barriers (through decreasing the spacing between them) also decreases microtubule bundles. The result of geometry driving microtubule self-organisation can also be seen in the bundling studies. We see a significant decrease in bundling when we place anisotropic barriers perpendicular to the major cell axis; here many of the long microtubule bundles are blocked. We hypothesize that the reduction of bundling would directly reduce organelle transport.

3.5.5 Role of actin cables in *Drosophila* follicular epithelium

The *Drosophila* follicular epithelium cells are from the fly's egg chamber. The egg chamber, unlike other *Drosophila* tissue, rotates through membrane proteins and the actin cytoskeleton coordinating to enable the rotation [146]. However, the otherwise robust microtubule angle distribution is altered in the egg chamber tissue during late stages of development ($ecc = 0.9 - 0.98$). From our studies we suggest that actin cables, which enable egg chamber rotation, act as barriers to microtubule cytoskeleton self-organisation. In particular, during early stages of development, the cells are not too elongated ($ecc = 0.7 - 0.8$) and the actin barriers lie at $\approx 25^o$ with respect to the minor axis of the cell. In late-stages of development, the cells are considerably elongated ($ecc = 0.9 - 0.9$), and the actin cables lie close to perpendicular to the major axis of the cell ($\approx 7^o$). From our results we saw that for discrete barriers decreasing the angle of anisotropy shifted the mean of the microtubule angle distribution away from the major cell axis and this is seen in the experimental results. Our results further suggest that the barriers are not strong and bundling only decreases with larger cell eccentricities. We predict that less E-cadherin will be transported along the microtubules to the short edges of the cell during later stages of development which could result in lower boundary adhesion, thereby permitting cell motility and egg chamber rotation.

Chapter 4

Animal navigation

4.1 Introduction

Despite their lack of technical tools, many animals show an ability to navigate large distances through complex and evolving environments, year after year, generation after generation. Successful navigation is often critical for survival, such as the need to find feeding grounds in bare environments or mating/breeding grounds. Whether we consider the swarming of honey bees (*Apis cerana*) as they set up a new hive a few kilometres away [158] or the extraordinary $60,000-80,000$ km migrations performed by Arctic terns (*Sterna paradisaea*) [42], there is no denying the remarkable diversity of navigations across the animal kingdom.

This diversity stems from the distinct environments, different sensory abilities and variability of navigating cues at an animals disposal. Navigating cues include: olfactory/chemical based cues, visual aids (such as land marks), the sun and stars, ultraviolet, infrared and polarized light, the magnetic field, thermoreception, auditory cues, inter-species communication, wind and ocean currents [62]. Given this variety, and the fact that many may be mysterious or unknown to us, it is crucial in studies that we do not make assumptions on the nature of animal navigation according to our own sensory capabilities.

Orientation can be split into "vector navigation" and "taxis-based orientation" [62]. In vector navigation, the journey is built from segments of different directions. An example of this is the visual aids that mice use to orient themselves in their environment [133]. Another example can be found in red-eye vireos who, like many other birds, migrate South for the winter from Canada to South America [62]. Taxis-

based orientation supposes that a target location lies directly in the direction towards or away from some cue, such as a chemical plume emanating from a point. We focus here on taxis-based orientation, and in particular on "true" navigation [62] where we assume that animals travel to some target location without the use of familiar land marks. Further, we consider animals which make their migratory journeys alone, therefore excluding group navigators like honey bees, which rely on communication between individuals in the migrating group [62], or schools of fish which align their movement and swim together for hydrodynamic advantages or avoiding predation.

While many studies into animal navigation have been made, fundamental questions remain. In particular, animals may use "multi-modal navigation" (several different navigating cues) to aid their nesting and foraging journeys, but the importance of individual cues within these searching strategies are unknown. Moreover, the actual sensitivity to specific cues is often unknown or very difficult to determine experimentally. In some cases natural selection removes genetic navigation traits from a species due to unsuccesful migration, such as seen in cliff swallows where early migrators where killed off from the 1996 population [62].

The threat of exctinction covers 13% of birds, 25% of mammals and 41% of amphibians (see [78]) making the understanding of animal navigation of crucial importance. Modelling animal population movement opens the possibility of future studies under evolving environmental conditions, such as changes in temperature, ocean currents, visual and noise pollution and magnetic information. Many conservation strategies have already been attempted, such as the release of turtle hatchlings in new areas to establish further breeding sites [127] or relocating Bermuda petrel (*Pterodroma cahow*) to new uninhabited locations where a population can grow [26]. Furthermore, since many animals navigate using cues that are either undetectable or barely utilised by humans, exploring homing strategies could also help enrich the field of artificial intelligence. Recently, researchers from DeepMind utilised functions of grid cells [1] to develop "a deep reinforcement learning agent with mammal-like navigational abilities" [12]. The performance of these agents was better than an "expert human and comparison agents" [12]. Understanding the fundamental properties of animal navigation could therefore lead to further improvements in the growing field of artificial intelligence.

[1] Grid cells fire in the entorhinal cortex in the brain to create a hexagonal tiling of a 2D surface in order to aid spatial representation [133].

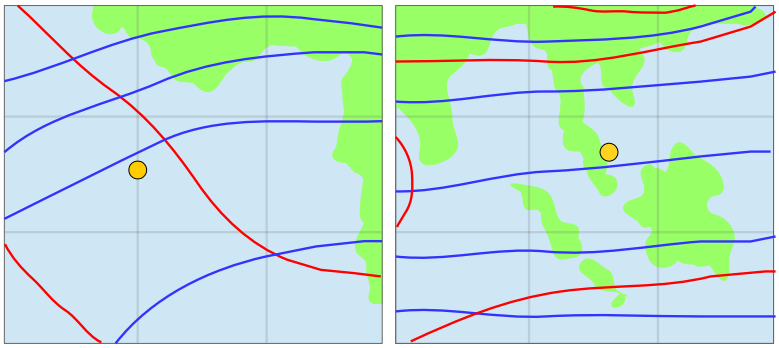

Figure 4.1: Schematic covering 45^o in latitude and longitude surrounding Ascension Island (orange dot on left hand figure, located at 8^o S, 14^o W) and Koh Tao, Thailand (orange dot on right hand figure, located at 10^o N, 100^o E). Red lines show magnetic intensity contours, differing by 5000nT, and blue lines show magnetic inclination contours, differing by 20^o. The values used in this schematic are obtained using the Magnetic Field Estimator, see [115] and [114].

4.1.1 Choosing navigating cues

Of the different cues included within taxis-based orientation, we will consider what we define as *line-based* and *point-based* cues. Specifically, we assume animals navigate towards either a line/curve source or single point source. These two forms effectively correspond to uni-coordinate or bi-coordinate navigating systems respectively.

We further classify our cues as *increasing* or *decreasing* in strength. An increasing cue is one where the cue strength increases with distance from the line/point source. A decreasing cue is correspondingly one where the cue strength decreases with distance from the line/point source.

Line-based cue

We define a line-based cue as a cue that orients an individual towards some smooth curve. Examples of a line-based cue could be responding to a single element of the geomagnetic field, such as detecting and responding to just the magnetic field total intensity or just the magnetic inclination. A specific value of magnetic intensity or inclination (or indeed any of the other elements of the field) will form a specific contour line/curve that runs across the earth's surface. Geomagnetic information has been found to be utilised by many species for migration purposes, including birds [157], [88], sea turtles [100], [71], red spotted newts (*Notophthalmus Viridescens*) [123], spiny lobsters (*Panulirus argus*) [62], [18] and even bacteria (*Spirochaeta plicatilis*)

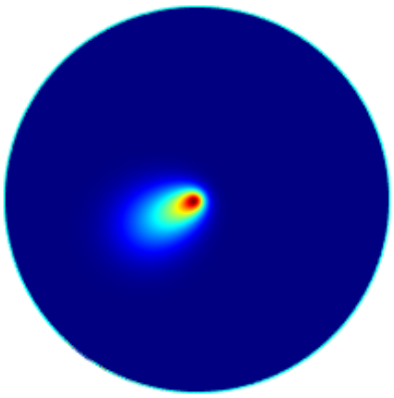

Figure 4.2: COMSOL simulation of a chemical plume, modelled via a PDE describing 2D symmetric diffusion, linear decay, a continuous point source and transport due to passive flow $\mathbf{u} = (u_x, u_y)$. The chemical plume is described by $C(x,y) = \frac{1}{4\pi}\int_0^\infty \frac{1}{t}\exp\left(\frac{-((x-u_x t)^2+(y-u_y t)^2)}{4t} - 0.1t\right)dt$ with $u_x = -1\,, u_y = -0.5\,$. Advection occurs from north-east to south-west, thus the plume is shifted bottom left from the origin.

[17]. While turtles return by following previously travelled tracks to the nesting ground, juvenile Chinook salmon (*Oncorhynchus tshawytscha*) appear to inherit their magnetic guidance information without prior migration [128]. Various experiments have displaced animals from their target sites and observed re-orientation according to the geomagnetic cues of the location [18], [123]. Since (over moderate distances) the difference between magnetic intensity (or inclination) grows as you move away further from a line of equal intensity (inclination), responding to a magnetic element would represent an example of an increasing cue, where a greater distance from the current location to the source line would yield a larger difference and presumably becomes easier to detect. Typical line-based navigating cues are shown in Figure 4.1.

Point-based cue

We define a point-based cue as a cue that orients an individual towards a single point. Examples of a point based cue include orienting according to a visual landmark (e.g. a hilltop), orienting in the direction of some specific sound source or orienting by moving up a chemical gradient (e.g. following a chemical plume to its source). Typically, the strength of these cues will decrease with distance from the source: visual/auditory due to limits of sensory perception and chemical due to diffusion and degradation of the cue. For example, given an island in the middle

of the ocean that produces soil particles, pollen, odourants *etc* into the surrounding ocean, diffusion and subsequent degradation would create a gradient of concentration that could potentially provide a target direction for animals. Yet the diminishing concentration with distance would likely yield a reduction in the sensitivity of the response. Specific examples of chemical following include moths, such as the pink bollworm (*Pectinophora gossypiella*) and summerfruit tortrix (*Adoxophyes orana*), which follow female pheromone odor plumes [46], [90]. At a larger scale, homing pigeons exposed to various odourants such as benzaldehyde, olive oil and synthetic turpentine were found to subsequently fly towards the corresponding scent locations after being transported away from the source [79], [120]. Figure 4.2 shows an example of a point source cue transported away from its source and undergoing some decay.

Cue combinations of two different line-based cues could effectively generate a point-based cue. As previously remarked, magnetic field intensity and inclination lines vary strongly across the world and Figure 4.1 illustrates this for two popular breeding grounds of green sea turtles. Here we can see that Ascension Island (left part of Figure 4.1) provides an "ideal" geomagnetic field map, where the measure of inclination is roughly perpendicular to the measure of intensity. Subsequently, an individual that detects both cues could potentially integrate this information and acquire bi-coordinate navigation: the two line-based cues could be put together to generate a point source. Koh Tao, on the other hand, has a geomagnetic field where inclination and intensity (right part of Figure 4.1) lines lie roughly parallel, making this integration to generate point-source information more challenging.

4.1.2 Motivation: a study of turtle navigation

In [119] we studied island homing of green sea turtles using both agent-based and continuous modelling approaches. Here we introduce the background to the migration of these turtles, and summarise the results from [119] that motivate the preliminary research here.

The remarkable journeys concern those taken by green sea turtles (*Chelonia mydas*) in order to reach their nesting ground at tiny Ascension Island, located over 2200km away from their feeding grounds along the coasts of eastern South America. Several cues have been proposed to explain this journey, including celestial, chemical, geomagnetic, visual and wave propagation patterns. Initial work during the

1960's suggested that turtles employed celestial navigation, using stars as a visual aid from the ocean surface. However, this theory was refuted by Koch in 1969, who determined that turtles are incapable of using celestial cues and suggested instead that they follow chemical plumes to their target [27]. Koch used modelling to suggest that chemical substances released from the island could remain unmixed with the surrounding water and carried intact over vast distances [27]. Moreover, he concluded that other forms of navigational cue may also be required to overcome the large distances travelled [27].

The analysis of six tracked female turtles travelling *from* Ascension Island showed that turtles maintain course over long distances and correct their path along the way [68]. It should be noted, however, that the return journey of these turtles to South America involves a vastly larger target and hence would be considerably simpler. Lohmann also used satellite tracking to show that migrating turtles swim directly towards their distant goals, even when faced with perpendicular currents [71], while models investigated by Scott showed that even small amounts of directional movement can generate big changes to the trajectories of the turtles [69].

In terms of navigational cues, recent theories have been proposed in which turtles use geo-magnetic cues [101], [100], chemical-based cues [3] or a combination in which magnetic cues are used at larger distances, followed by chemical cues when the target is near [71], [68] and [44]. However, we remark that research has also been done which seems to contradict certain hypotheses on magnetic cues, [4], [3]. For example, in one experiment displaced female sea turtles were tracked during their breeding period, with their return paths to Ascension Island compared against gradients of various magnetic field components [3] while in the other experiment the magnetic field surrounding a turtle was disrupted via magnets. Negligible difference was found in the migratory paths [4].

Using both agent based (see Figure 4.3) and continuous modelling we previously modelled how multimodal navigation impact on turtle homing [119]. We introduced navigating cues which represent the magnetic field strength intensity, the magnetic inclination angle, a chemical plume transported by the ocean currents and a chemical plume transported by the wind. Each of the intensity and inclination cues represented an example of line-based navigation, with the turtle respectively navigating towards the contours of intensity and inclination that intersect with the island. Each of the chemical cues potentially provided point-based information, as the turtles navigated up the plume to the source. We found that increasing the number of cues utilised

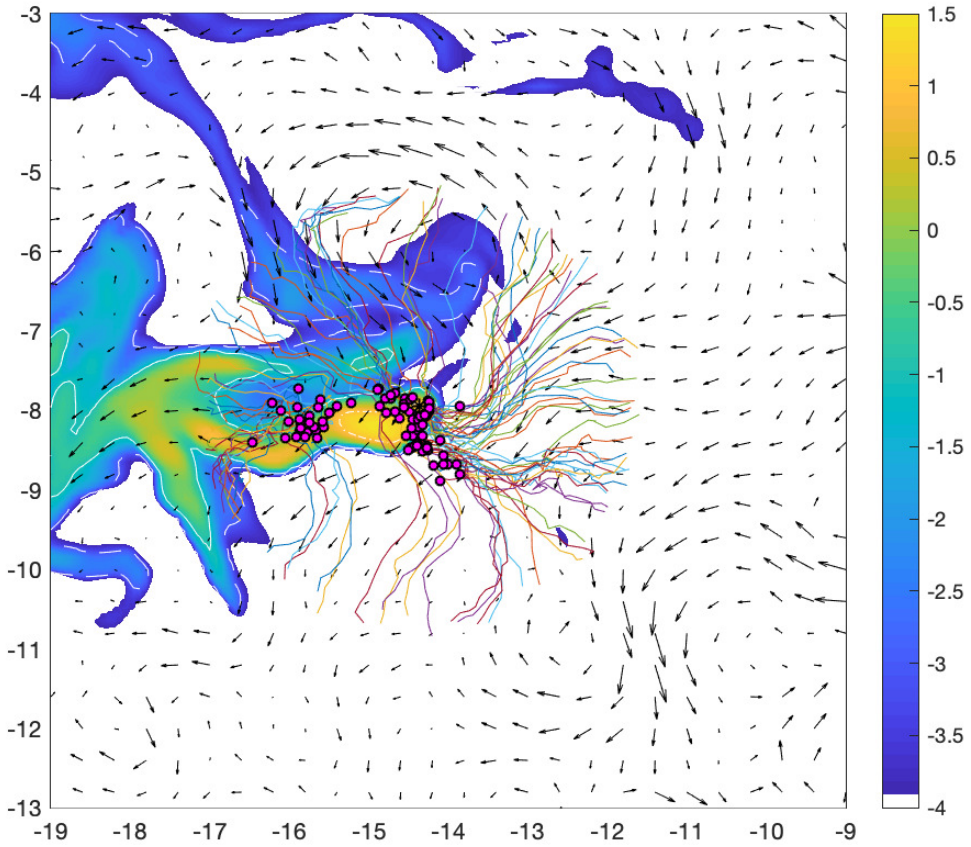

Figure 4.3: Example trajectories (colourful lines) of an IBM for turtles (pink dots) released around Ascension Island (located at the centre of the field) and attempting to navigate back to this location. The numerical simulations are performed in Matlab [108]. The ocean flow strength is represented by the black arrows while the colour density map illustrates the distribution of a presumed chemical/odour that is produced at the island and spreads via ocean transport. See [119] for further details.

by the turtles improved their homing abilities, even in extreme cases where the total amount of navigation strength dropped. In other words, we found that turtles navigating with several fewer weak cues would outperform those utilising one strong cue. We show in Figure 4.4 the homing efficiency of turtles (the fraction of turtles

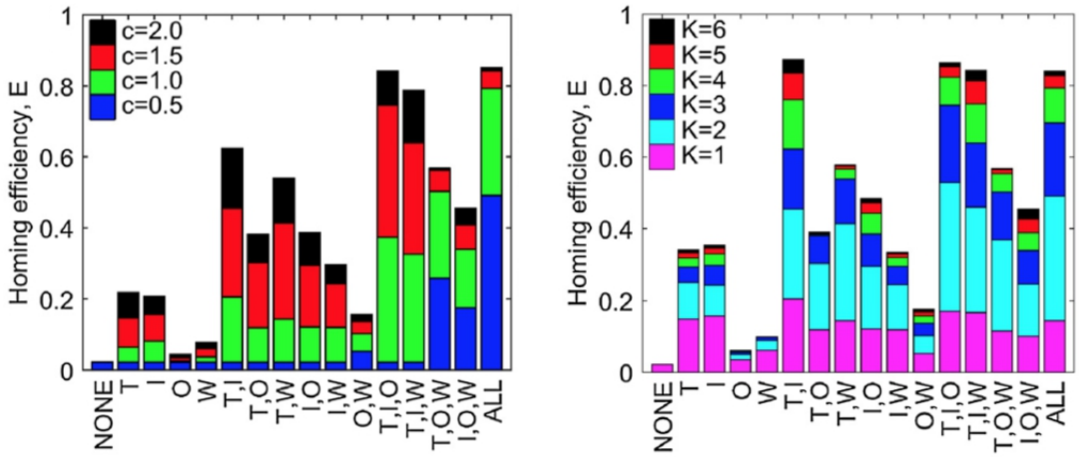

Figure 4.4: Homing efficiency of green sea turtles under additive (left) and redistributive (right) normalisation of navigating cues where navigating cues are T: magnetic field total intensity, I: inclination of magnetic field, O: ocean plume cue and W: wind borne cue. See [119] for full details of the study.

which returns to a vicinity of the island in the allocated time) under two types of normalisation procedure (termed "additive" and "redistributive"). Full details of the agent based simulations are included in Section A.2.

4.1.3 Outline

In this work we consider a generalised study of animal navigation. We consider taxis-based line and point source cues as the guiding navigation. Motivated by the results from [119] we create an abstract study which focuses on the various generalised forms of cue, and examine their potential to allow efficient homing of a population (i.e. navigation back to a specific location) either on their own or in combination.

4.2 Methods

Two approaches in building a model are a "bottom up" approach, such as an individual based model (IBM), and a "top down" approach, such as postulating a continuous equation that describes the some population distribution. IBM models are computa-

tionally expensive due to the need to compute each individual in a large population, but can be compared well against empirical data. However, due to the limited availability of large data sets, weaker patterns may be missed when it comes to direct comparison. On the other hand, continuous models show statistical regularities while missing out on the possible intricacies of individuals. We focus on the use of scaling to establish a link between an IBM and its corresponding macroscopic PDE model, investigating at this stage only the continuous model further. The derivation of the model for describing animal navigation is based on the transport equation approach outlined in [73] and [74].

4.2.1 Individual Based Model

We start with a velocity-jump description [117] for the individual based model (IBM), which assumes migratory animal i is at position $\mathbf{x}_i(t)$ and moves with velocity $\mathbf{v}_i(t)$. The flow of the medium (passive movement) is given by $\mathbf{u}(t, \mathbf{x}) \in \mathbb{R}^n$. The active velocity $\mathbf{v}_i \in \mathbb{R}^n$, which describes the movement of the individual specifically due to its self-generated movement, is assumed to remain the same until the animal makes a turn. Here, the act of turning is taken to be effectively instantaneous and its frequency distribution follows a Poisson process with parameter λ. The new active velocity is subsequently chosen from a distribution $q(\mathbf{v}|t, \mathbf{x}_i)$ and it is through this distribution that we can incorporate navigation information. We note that in the current formulation the new active velocity will only depend on the environment and not on the individual's previous active velocity. For a small time increment Δt, the evolution of the system can be summarised by the following:

$$\begin{aligned} \mathbf{x}_i(t + \Delta t) &= \mathbf{x}_i(t) + \Delta t(\mathbf{v}_i(t) + \mathbf{u}(t, \mathbf{x}_i))\,; \\ \mathbf{v}_i(t + \Delta t) &= \begin{cases} q(\mathbf{v}|t + \Delta t\,,\, \mathbf{x}_i(t + \Delta t)) & \text{with probability } \lambda \Delta t\,, \\ \mathbf{v}_i(t) \quad \text{otherwise}\,. \end{cases} \end{aligned} \tag{4.1}$$

Full details of the agent based simulations are included in Section A.2. The corresponding continuous model for the position and velocity dynamics of (4.1) is

$$\frac{d\mathbf{x_i}}{dt} = \mathbf{v}_i(t) + \mathbf{u}(t, \mathbf{x}_i)\,, \tag{4.2}$$

where $\mathbf{v}_i$ is a stochastic Markov jump process where jumps occur at a rate λ and the new velocity is chosen from the distribution $q(\mathbf{v}|t\,,\, \mathbf{x_i})$.

4.2.2 Transport Model

Our next step is to move from the discrete IBM to a continuous model by reformulation as a continuous transport equation. Specifically, we define the animal population density $p(t, \mathbf{x}, \mathbf{v})$ as the density distribution of animals at time t, position $\mathbf{x} \in \mathbb{R}^n$ with active velocity $\mathbf{v} \in \mathbb{R}^n$. Here $\mathbf{x}$ and $\mathbf{v}$ are now describing the population density instead of individuals i so we do not require the index notation. So $\mathbf{v}$ is the average velocity corresponding to $\mathbf{v} := \frac{1}{N}\sum_{i=1}^{N} \mathbf{v}_i$ where N is the number of individuals in the agent based model. Note that we implicitly assume that the interactions of individuals are negligible, an assumption that applies well to the turtle navigation problem (solitary migratory animals unaffected by group dynamics), as animals are widely dispersed in their environment and contacts are rare. It does not necessarily apply to other instances of naigation, where populations travel in groups. Our continuous transport model is given by

$$p_t(t, \mathbf{x}, \mathbf{v}) + \nabla \cdot \mathbf{v}p(t, \mathbf{x}, \mathbf{v}) + \nabla \cdot \mathbf{u}p(t, \mathbf{x}, \mathbf{v}) = \lambda(m(t, \mathbf{x})q(\mathbf{v}|t, \mathbf{x}) - p(t, \mathbf{x}, \mathbf{v}))\,, \quad (4.3)$$

where $m(t, \mathbf{x}) = \int_V p(t, \mathbf{x}, \mathbf{v})d\mathbf{v}$ is the macroscopic or "observable" population of animals. Note that the turning distribution q and the passive flow $\mathbf{u}$ remain the same in the individual based (4.1) and the transport model (4.3).

4.2.3 Macroscopic description

Following the steps in [74] we can state that the macroscopic population density of animals, $m(t, \mathbf{x})$, is approximated by the solution of

$$\begin{aligned} \frac{\partial m(t,\mathbf{x})}{\partial t} \quad &+ \quad \nabla \cdot ((\underbrace{\mathbf{a}(t,\mathbf{x})}_{\text{active velocity}} + \underbrace{\mathbf{u}(t,\mathbf{x})}_{\text{passive velocity}})m(t,\mathbf{x})) \\ &= \quad \nabla\nabla(\underbrace{\mathbb{D}(t,\mathbf{x})}_{\text{anisotropic diffusion}} m(t,\mathbf{x}))\,, \end{aligned} \quad (4.4)$$

with

$$\nabla\nabla(\mathbb{D}(t, \mathbf{x})m(t, \mathbf{x})) = \sum_{i,j=1}^{n} \frac{\partial}{\partial x_i}\frac{\partial}{\partial x_j}(\mathbb{D}^{ij}(t, \mathbf{x})m(t, \mathbf{x}))$$

for all $t \geq 0$. In the above,

$$\mathbf{a}(t, \mathbf{x}) = \int_V \mathbf{v}q(t, \mathbf{x}, \mathbf{v})d\mathbf{v}\,, \quad (4.5)$$

defines active advection (i.e. the movement due to an individual's self generated movement) and

$$\mathbb{D}(t,\mathbf{x}) = \frac{1}{\lambda}\mathbb{V} = \frac{1}{\lambda}\int_V (\mathbf{v} - a(t,\mathbf{x}))(\mathbf{v} - a(t,\mathbf{x}))^T q(t,\mathbf{x},\mathbf{v})d\mathbf{v} \tag{4.6}$$

defines the anisotropic diffusion. We should note here that $\mathbf{a}(t,\mathbf{x})$ is the expectation of $q(\mathbf{v}|t,\mathbf{x})$ and $\mathbb{D}(t,\mathbf{x})$ is proportional to the variance-covariance matrix of $q(\mathbf{v}|t,\mathbf{x})$. Thus, the PDE relates directly to statistical properties of the the turning distribution $q(\mathbf{v}|t,\mathbf{x})$ of the IBM. Further, we will consider $n = 2$, therefore simplifying our model such that animals navigate over 2D space. Again, in the specific context of turtle navigation, this is reasonable since turtles mainly swim within the few metres of the surface. We further assume that the animal active speed is constant and equal to s, such that only the direction changes at each turn. In this way we set $\mathbf{v} = s\mathbf{n}$, where $\mathbf{n} = \mathbf{v}/|\mathbf{v}|$ is the unit vector describing the direction. Through stating

$$q(\mathbf{v}|t,\mathbf{x}) := \tilde{q}(\mathbf{n}|t,\mathbf{x})/s^{n-1}, \tag{4.7}$$

with active direction $\mathbf{n} = \mathbf{v}/|\mathbf{v}| \in \mathbb{S}^{n-1}$ on the unit sphere $\mathbb{S}^{n-1}$ we define $\tilde{q}(\mathbf{n}|t,\mathbf{x})$ as the distribution of turning over all possible directions.

Choices for $\tilde{q}(\mathbf{n}|t,\mathbf{x})$

We use polar coordinates, setting $\mathbf{v} = s\mathbf{n} = s(\cos\alpha, \sin\alpha)$ with $\alpha \in [0, 2\pi)$ being the corresponding angle of the turning direction. With coordinates $\mathbf{w} = (\cos A, \sin A)$, where $A(t,\mathbf{x})$ is the dominant angle of orientation and $k(t,\mathbf{x})$ is the navigational strength[2], our circular turning distribution will be described by the Von Mises distribution [105]

$$\hat{q}(\alpha|k,A) = \frac{1}{2\pi I_0(k)} e^{k\cos(\alpha - A)}, \tag{4.8}$$

where $I_0(k)$ denotes the modified Bessel function of first kind and order 0. Under this choice of $\hat{q}$, we can directly compute a and $\mathbb{D}$ in (4.5) and (4.6) (see [72] for the derivation) as

$$\mathbf{a}(k,A) = s\frac{I_1(k)}{I_0(k)}(\cos A, \sin A), \tag{4.9}$$

[2]Increasing k corresponds to the species having a stronger navigating capacity to travel towards the target while setting k to zero means there is no navigating capacity and an active direction of movement is chosen randomly from a uniform distribution.

and

$$\begin{aligned}\mathbb{D}(k,A) &= \frac{s^2}{2\mu}\left(1-\frac{I_2(k)}{I_0(k)}\right)\begin{pmatrix}1 & 0\\ 0 & 1\end{pmatrix} \\ &+ \frac{s^2}{\mu}\left(\frac{I_2(k)}{I_0(k)}-\frac{I_1(k)^2}{I_0(k)^2}\right)\begin{pmatrix}\cos^2 A & \cos A\sin A\\ \cos A\sin A & \sin^2 A\end{pmatrix}.\end{aligned} \tag{4.10}$$

We now define three functions of k that relate to the navigation strength of the animals as

$$c_1(k) = s\frac{I_1(k)}{I_0(k)}, \tag{4.11}$$

$$c_2(k) = \frac{s^2}{2\mu}\left(1-\frac{I_2(k)}{I_0(k)}\right), \tag{4.12}$$

$$c_3(k) = \frac{s^2}{\mu}\left(\frac{I_2(k)}{I_0(k)}-\frac{I_1(k)^2}{I_0(k)^2}\right), \tag{4.13}$$

where $I_0(k), I_1(k), I_2(k)$ denotes the modified Bessel function of first kind and order $0, 1, 2$ respectively. The modified Bessel function of first kind and order α is defined as

$$I_\alpha(k) = \sum_{m=0}^{\infty}\frac{1}{m!\Gamma(m+\alpha+1)}\left(\frac{k}{2}\right)^{2m+\alpha},$$

where $\Gamma(n) = (n-1)!$.

From Figure 4.5 we note that $|c_1(k)| > |c_3(k)|$ and $c_3(k) < 0\,, \forall k \in (0, 10)$ an important fact for stability analysis later. Building on the nature of directional bias in the Von Mises distribution with regards to k discussed earlier, our model implies that at $k = 0$ the animals will be dominated by the passive flow, as they have no navigational capacity and move randomly. In this case the active advective component becomes zero and we are left with isotropic diffusion and an advection due to the passive flow in the environment. Moreover, when $k \to \infty$ the strength of the active advection saturates to their active swimming speed. In this case, the diffusion terms disappear and it is solely the combination of passive and active advection that pulls animals towards the target. We note that $c_1(k)$ is therefore the critical function that determines the critical speeds required for animals to move in the direction of their target. The animal is expected to successfully navigate to their goal if active advection can overcome the passive flow.

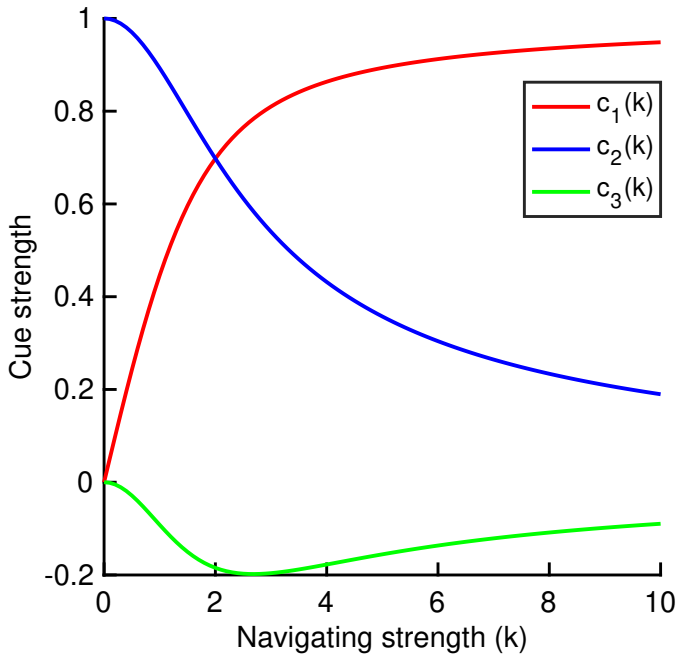

Figure 4.5: Functions (4.11), red, (4.12), blue, (4.13), green, of the varying animal navigating strength parameter k.

4.2.4 Characteristics

To investigate the long term dynamics of the system, we study the characteristics of (4.4) by noting it can be re-written as

$$\frac{\partial m(t,\mathbf{x})}{\partial t}+\nabla\cdot((\mathbf{a}(t,\mathbf{x})+\mathbf{u}(t,\mathbf{x}))m(t,\mathbf{x}))=\nabla\cdot(\mathbb{D}(t,\mathbf{x})\nabla m(t,\mathbf{x}))+\nabla\cdot((\nabla\cdot\mathbb{D}(t,\mathbf{x}))m(t,\mathbf{x}))\,.$$

When we run simulations for this PDE model we use no-loss reflective boundary conditions at the edge of the computational domain (i.e. animals are reflected back into the domain when they reach the edges). The initial conditions mimic either the situation of a localized release or a uniform animal density distribution throughout the domain as described in [74, 119]. Since we do not compute any result from this PDE here we omit further details as the characteristics do not require boundary conditions. This can be re-arranged to a classic form advection-diffusion model, specifically

$$\frac{\partial m(t,\mathbf{x})}{\partial t}+\nabla\cdot((\mathbf{a}(t,\mathbf{x})+\mathbf{u}(t,\mathbf{x})-\nabla\cdot\mathbb{D}(t,\mathbf{x}))m(t,\mathbf{x}))=\nabla\cdot(\mathbb{D}(t,\mathbf{x})\nabla m(t,\mathbf{x}))\,.$$

Hence, the advection speed gives the mean trajectory paths resulting in the following dynamical system:

$$\frac{d\mathbf{x}}{dt} = \mathbf{u}(t,\mathbf{x}) + \mathbf{a}(t,\mathbf{x}) - \nabla \cdot \mathbb{D}(t,\mathbf{x})\,. \tag{4.14}$$

The dynamical system given by (4.14) effectively represents the trajectory of a typical individual from a given position. Thus, by carrying out a stability analysis on the above dynamical system we can determine whether an animal eventually ends at a specific point in space and, if so, whether this point is sufficiently close enough to the target location to consider that it has successfully homed.

4.2.5 Modelling different types of cues

Point-based cue

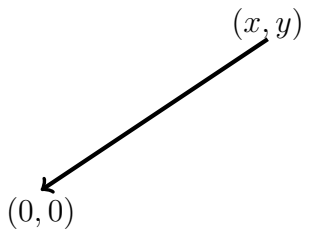

Figure 4.6: Schematic of an animal at $(x\,,y)$ intending to return to a target centred at the origin. In a point-based cue, the dominant angle of orientation will be exactly towards the origin, although the certainty of this choice will depend with distance as described in the text.

To describe a point based cue we suppose that an animal at position (x,y) has some information that actively navigates it in the direction of its target, supposed to be centred at the origin, see Figure 4.6. Since active movement direction is defined through the turning distribution $\tilde{q}$, given in (4.8), we therefore set $\mathbf{w} = \left(\frac{-x}{\sqrt{x^2+y^2}}\,,\frac{-y}{\sqrt{x^2+y^2}}\right)$. Thus we have $\cos A = \frac{-x}{\sqrt{x^2+y^2}}$ and $\sin A = \frac{-y}{\sqrt{x^2+y^2}}$ and, substituting into (4.9) and (4.10), we obtain

$$\mathbf{a}(t,\mathbf{x}) = -c_1(k)\begin{pmatrix} x/r \\ y/r \end{pmatrix}\,, \tag{4.15}$$

where $c_1(k) := s\frac{I_1(k)}{I_0(k)}$ and $r = \sqrt{x^2+y^2}$ and

$$\mathbb{D}(t,\mathbf{x}) \overset{\text{Cartesian}}{=} c_2(k)\begin{pmatrix}1 & 0\\ 0 & 1\end{pmatrix} + c_3(k)\begin{pmatrix}x^2/r^2 & xy/r^2\\ xy/r^2 & y^2/r^2\end{pmatrix}, \tag{4.16}$$

where $c_2(k) := \frac{s^2}{2\lambda}\left(1 - \frac{I_2(k)}{I_0(k)}\right)$ and $c_3(k) := \frac{s^2}{\lambda}\left(\frac{I_2(k)}{I_0(k)} - \frac{I_1(k)^2}{I_0(k)^2}\right)$ as defined previously. Considering the characteristics defined as in (4.14) and setting the passive flow $\mathbf{u} = (u_x\,, u_y)$, the dynamical system describing typical trajectories will be given by

$$\dot{x} = u_x - c_1(k)\frac{x}{\sqrt{x^2+y^2}} - c_3(k)\frac{x}{x^2+y^2}\,; \tag{4.17}$$

$$\dot{y} = u_y - c_1(k)\frac{y}{\sqrt{x^2+y^2}} - c_3(k)\frac{y}{x^2+y^2}\,. \tag{4.18}$$

Our aim is to study the steady states and phase plane of (4.17) and (4.18), to investigate how a typical animal trajectory will evolve from some starting location. In the dynamical system u_x, u_y are constants which describe the strength of the flow in the x and y direction respectively whereas the navigating cue strength k depends on both x and y.

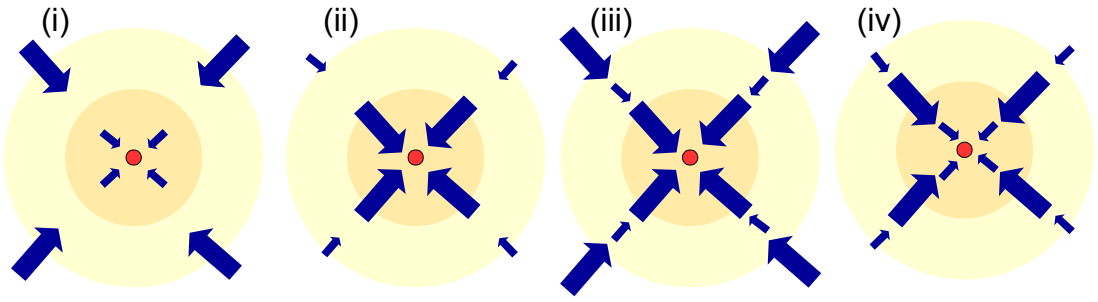

Figure 4.7: A schematic of point based navigating cues. Red circle shows the target, yellow to orange border denotes the mid zone for the navigating cues and the blue arrows demonstrate cue strength. From left to right cues are: (i) purely increasing with radial distance, (ii) purely decreasing with radial distance, (iii) combined with a trough in the mid zone and (iv) combined with a peak in the mid zone.

We will consider that the cue, or cue combinations, generates a navigational response that is either:

- purely increasing, i.e. strongest at largest distances and weaker closer to the target (Figure 4.7 (i)) ;

- purely decreasing, i.e. strongest close to the target and weaker further away (Figure 4.7 (ii));
- strongest close and far away, but weaker at intermediates distances from the target (Figure 4.7 (iii));
- strongest at intermediate distances, but weaker close or far away from the target (Figure 4.7 (iv)).

With this in mind, as generic choices we consider either the exponential form

$$k := \kappa_1(1 - e^{-\alpha_1 r}) + \kappa_2 e^{-\alpha_2 r}\,, \tag{4.19}$$

or the hyperbolic form

$$k := \frac{\kappa_3}{2}(1 + \tanh(r - \alpha_3)) + \frac{\kappa_4}{2}(1 + \tanh(-r + \alpha_4)) \tag{4.20}$$

where $r = \sqrt{x^2 + y^2}$. The parameters κ_i for $i \in \{1, 2, 3, 4\}$ determine the maximum strength of the cue, while the parameters α_i for $i \in \{1, 2, 3, 4\}$ determine the spatial range over which the cue strength changes in magnitude. The various forms illustrated in Figure 4.7 (i-iv) can be replicated through appropriate specification of these parameters. As an example, the purely increasing cue strength scenario (Figure 4.7 (i)) under the exponential form would correspond to setting $\kappa_1 > 0$ and κ_2 at zero. Similarly, the purely decreasing cue scenario (Figure 4.7 (ii)) would correspond to setting $\kappa_2 > 0$ and $\kappa_1 = 0$. Combinations of purely increasing/decreasing cues can generate either of the forms suggested by Figure 4.7 (iii) or (iv) according to appropriate parameter selection.

The distinct choice of the hyperbolic form stems from the desire to model more "switch-like" cues, where a cue effectively provides zero navigating strength above/-below some critical distance and a constant navigation below/above, where the α_i's set the spatial distance at which these switches occur.

We study both exponential and hyperbolic cues since the perceived cue strength for animals remains an open questions and theories exist whether cues either gradually or rapidly change with distance. Different cues will exert different strengths of response according to the distance from the target. For example, bi-coordinate magnetic field information may be expected to become stronger further away from the target whereas a chemical cue may be expected to become weaker, as discussed

in Section 4.1.1. A combination of the two together could give either of the cases in Figure 4.7 (iii)-(iv), according to their effective ranges.

Line-based cue

For navigation towards a line we return to the full system of characteristics (4.14) and set the navigating strength

$$k := \kappa_5(1 - e^{-\alpha_5 \tilde{d}_5}) + \kappa_6(1 - e^{-\alpha_6 \tilde{d}_6}) \,, \tag{4.21}$$

where $\tilde{d}_5 = \left| \frac{x\tan(\theta_5) - y}{\sqrt{\tan(\theta_5)^2+1}} \right|$, $\tilde{d}_6 = \left| \frac{x\tan(\theta_6) - y}{\sqrt{\tan(\theta_6)^2+1}} \right|$ and angle $A := \theta_{5,6} \pm \frac{\pi}{2}$. Here, $\theta_{5,6}$ corresponds to the angle of the navigating cue line and $\pm\frac{\pi}{2}$ allows for correct re-orientation perpendicular to $\theta_{5,6}$, i.e. if $y < \tan_{5,6} x$ then $A = \theta_{5,6} + \frac{\pi}{2}$ and otherwise $A = \theta_{5,6} - \frac{\pi}{2}$. With this form we effectively assume that an animal navigates towards one or two lines that pass through the origin with angles θ_5 or θ_6. Note that with this form we have specifically restricted to the case of purely increasing cue strengths, i.e. where the strength of navigation increases with distance from the line source. Our motivation for this lies in that line-based cues typically represent magnetic field contours, where the strength of response is likely to increase with distance from the contour as discussed earlier. We note further that migrating in response to just one single line (oriented at angle θ_5) can be achieved by setting $\kappa_6 = 0$. A schematic of the various assumed combinations of line-based cues is provided in Figure 4.8. Again, the island that animals migrate towards is located at the origin.

The equations we study for the line-based navigation become

$$\dot{x} = u_x + a(k, A) - \nabla \cdot \mathbb{D}(k, A) \tag{4.22}$$

$$\dot{y} = u_y + a(k, A) - \nabla \cdot \mathbb{D}(k, A) \tag{4.23}$$

with

$$a(k, A) := s\frac{I_1(k)}{I_0(k)}(\cos A \,, \sin A) \,,$$

and

$$\mathbb{D}(k, A) := \frac{s^2}{2\lambda}\left(1 - \frac{I_2(k)}{I_0(k)}\right)\begin{pmatrix} 1 & 0 \\ 0 & 1 \end{pmatrix} + \frac{s^2}{\lambda}\left(\frac{I_2(k)}{I_0(k)} - \frac{I_1(k)^2}{I_0(k)^2}\right)\begin{pmatrix} \cos^2 A & \cos A \sin A \\ \cos A \sin A & \sin^2 A \end{pmatrix} ,$$

with k and A as specified above. In this case we work with circular co-ordinates and

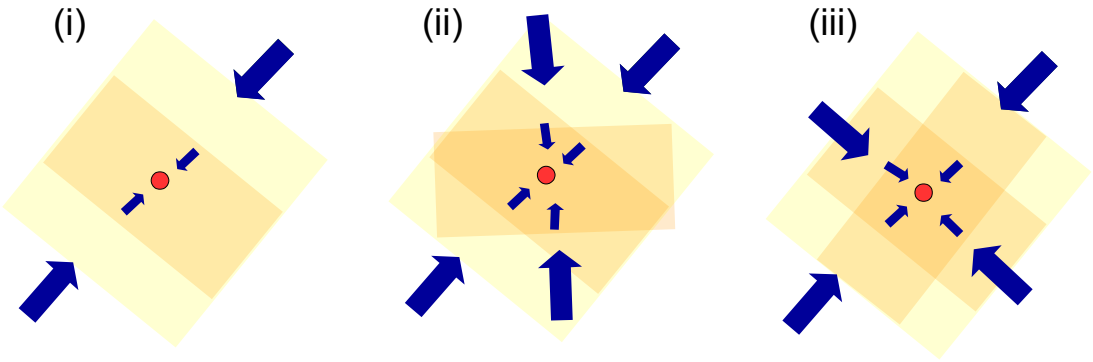

Figure 4.8: A schematic of line based navigating cues. Red circle shows the target, yellow to orange border denotes the mid zone and the blue arrows demonstrate cue strength. From left to right, cues are: (i) single line cue increasing with distance, (ii) two lines cues which increase with distance with 45^o between angles of cues, (iii) two lines cues which increase with distance with 90^o between angles of cues.

use the full system of equations without any simplifications.

4.3 Results

4.3.1 Parameters

Given the abstract nature of this initial study, for all simulations we choose an analytically convenient flow by setting $u_y = 0$ and varying u_x. This corresponds to a passive flow where flow is only in the x direction. Unless stated otherwise we set $\lambda = 1$, which can effectively be stipulated through assuming an a priori non-dimensionalisation of the time scale such that turning rate is scaled to unity. As a reference speed s we consider $s = 1$, although this parameter will be altered in some of the simulations that follow. It is worth remarking that under $s = \lambda = 1$, the length scale of 1 constitutes the individual's "run-time", i.e. the distance travelled by an individual between turning processes. We will consider the dimensions of the field to be two orders of magnitude higher this, allowing our individuals to navigate within the square region $[-50, 50] \times [-50, 50]$, where the origin marks the centre of the navigating target (later taken to be a circular region).

We vary the cue strengths $\kappa_i \in [0.5\,, 10]\,, \forall i = \{1\,, 2\,, 3\,, 4\}$, where we note that an individual navigating with a strength at the lower bound of this range would correspond to an uncertain navigator and at the upper bound a confident navigator,

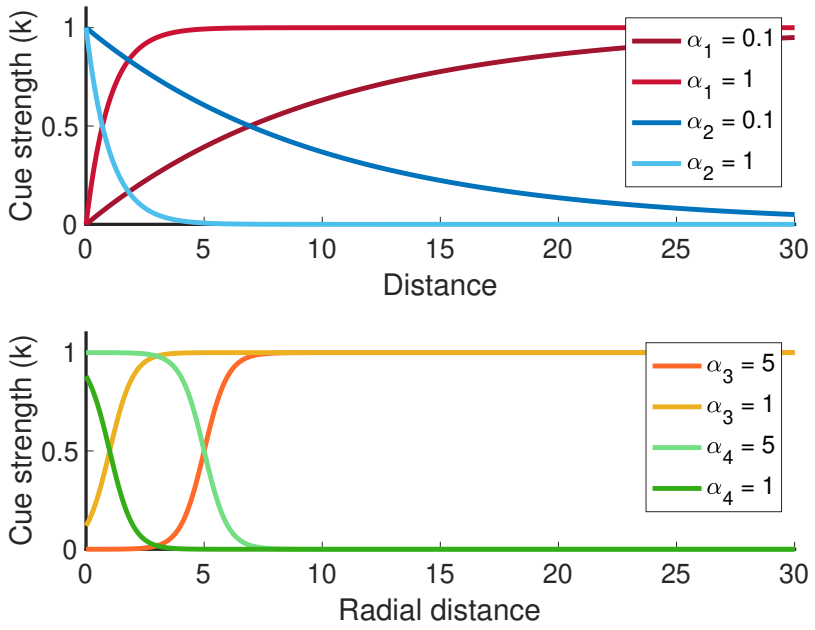

Figure 4.9: Examples of navigation cue strength with distance for exponential cues, $k := \kappa_1(1-e^{-\alpha_1 r})+\kappa_2 e^{-\alpha_2 r}$, and hyperbolic cues, $k := \frac{\kappa_3}{2}(1+\tanh(r-\alpha_3))+\frac{\kappa_4}{2}(1+\tanh(-r+\alpha_4))$. Note that $k := \kappa_1(1-e^{-\alpha_1 r})$ also applies to the strength of the line-based cues in our study.

i.e. one that will typically choose the correct direction within a few degrees or so. For the range parameters we either vary α between 0.5 and 5 for the exponential case or between 0.5 and 25 for the hyperbolic case. Example cue strengths are plotted in Figure 4.9.

To understand whether individuals are able to efficiently home, we study the dynamical equations generated through the study of the characteristics. Specifically, we will either study the properties of the phase plane to evaluate typical trajectories (aided through the use of the bifurcation software XPP-Auto) or use a standard stiff-systems ODE solver (the MATLAB routine "ode15s" [108]) to directly compute trajectories from different starting locations.

4.3.2 Measurements

We use two principal measurements to characterise the homing/navigation process of the population, i.e. the ability of the navigator to reach the target located at the origin:

- the distance of the stable steady state (if it exists) in the phase plane to the target location;
- the homing value.

The distance of the stable steady state to the origin is somewhat imperfect as a measure, but its advantage lies in the fact that we can compute this quickly and determine how it changes via the use of XPP-Auto. Essentially, as we illustrate in a case study below, a stable steady state can be regarded as an attractor for trajectories and therefore a potential end point for navigators. If this is sufficiently close to the origin, the individuals can be assumed to have homed successfully. However, its imperfect nature stems from the fact that there may be multiple or no stable steady states, or that it may only act as an attractor for certain portions of the phase plane (i.e. only for a subset of initial locations). Furthermore, instead of finding how the average animal behaves we also want to consider how the initial starting position affects the animals ability to reach the stable steady state. The existence of a stable steady state close to a saddle node might prevent many individuals reaching the stable steady state and thus we also compute the homing value (see below). The code used for the stability analysis is included in Appendix A.

Therefore, we also determine homing success more robustly via the homing value. Specifically, we consider a grid of 100 points, given by a mesh of x and y whose coordinate values are selected from $\Omega = [-50\,, -40\,, -30\,, -20\,, -10\,, 10\,, 20\,, 30\,, 40\,, 50]$. We calculate the homing value by integrating the system of equations for the 100 initial locations $(x_i\,, y_j)$, where $i\,, j \in \Omega$, up to the nondimensional time of $t = 300$. The homing value HV_t is then taken to be the percentage of solutions that land within the circle of radius $A = 0.5$ or $A = 5$ at $t = 300$. Effectively, this assumes the target is a circular region either of radius 0.5 or 5 of the origin since we always model the target island at the origin.

4.3.3 Case study: Constant navigating cue

To illustrate these concepts in a case study, we consider the dynamical system generated for the constant cue case, as previously discussed in [74]. The dynamical system here is found to behave in two ways:

1. If $c_1(k) > u_x$ the three steady states in the system are: a (USS) unstable steady state at $(0\,, 0)$, a (S) saddle node at $\left(\frac{c_3(k)}{u_x + c_1(k)}\right)$ and a (SSS) stable steady state

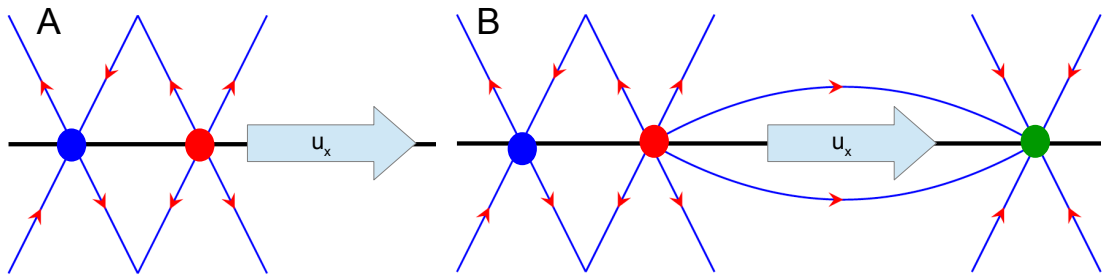

Figure 4.10: A schematic illustrating the steady states of the dynamical system (4.17)-(4.18) with constant navigating strength k. A) If $c_1(k) < u_x$ there are two steady states: saddle node $\left(\frac{c_3(k)}{u_x+c_1(k)}\right)$, blue circle, and unstable steady state $(0\,,0)$, red circle. B) If $c_1(k) > u_x$ there are three steady states: saddle node $\left(\frac{c_3(k)}{u_x+c_1(k)}\right)$, blue circle, unstable steady state $(0\,,0)$, red circle and stable steady state $\left(\frac{-c_3(k)}{c_1(k)-u_x}\right)$.

at $\left(\frac{-c_3(k)}{c_1(k)-u_x}\right)$. In this case, the stable steady state acts as an attractor for the system and trajectories, given enough time, will end up close to this point. Hence, the distance of this steady state from the centre of the origin serves to determine whether individuals would eventually home (see Figure 4.10B).

2. Otherwise there are two steady states: an unstable steady state at $(0\,,0)$, a saddle node at $\left(\frac{c_3(k)}{u_x+c_1(k)}\right)$. In this case, there is no attracting steady state and trajectories evolve over time away from the origin (see Figure 4.10A). Negligible homing is expected.

To illustrate the homing value for this case study, we calculate it as we vary the strength of k and animal movement speed s (see Figure 4.11). As expected increasing the strength k (i.e. making them better navigators) and the speed s (i.e. making them stronger active movers) increases the proportion of trajectories that end up close to the target, and hence generate higher values of HV_t. However, it is noted that the success of reaching the for the smaller target ($A = 0.5$) is considerably lower, illustrating that it is harder to find a smaller target. We further observe the effect of the flow, where larger flows restrict the parameter space for successful homing as individuals are more significantly deviated from their true course.

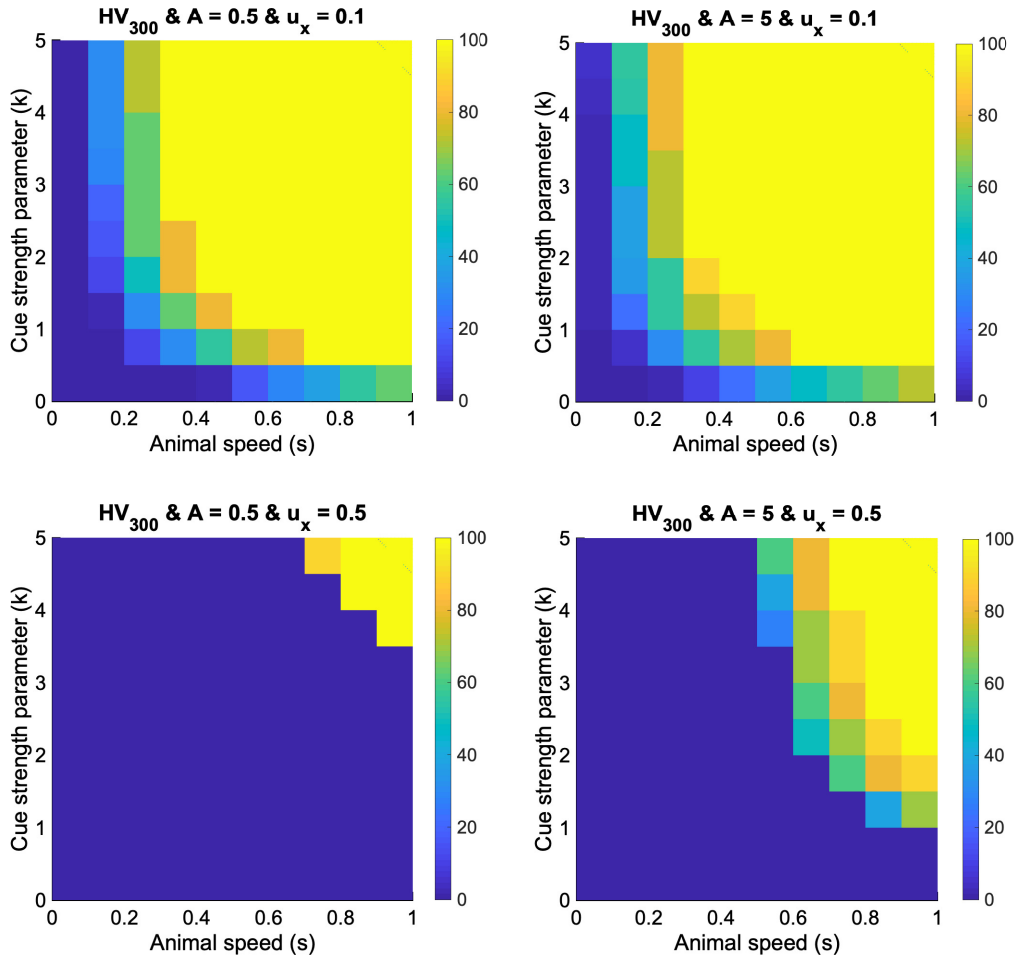

Figure 4.11: Homing values obtained using (4.17)-(4.18) for varying the constant navigating cue strength (k) and animal movement (s) with $\lambda = 1$. Top figures consider a passive flow characterised by $u_x = 0.1$, while the bottom figures correspond to the passive flow $u_x = 0.5$. Simulations were computed in MATLAB using code similar to the one in Section A.4.

4.3.4 Point-based navigation

Distance of stable steady state to target

We start by using XPP-Auto to determine the position, number and stability of under point-based cues. For purely increasing or purely decreasing cues we find that there is up to one stable steady state which, when it exists, can therefore act as an attractor for certain starting locations. We plot the position of this steady state with respect to the origin under certain parameter changes to understand the potential impact on homing. Figure 4.12 shows the impact of changing speed s

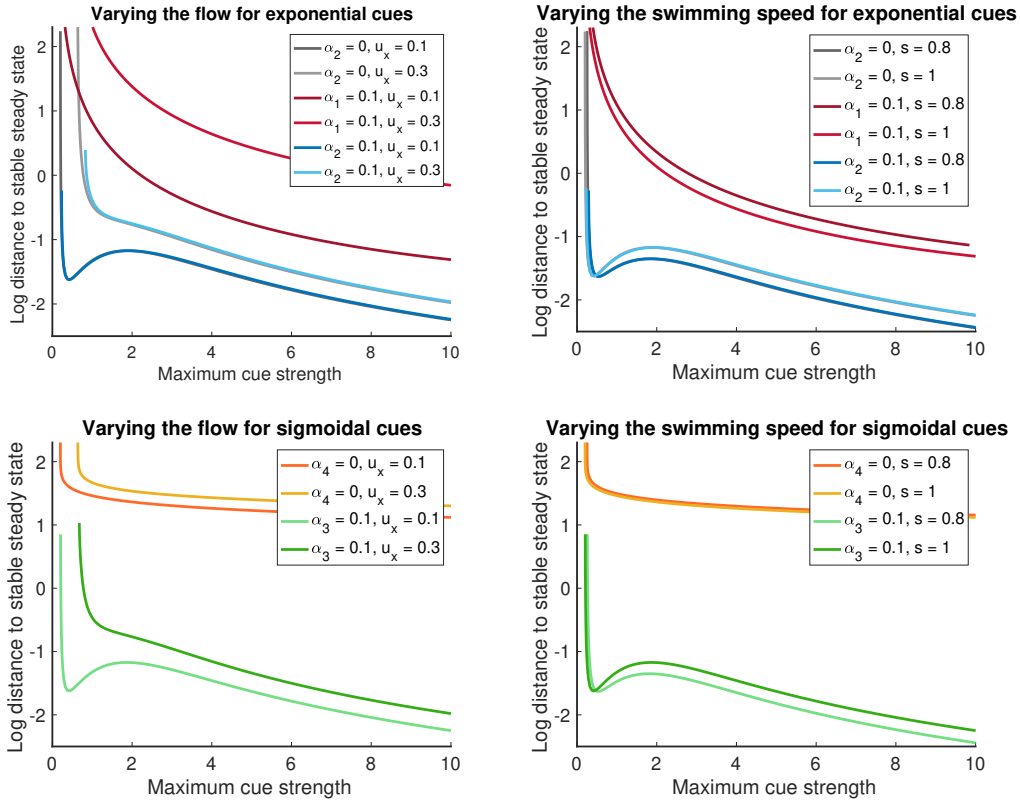

Figure 4.12: Log distance between the stable steady state for dynamical system (4.17)-(4.18) and the target for varying the speed of the animals s and the passive flow u_x for various combinations of navigating cues (4.19),(4.20). Where not stated otherwise we set $s = \lambda = 1$ and $u_x = 0.1$. We set $\lambda = 1$. Simulations were computed in XPP-Auto using code in Section A.3.

and the background flow u_x . As expected, increasing the passive flow acts to shift the stable steady state further away from the target location, since the flow knocks individuals off course. Much larger increases in the flow result in a loss of the stable steady state and homing fails, consistent with the constant cue case. Subtleties arise in the purely increasing/purely decreasing cue cases in terms of the speed, where increasing the speed of the animal brings the steady state closer to the origin for cues that increase with distance but the opposite effect for cues that decrease with distance. This is somewhat counter-intuitive, and we believe that it occurs through faster movement of animals resulting in an overshoot of their target location. Overall, for a purely increasing or purely decreasing cue we observe large variations in the position of the steady state as parameters are shifted, indicating their respective failures at robustly generating homing: for the purely increasing case, a cue may

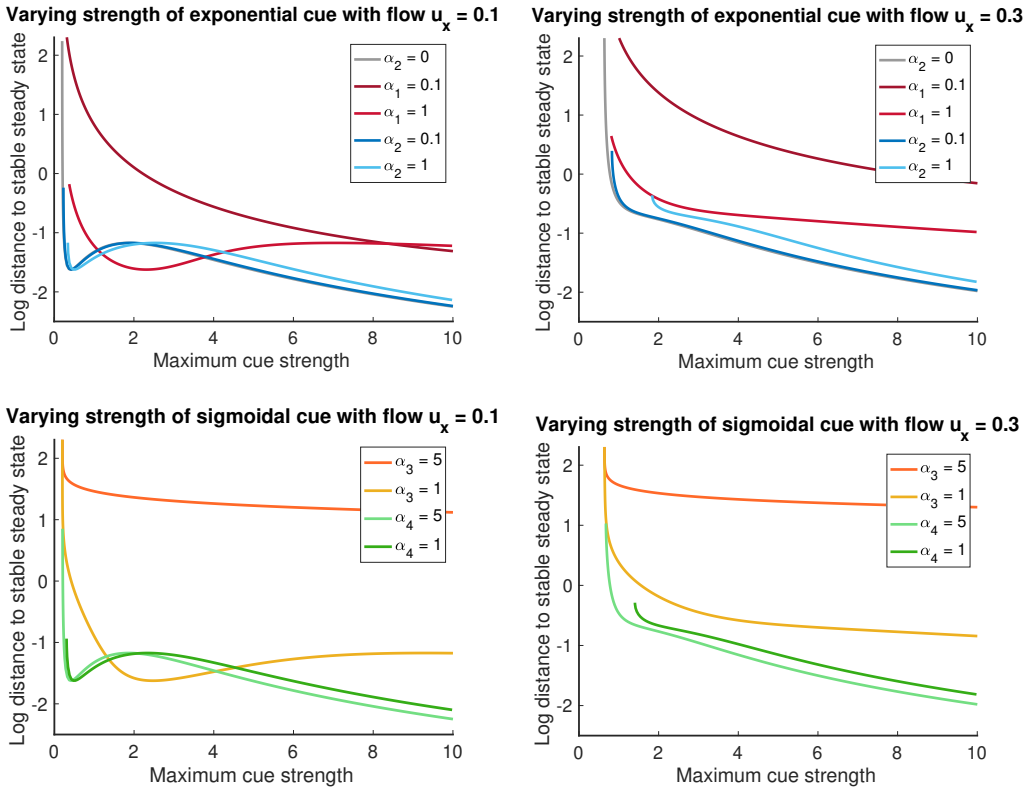

Figure 4.13: Log distance between the stable steady state for dynamical system (4.17)-(4.18) and the target for exponentially varying and constant cue strength (4.19),(top figure), and hyperbolic varying cue strength (4.20),(bottom figure). We set $s = \lambda = 1$. Simulations were computed in XPP-Auto using code in Section A.3.

allow individuals to arrive reasonably close to the goal but, at that point, fails to provide sufficient navigating information; for the purely decreasing case an individual far from the goal may simply not have enough guidance certainty to overcome passive flow.

We further remark that while Figure 4.13 implies that purely decreasing cues are generally more successful, in the sense of producing a stable steady state closer to the target location, we should remark on a factor highlighting the limitation of this measure for homing success. Specifically, for the decreasing cue scenario the phase plane of our dynamical system typically contains four steady states, highlighted in Figure 4.14, rather than the normal two or three as for the constant/increasing cue cases. While a stable steady state persists close to the origin – this is expected, as there is always strong navigating information within region – further away and downstream an additional saddle node is present. Consequently, individuals trapped

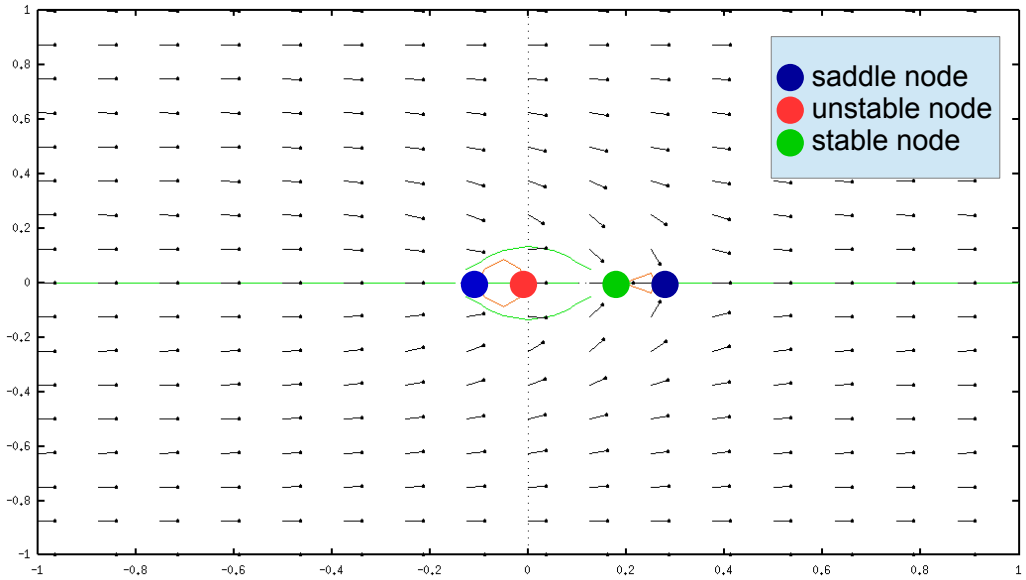

Figure 4.14: The vector field (black arrows) and nullclines (in green and red) of the dynamical system (4.17)-(4.18) with a cue decreasing exponentially with radial distance from the island (4.19) with $s = \lambda = 1\,, u_x = 0.1\,, \kappa_2 = 1$ and $\alpha_2 = 1$. The four steady states from left to right are a saddle node, an unstable node, a stable node and a saddle node. Simulations were computed in XPP-Auto using code in Section A.3.

far from the goal lie away from the zone of attraction for the stable steady state, and fail to home. Thus, for the purely decreasing case we expect successful homing to be highly dependent on starting location. This will be investigated further below.

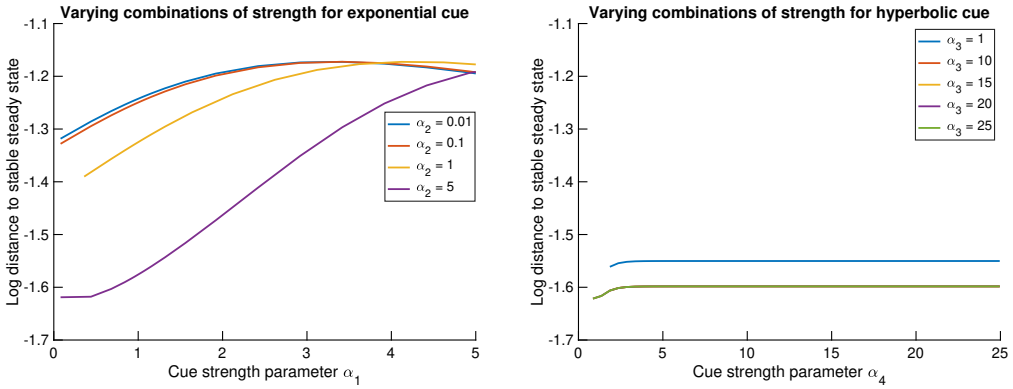

Figure 4.15: Log distance between the stable steady state for dynamical system (4.17)-(4.18) and the target with various combinations for of the exponential (4.19), left, and hyperbolic (4.20), right, cues. We set $s = \lambda = 1\,, u_x = 0.1$. Simulations were computed in XPP-Auto using code in Section A.3.

Figure 4.15 shows how the position of the steady state varies as we consider the scenarios corresponding to Figure 4.7 (iii-iv), i.e. corresponding to some cue combination of increasing and decreasing cues. Generally we observe far less variation in the position of the steady state, indicating greater robustness: effectively, the dual cues combine to provide compensatory guidance information.

Homing values

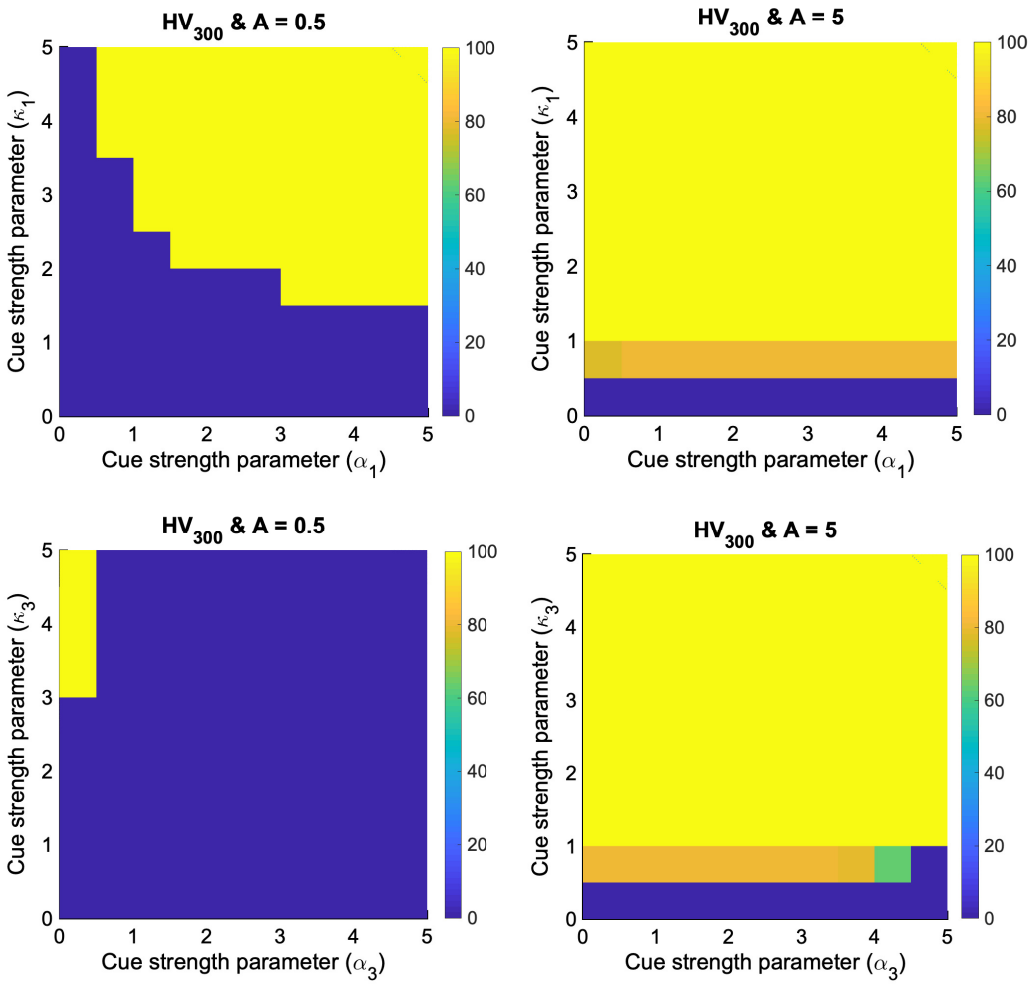

Figure 4.16: Homing values obtained using (4.17)-(4.18) with various cue strengths (4.19). We set $u_x = 0.3\,, s = \lambda = 1$. The top row shows the cues which increase with radial distance from the target location and the bottom row shows the cues that decrease with radial distance from the target location. Simulations were computed in MATLAB using code similar to the one in Section A.4.

We move on to consider a more nuanced measure, the homing value. Specifically,

the homing value provides information on the success over a range of starting positions, uniformly distributed over our study region. The homing value simulations are performed in Matlab [108].

Figure 4.16 indicates that whether employing exponential or hyperbolic cue forms, strong exponentially increasing cues that rapidly saturate at the maximum (i.e. largest $(\alpha_1\,,\kappa_1)$) give the best homing: this is as expected, as the cue rapidly acquires maximum navigating strength when still close to the target, and hence individuals can find the target. A cue that only reaches its maximum strength when far from the target, however, gives variable success and it further strongly depends on the target size. We note that purely decreasing cues resulted in zero homing value for the analogous parameter study. We believe that the poor homing success for decreasing cues occurs since the majority of starting locations start navigation from points where the cue is too weak for detection and movement is dominated by transport due to passive flow.

Figure 4.17 further substantiates the findings from [119]: combinations of weak cues will outperform strong single cues. Here we have set all strength parameters (κ) to 1 which, when a single purely increasing/decreasing cue is utilised, will lead to negligible homing value. Overall, we find that the exponential combination cues (see Figure 4.17) for the point source navigation are the most successful in bring animals close to their target locations; for the strongest parameter combination of these cues we get that 100% of the population is within a radius of 0.5 of the target location. Moreover, we see that most of the animals remain in the larger region of 5 throughout the simulation.

Finally, the studies in Figure 4.18 attempt to describe how animal migration is impacted by "blind zones" where the cue starts decreasing after a radial distance of 1 from the target and then increases again at distance $\alpha_3 > 1$. In other words, animals are given navigating information close to the target then encounter a region of zero navigating information for a given distance $(\alpha_3 - 1)$ before again obtaining navigation guidance. We see that there is very little effect on adding the decreasing cue close to the target. The combination of cues is, however, more successful at bringing animals critically close to the target location.

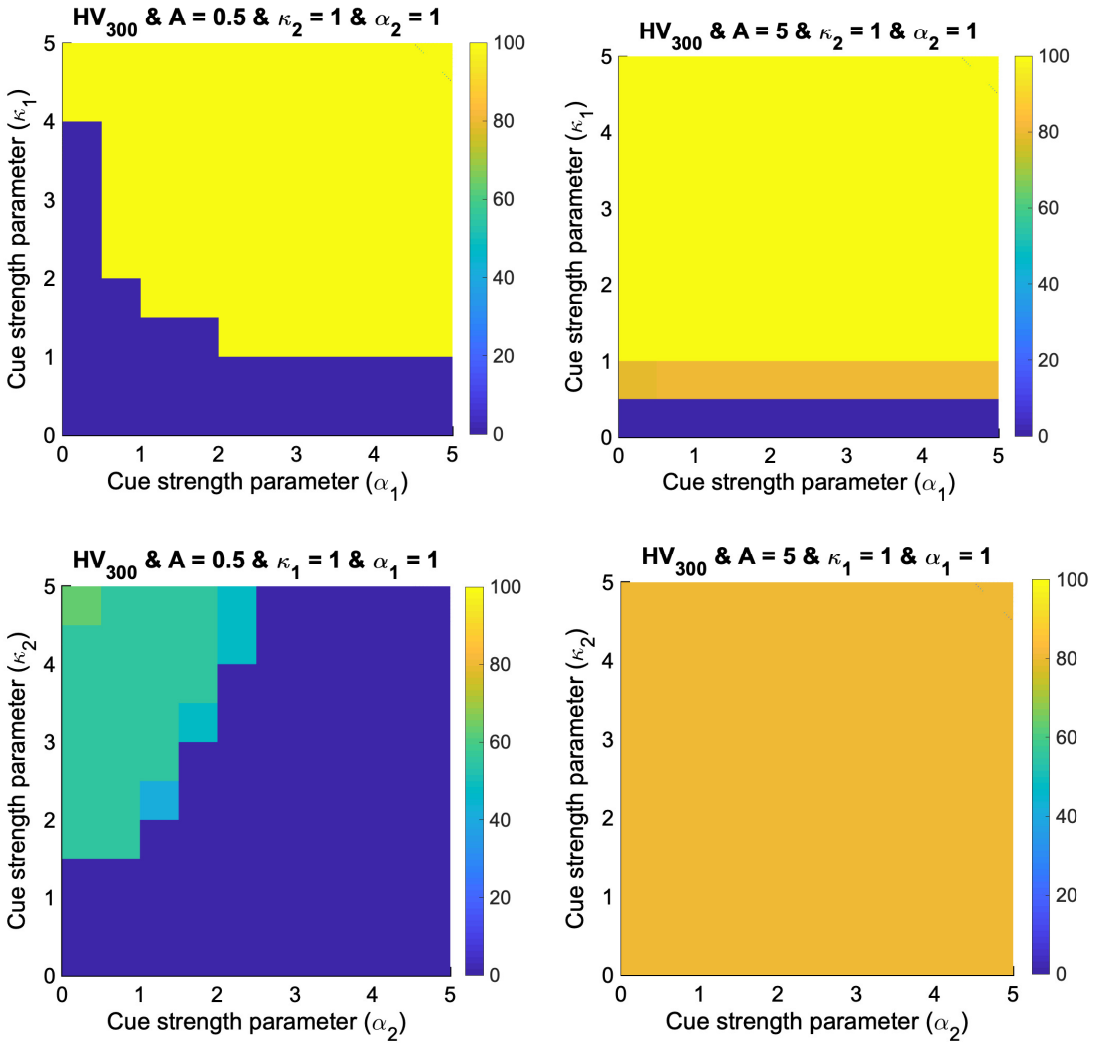

Figure 4.17: Homing values obtained using (4.17)-(4.18) with $s = \lambda = 1\,, u_x = 0.3$ using various cue strengths (4.19). Simulations were computed in MATLAB using code similar to the one in Section A.4.

4.3.5 Line based navigation

We turn our attention to line-based navigation. Note that in this case the exploration of steady-states under a single line-cue is less indicative: for a single line-based cue in the absence of flow, there will generally be a continuous line of steady states to which individuals are attracted. However, the simple of addition of flow disrupts this delicate balance, and there are no stable steady-states except in the unlikely scenario that the orientation of the cue is exactly perpendicular to the flow. We therefore confine our study to studying the trajectories of the dynamical system numerically.

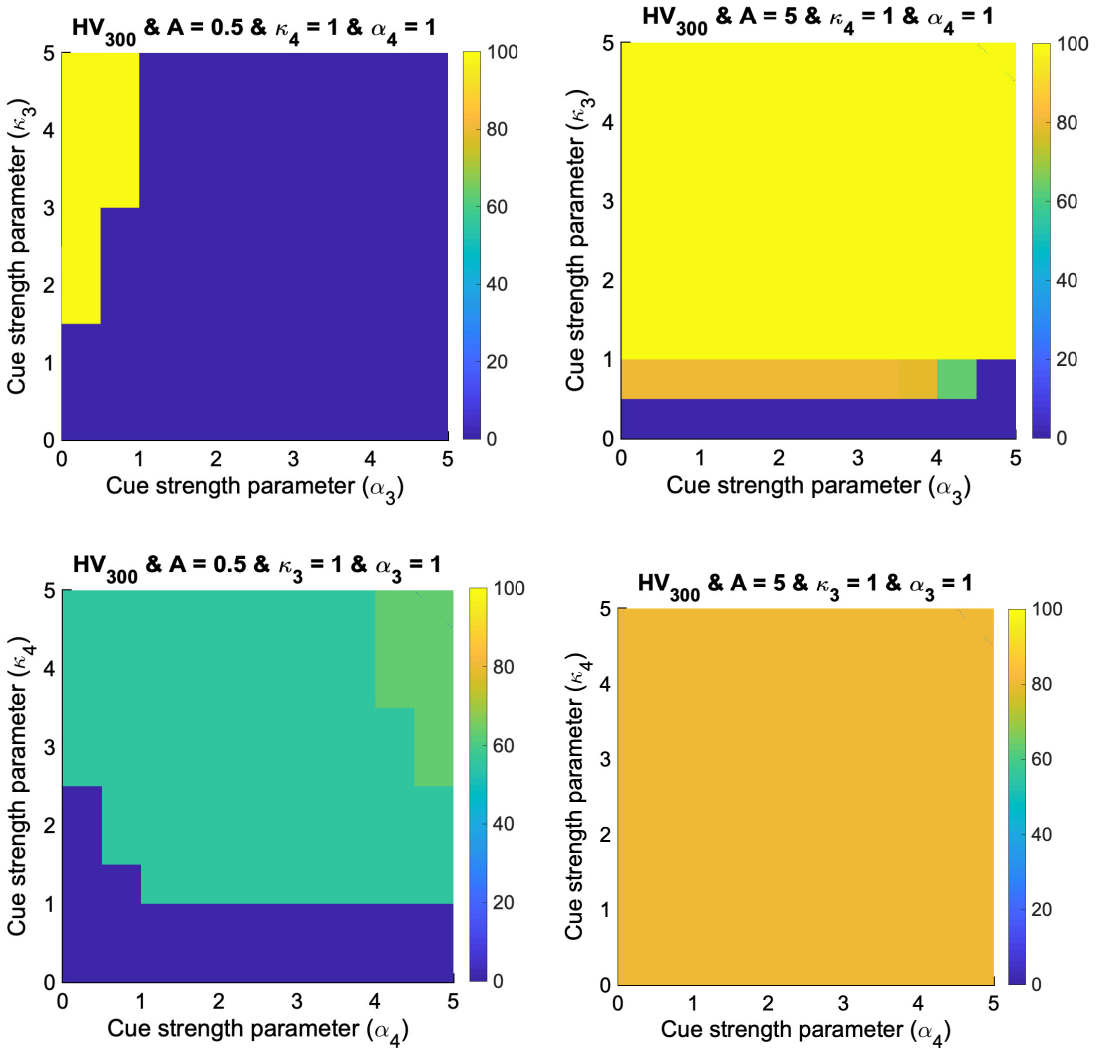

Figure 4.18: Homing values obtained using (4.17)-(4.18) with $s = \lambda = 1\,, u_x = 0.3$ using various cue strengths (4.20). Simulations were computed in MATLAB using code similar to the one in Section A.4.

Simulations plotted in Figure 4.19 illustrate the above: under a single line cues, we observe trajectories moving in the direction of the line cue, but subsequently are transported by the flow of the system. Thus, for a line cue oriented at 0^o (i.e. in the same direction of the flow), trajectories end up on the contour line intersecting the target but subsequently move rightwards due to the flow: whether or not an individual eventually finds the target will depend on whether it first lands on this line up or downstream. Pushing the orientation of the line cue to 90^o allows navigation onto a contour, but a subsequent trapping and failure to home. Allowing a combination

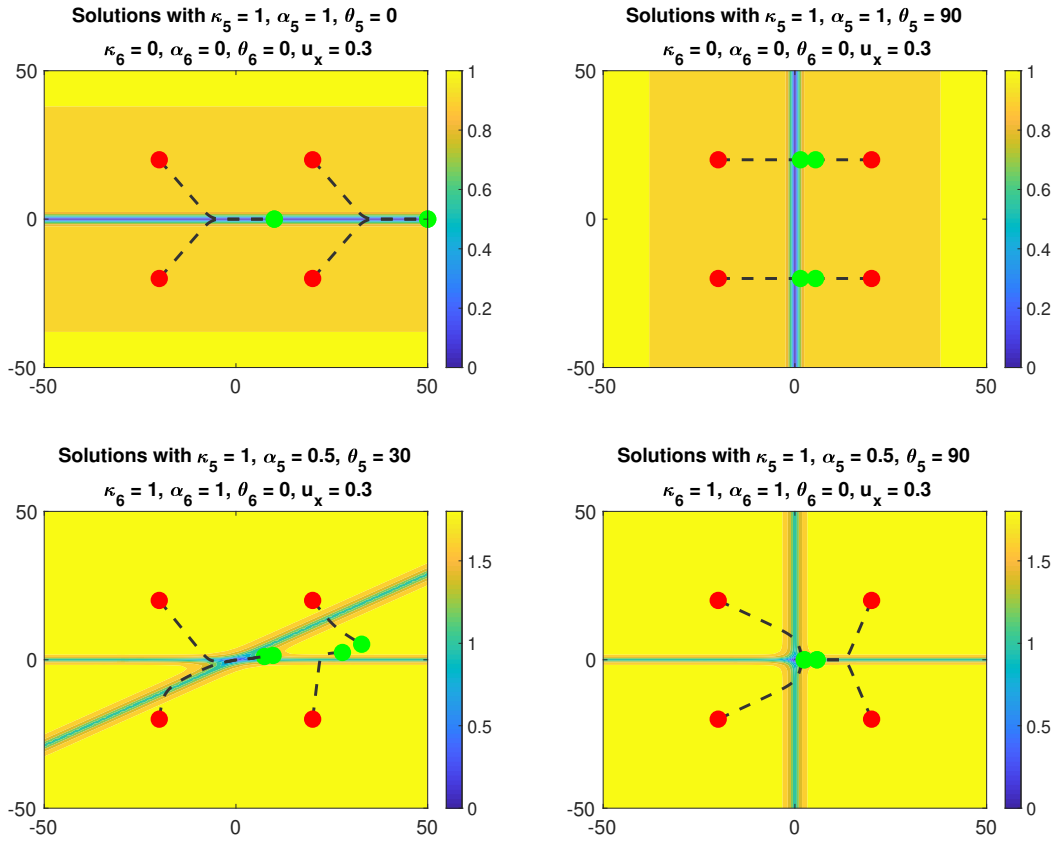

Figure 4.19: Solutions of (4.22)-(4.23) for one (top row) and two (bottom row) line cues (4.21). The colour bar shows the strength of the navigating field, the red dots shows the release positions $(-20,-20)$, $(-20,20)$, $(20,20)$ and $(20,-20)$, the lines show the paths taken and the green dots show the final position at time 100. We set $s = \lambda = 1$. Simulations were computed in MATLAB using code in Section A.4.

of line cues proves more successful, with a combination of two almost perpendicular cues providing the most effective homing. In this case, the two line-based cues combine to provide point-source information and homing is relatively successful.

We focus on the results of two line cues, comparing results for two parallel (see Figure 4.20 left hand side) and perpendicular cues (see Figure 4.20 right hand side). We see that the angle between the line cues strongly influences successful homing and we hypothesise that animals benefit from the use of perpendicular lines cues.

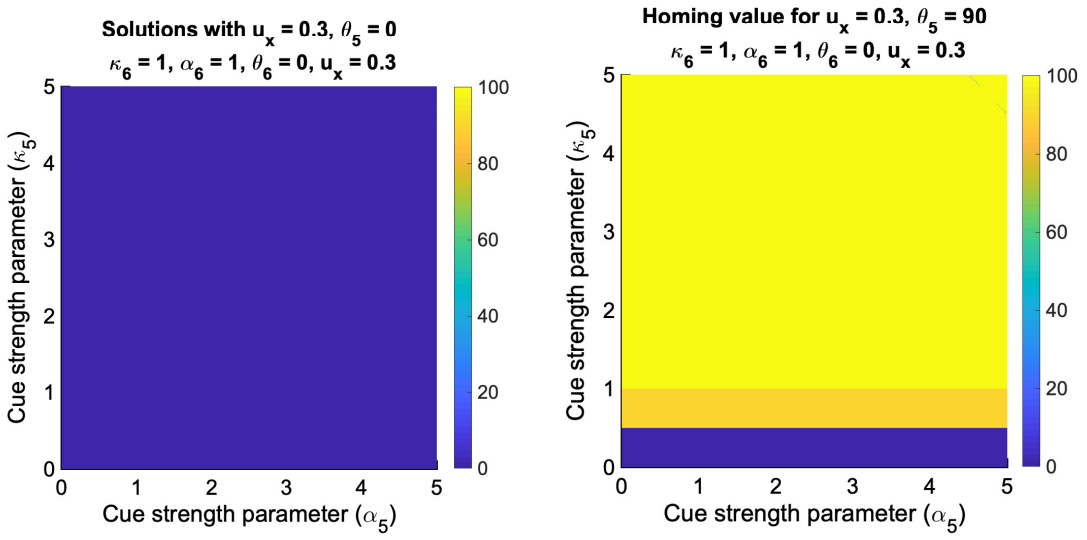

Figure 4.20: Homing values obtained using (4.22)-(4.23) for two line based cues (4.21) with $s = \lambda = 1\,, u_x = 0.3\,, A = 5$. Simulations were computed in MATLAB using code in Section A.4.

4.4 Discussion

The preliminary results presented here indicate that under point source navigating cues, a combination of several cues leads to more successful migration. We also note that, while cues which decrease with distance from the target location perform best at allowing a stable steady state to exist close to the target, the dynamical system itself brings an additional saddle node that pushes trajectories away from the target location for a large portion of the field. Thus, we would suggest that while long-scale navigations are possible for cues that increase with distance from the target, they are highly infeasible for those that decrease significantly with distance from the target.

Under line-based cues the use of two line cues almost orthogonally oriented to each other can effectively recapitulate the point-based cue effectiveness; under a single line cue, navigation is potentially possible but success would be highly critical according to the individual's starting position. In the context of turtle navigation this relates to the geographic location of two popular turtle homing sites: Ascension island and Koh Tao. Ascension island is located over 1600km to the nearest coast line (West Africa) and therefore it is crucial that turtles use two line cues to navigate. They are able to utilise the grid nature of the magnetic field intensity and inclination lines as they home. However Koh Tao includes magnetic field intensity and inclination

lines which are almost parallel to one another; therefore turtle rely on one line based cue. We hypothesise that the location of Koh Tao, on the coast of Thailand, means that turtles are able to use visual cues such as following the coast line to navigate successfully.

4.4.1 Mean first passage time

Due to the specific nature of our system we saw that the position of a steady state inside the system does not tell us the full history of animal migration. In fact having a close steady state could not fully reflect the details of the dynamical system which could push away much of the migratory animals very far away from the target location. In this section we include a discussion of the mean first passage time, our next aim in this work.

The *mean first passage time* is defined as the average time it takes for an event to first occur. In the context of animal navigation we are interested in the average time it takes for an animal to first reach position x during its migration. Since the steady states show us the behaviour of the system in a long time we cannot model if the animals reach the island in a given time. The time taken for migratory journeys is critical so we now choose to compute the mean first passage time. A real life example can be seen when turtles fail to reach their homing island fast enough and they navigate back to their main foraging coasts. Computing the mean first passage time will allow us to model how long a migratory journey will take from a given position. We make use of the first passage time and position jump random walk derivations [109, 118] to discuss our preliminary study. Specifically we will illustrate the derivation of the mean first passage time for our problem, but under a distinct underlying random walk.

Derivation of the Fully Anisotropic Advection-Diffusion from a position jump random walk

A position jump random walk describes the movement of an individual moving from position y to position x using instantaneous jumps. Whether a jump occurs between positions x and y with a small time step τ is determined according to redistribution kernel $K(x, y, t)$. We let $\rho(x, t)$ define the probability of an individual being at position x, time t .

We consider the change in the probability of an individual being at position x

at time t and $t+\tau$ by integrating over possible jumps to position x from a different position y and removing all jumps from position x for some position y. Hence, the master equation for a position jump random walk in 2D is defined as

$$\rho(x,t+\tau)-\rho(x,t)=\int_{D^x} K(x,y,t)\rho(y,t)-K(y,x,t)\rho(x,t)d\mu(y)\,. \tag{4.24}$$

where $(D^x,\mu(y))$ is a measure space which determines the set of spaces considered for possible jumps towards or away from. In our derivation D^x is the sphere in $S^1\subset\mathbb{R}^2$. Note that the redistribution kernel K is not symmetric.

We start by making two assumptions for the derivation of our position jump random walk:

1. We allow jumps into any direction, but to be set length δ. Note therefore that this sets the speed s $\approx \frac{\delta}{\tau}$.

2. The redistribution kernel depends on the environmental information at the individual's current position.

We can therefore write $K(y,x,t)=k(n,x,t)$ where $n=\frac{y-x}{|y-x|}$ and (4.24) becomes

$$\rho(x,t+\tau)-\rho(x,t)=\int_{S^1} K(n,x-\delta n,t)\rho(x-\delta n,t)-K(n,x,t)\rho(x,t)dn\,. \tag{4.25}$$

For deriving our system we set

$$k(n,x,t)=\frac{1}{A+F}\left(\frac{A}{2\pi I_0(k)}e^{knx}+F\delta_{\rho(x,t)}(n)\right)\,, \tag{4.26}$$

to describe that animals jump into a position x based on the strength A from their navigating abilities and the strength F of the passive flow. Here the Von Mises distribution is used to describe that with navigating strength k animals choose the next preferred direction whereas the passive advective field $\rho(x\,,t)$ moves them with strength F. Note that the point measure $\delta_{\rho(x,t)}(n)$ allows us to include external drift as seen in [118].

By expanding the right hand side of (4.25) for small values of τ and δ (using our

assumption that $s \approx \frac{\delta}{\tau}$) [118] we obtain that

$$\begin{aligned} \rho + \frac{\partial \rho}{\partial t}\tau - \rho + O(\tau^2) &= \int_{S^1} (k\rho - k\rho) dn - \delta \left(\nabla \cdot \int_{S^1} k n dn \right) \rho \\ &+ \frac{\delta^2}{2} \left(\nabla\nabla : \int_{S^1} n n^T k dn \right) \rho + O(\delta^3) \,. \end{aligned} \tag{4.27}$$

We can consider no loss boundary conditions, however this is not necessary for the purposes of the derivation. Further, this simplifies to

$$\frac{\partial \rho}{\partial t} + O(\tau) = -\frac{\delta}{\tau} \left(\nabla \cdot \int_{S^1} k n dn \right) \rho + \frac{\delta^2}{2\tau} \left(\nabla\nabla : \int_{S^1} n n^T k dn \right) \rho + O(\delta^3/\tau) \,. \tag{4.28}$$

We now define $\lim_{\delta,\tau \to 0} \frac{\delta^2}{2\tau} \approx d$ and $\lim_{\delta,\tau \to 0} \frac{\delta}{\tau} \int_{S^1} nk dn \approx c\delta$. We can use this in (4.28) and neglect higher order terms to obtain

$$\begin{aligned} &\frac{\partial \rho}{\partial t} + \nabla \cdot \left(c \int_{S^1} n k(n,x,t) dn \rho \right) \\ &= \nabla\nabla : (d \int_{S^1} (n - c \int_{S^1} n k(n,x,t) dn)(n - c \int_{S^1} n k(n,x,t) dn)^T k(n,x,t) dn \rho). \end{aligned} \tag{4.29}$$

Now, consider the redistribution kernel (4.26), to obtain

$$\begin{aligned} &\frac{\partial \rho}{\partial t} + \nabla \cdot \left(c \left(\frac{1}{A+F} \right) A \frac{I_1(k)}{I_0(k)} x + F \right) \rho \\ &= \nabla\nabla : \left(\left(d \left(\frac{A}{A+F} \right) \left(1 - \frac{I_2(k)}{I_0(k)} \right) x + \left(\frac{I_2(k)}{I_0(k)} - \frac{I_1(k)^2}{I_0(k)^2} \right) x \right) \rho \right) \end{aligned} \tag{4.30}$$

Note that we have therefore derived the Fully Anisotropic Advection-Diffusion (FAAD) equation as noted in (4.4) from a position jump process, instead of the velocity jump process, if we define

$$a(x,t) = c \int_{S^1} n k(n,x,t) dn \,, \tag{4.31}$$

and

$$\mathbb{D}(x,t) = d \int_{S^1} (n - a(x,t))(n - a(x,t))^T k(n,x,t) dn \,. \tag{4.32}$$

Mean passage time

We can now use the same redistribution kernel for our derivation of the mean first passage time. We first let $T(x)$ define the mean passage time from the location x. We can define our mean passage time as

$$T(x) = \tau + \int_{S^1} k(x\,, x + n\delta\,, \tau) T(x + n\delta) dn\,, \tag{4.33}$$

where τ defines the time increment taken to move using the redistribution kernel $k(x\,, x+n\delta\,, \tau)$ from position x to position $x+n\delta$. Next we make use of the modelling assumption that our animals move at a constant speed and consider the limit of the step size. Using the redistribution kernel (4.26) allows us to obtain the mean passage time using Taylor expansions alike the ones we used to obtain the FAAD (4.29) from the position jump random walk (4.24). We use [109] and the derivations of the moments computed in [72] to obtain

$$(a(x\,, t)) \cdot \nabla T(x) + \nabla\nabla : \mathbb{D}(x\,, t) T(x) + 1 = 0\,, \tag{4.34}$$

where $a(x\,, t)\,, \mathbb{D}(x\,, t)$ are defined analogously to equations (4.5) and (4.6) and F is the strength of the passive flow that the animals are navigating in. We find that

$$a(x\,, t) = \left(\frac{1}{A + F}\right) A \frac{I_1(k)}{I_0(k)} x + F\,, \tag{4.35}$$

and

$$\mathbb{D}(x\,, t) = \left(\frac{A}{A + F}\right) \left(1 - \frac{I_2(k)}{I_0(k)}\right) x + \left(\frac{I_2(k)}{I_0(k)} - \frac{I_1(k)^2}{I_0(k)^2}\right) x\,. \tag{4.36}$$

In the future we will analyse (4.34) to discuss how various positions in our system determine the mean time it takes for an animal to migrate to a given location. We note here that, to our knowledge, a mean first passage time has not been derived directly from a velocity jump process and therefore our illustration above is currently for a position jump process.

As a first attempt of computing the finite element numerical simulation of (4.34) we let $a(x, t) = 0$ and $\mathbb{D}(x, t) = I_2$ where I_2 is the 2D identity matrix. In this way

we want to solve

$$\Delta T(x) = -1, \qquad in \quad \Omega, \tag{4.37}$$

which represents the mean first passage time of animals diffusing with no passive flow or advection included in their motion. Our domain of interest is $\Omega = 1 \leq \sqrt{x^2 + y^2} \leq 10$ and we define the boundary conditions as Dirichlet

$$T(x) = 0, \quad \partial\Omega_1 := \{\sqrt{x^2 + y^2} = 1\} \tag{4.38}$$

and Neumann

$$\partial_n T(x) = 0, \quad \partial\Omega_2 := \{\sqrt{x^2 + y^2} = 10\} \tag{4.39}$$

We obtain the variational formulation [98] by first multiplying (4.37) by a test function $v \in H^1(\Omega)$ and integrating with respect to x while using integration by parts to obtain

$$\int_\Omega \nabla T(x) \cdot \nabla v - \int_{\partial\Omega} \frac{\partial T(x)}{\partial n} v ds = \int_\Omega v dx. \tag{4.40}$$

Next we use the boundary conditions and solve $T(x)$ such that

$$\int_\Omega \nabla T(x) \cdot \nabla v - \int_{\partial\Omega} \frac{\partial T(x)}{\partial n} v ds = \int_\Omega v dx. \tag{4.41}$$

The solution we obtain in Fenics [7] can be seen in Figure 4.21. As expected, with the island located at the origin with the radius set to 10 we see that the result shows symmetric mean first passage time in all directions since we have no flow or advection and as we increase the distance from the origin the mean first passage time increases. Animals that are located further from the island will take much longer to get to it.

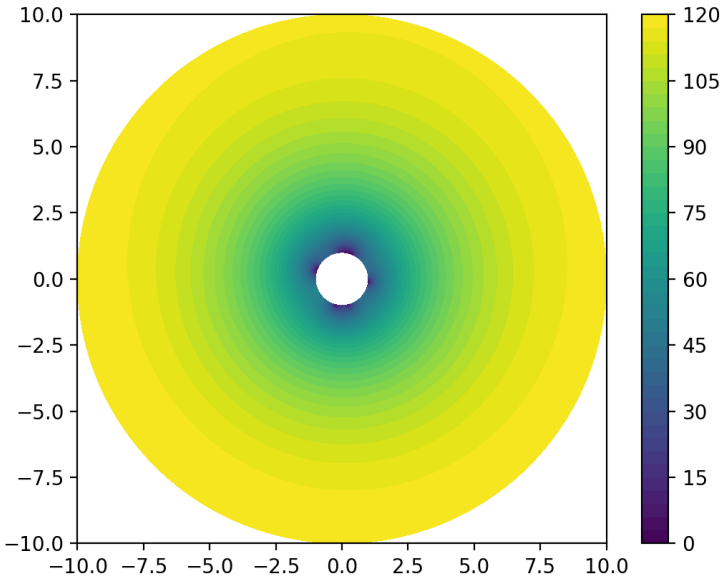

Figure 4.21: Numerical simulation of (4.41) from Fenics using the code in Appendix A.5. Colourbar shows the mean first passage time for the given geometry $\Omega = 1 \leq \sqrt{x^2 + y^2} \leq 10$.

Chapter 5

Conclusions

This thesis explores two very different aspects of mathematical biology. As the main research topic we study the self-organisation of the microtubule cytoskeleton using stochastic simulations and probabilistic models. We also explore models of animal navigation based on continuous models derived from agent-based velocity jump processes. Here we discuss the main results and explore outlooks of future work; in particular we outline a research direction where we will be able to make use of methods from both of these topics.

5.1 Results

5.1.1 Self-organisation of the microtubule cytoskeleton

In Chapter 2, we discovered the robustness of the self-organisation of the microtubule cytoskeleton in *Drosophila* epithelial cells. We ran a large sensitivity analysis using stochastic simulations on the cluster and predicted that the microtubule angle distribution remains unchanged for cells of the same eccentricity. An important part of our collaboration with the group of Dr. Natalia Bulgakova was to reproduce experimentally observed results, but also to motivate new experiments. Our predictions from the stochastic stimulations were confirmed experimentally, concluding that microtubule self-organisation is robust on the tissue scale. The robustness of the system allowed us to build a minimal probabilistic model and show that the robustness of the microtubule self-organisation is inherent to the system due to the separation of scales between the rates of polymerisation and depolymerisation and the small rates of catastrophe and rescue. We showed that the only factor besides geometry that

influences microtubule self-organisation is the density of the microtubule minus-ends.

In Chapter 3, we illustrated how anisotropies in the cytoplasm bias the direction of microtubule self-organisation along the anisotropy. We expanded our probabilistic model and carried out further stochastic simulations to test isotropic and anisotropic barriers to microtubule polymerisation inside the cell. We found that if barriers are placed within the cell at a given angle, the microtubule cytoskeleton will progressively assemble in the direction of the anisotropy as the strength of the barrier is increased. We complimented this theoretical work with experiments on the *Drosophila* follicular epithelium tissue, where actin cables align microtubules in the direction of the anisotropy.

5.1.2 Animal navigation

In Chapter 4, we have shown the need for analysis of dynamical systems of animal navigation beyond finding the steady states of the system. After a large agent-based study of turtles homing to Ascension Island using various navigating cues, we concluded that several weak cues can outperform one strong cue. Through studying the dynamical system of characteristics, which represents the average movement of animals, in an abstract model we found that simply measuring the location of steady states in the system may not accurately describe the behaviour of migratory animals. We concluded that to study animal navigation we have to take account of the full field as saddle or unstable node could result in splitting of the plane ensuring up to half of a migratory population does not reach the target. We discussed the need for computing the mean passage time to elucidate more details of the problem. The first attempt of finding the mean passage time for our system can be found in Section 4.4.1.

5.2 Future work

5.2.1 Self-organisation of the microtubule cytoskeleton

Our model of microtubule dynamics contains the minimal amount of information required to describe the system and predict new biological properties. The agreement between the theory and experiments is especially remarkable considering the intrinsic noise in biological systems. Some aspects of future work could include:

- Using a Bayesian statistics approach to fit our models to the provided experimental data (eg. [25].
- Determining the slow-time dynamics of the microtubule minus-end distribution;
- Including elasticity into the parameterisation of the microtubule interaction dynamics (eg. [36, 135, 154, 82]);
- Modelling the cell and microtubules in 3D;
- Including the effect of the viscous cytoplasm into the model.

However, including any of these modelling assumption would introduce further unknowns into the system which could result in data overfitting as opposed to generating meaningful biological conclusions.

There are many exciting questions that remain open for our system such as: What keeps microtubules anchored in the adhesion plane? What keeps the centrosome below the adhesion plane? Why do the centrosomal microtubules point downwards? While we cannot study these questions in the *in vivo* system given the current stage of experimental setup, mathematical modelling could provide some insights to these questions for future experimental testing.

Most research leads to new questions; this is particularly apt for our model of microtubule self-organisation, where we showed the asymmetric seed distribution of elongated *Drosophila* cells. A clear modelling question is how do the microtubule seeds move during the stages 12-15 of development? Is the asymmetry simply a result of stretching occurring unevenly along the cell membrane? We know, experimentally, that there is a feedback mechanism which occurs between the microtubule self-organisation and which affects the relocation of microtubule minus ends. The feedback mechanism occurs on the time scale of hours, therefore we have not discussed it here, however a future model could include a growing boundary with microtubule minus-ends changing their location with time in order to understand how microtubule self-organisation is impacted. Mathematically, this involves studying transport via molecular motors along microtubules, and coupling motor transport on short time scales (seconds) to microtubule self-organization on longer time-scales (minutes), to the long-term establishment of the result of intracellular transport on very long time scales (perhaps tens of minutes or hours).

5.2.2 Transport models

There are many new avenues for future research in modelling transport. In particular, we would like to further develop the model of transport for animal navigation and to create a model to describe the transport of E-cadherin along the microtubule network.

Animal navigation

One question, inspired by the turtle study at Ascension Island, is to investigate various turtle nesting locations such as Koh Tao or Galapagos. These locations include magnetic field information, ocean and wind data which differs greatly from the data at Ascension Island. For example, the magnetic field intensity and inclination lines at Koh Tao are parallel to each other, unlike Ascension Island where the lines are almost perpendicular. Comparing these location studies along with GPS tracking routes of turtles at these locations could provide insight into the nature of turtle homing specific to the outlined regions.

Another point of interest for animal navigation models is the mean first passage time. Due to the nature of the dynamical systems that are obtained from our models for animal navigation the mean first passage time could be an ideal measure for studying migration. In particular we see the derivation of the mean first passage time from a velocity jump process as an open topic.

Asymmetry of E-cadherin

A future direction of study would be to investigate the transport of E-cadherin along the microtubule cytoskeleton. This would use the microtubule network obtained from Chapter 2 along with the methods discussed in Chapter 4 (agent-based to continuum modelling) to describe the asymmetric distribution of E-cadherin that is observed experimentally [22]. As a long term approach it would be interesting to model how the microtubule network (governed by microtubule seeds and cell geometry) impacts E-cadherin distribution and thus the properties of adhesion and tension at the cell boundary. An overarching goal would be to understand how the subcellular level effects like microtubule cytoskeleton self-organisation and E-cadherin transport affect tissue mechanics.

Appendices

Appendix A

Codes

A.1 MATLAB code for microtubule dynamics in 1D

The code included here shows the microtubule dynamics in 1D. Here there are no interactions as we are focusing on one microtubule minus end growing stochastically until it reaches a length of 100. This serves as an illustration of the full stochastic simulations used in Chapters 2 and 3 where microtubules grow in the same way. However in the full simulations we also take account of two microtubules crossing and their corresponding collision dynamics. For full details of the code see [58].

```
close all; clear all;

rng('shuffle');
%%% discrete barriers
a = 100;          % max microtubule length (until boundary)

%%% rates
alphapr   = 4;   % (rescue)
betapr    = 1;   % (catastrophe)
alpha     = 2*500; % (grow)
beta      = 3.5*alpha; % (shrink)
t_end     = 10000;
time      = 0;
capyesno  = 0;
bigstate  = [alphapr;0]; % (initial seed state)
```

```
L = zeros(1e8,1); C = L;
ind = 1;
T_nonzero = 0;


%%% stochastics
while ((time<t_end) ),

    bigsum  = sum(bigstate);
    ab = min(find(rand<cumsum(bigstate/bigsum)));
    % find which action is going to take place

    % microtubule will grow or undergo catastrophe
    if capyesno>0.5,

        if ab > 0.5 && L(ind,1)<a;

            % GROW

            if L(ind,1)>0
                capyesno = 1; bigstate = [alpha;betapr];
                % add dimer
                L(ind+1,1) = L(ind,1) + 1;
            end

        else
            % get cap, update bigstate
            capyesno = 1; bigstate = [alpha;betapr];
            L(ind+1,1) = L(ind,1) + 1;
        end


    else

        % CATASTROPHE
```

```
        if L(ind,1)>0,
            % lose cap, update bigstate
            L(ind+1,1) = L(ind,1) - 1;
            capyesno = 0; bigstate = [alphapr;beta];
        else
            % last dimer to shrink > seed state
            capyesno = 1; bigstate = [alphapr;0];
            L(ind+1) = 0;
        end

    end

    else

        % RESCUE
        if ab > 0.5 && L(ind,1)<a;

            if L(ind,1)>0

                % keep going, barrier
                L(ind+1,1) = L(ind,1) + 1;
                capyesno = 1; bigstate = [alpha;betapr];


            else
                % get cap, update bigstate
                L(ind+1,1) = L(ind,1) + 1;
                capyesno = 1; bigstate = [alpha;betapr];


            end

        elseif ab <= 0.5
            % SHRINK
```

```
            if L(ind,1)>1,
                % decrease by dimer
                capyesno = 0; L(ind+1,1) = L(ind,1) - 1;
            else
                % last dimer > seed state
                capyesno = 1; bigstate = [alphapr;0];
            end
        end
end

% time increment
ddt = log(1/rand)/bigsum;
time = time  + ddt;
ind = ind + 1;
t(ind) = time;
C(ind) = capyesno;

if L(ind,1)>0,
    T_nonzero = T_nonzero + ddt;
end

end

cycles =  length(find(C(1:length(t))==0)) - 1;
```

A.2 Agent based simulations for turtle study

This section describing the details of the numerical simulations has been included in [119]. Virtual tracks and population distributions are computed by adapting a previously developed multiscale framework [119]. In the agent based model (ABM) virtual turtle agents are immersed into a flow field representing ocean currents. Agent motion in the ABM derives from ocean current drift and oriented swimming, the latter described by a "velocity-jump" random walk consisting of smooth swims with fixed

heading interspersed by reorientation. Note that detailed tracks obtained from "crittercams" attached to loggerhead turtles suggest this to be a reasonable approximation of oriented swimming behaviour. Further to vector fields for ocean currents (u_{ocean}), the critical statistical inputs for parametrising this model are: (i) the average speed (s); (ii) the average rate of reorientations (λ); (iii) a directional distribution $q(\alpha)$ for turning into a new heading, angle α. The distribution q allows navigation to be entered, via biasing turns into specific angles. We employ the von Mises distribution, a standard in animal navigation studies. Specifically,

$$q(\alpha|k, A) = \frac{1}{2\pi I_0(k)} e^{k\cos(\alpha - A)} . \tag{A.1}$$

The parameters k and A denote the navigational strength and dominant angle respectively: large k generate a majority of turns within a few degrees of the dominant angle A, while for negligible k no particular angle is favoured. Cues typically vary spatially and/or temporally, so k and A are functions of t and x. $I_j(k)$ denotes the modified Bessel function of first kind (order j) and enters as a normalising factor.

The distribution (A.1) is parametrised via the consolidated navigation field, a vector field $w_C(x, t)$ that combines individual cue fields into a single entity that confers navigation information. The individual cue fields are taken to be as follows:

- w_T and w_I, respectively describing responses to geomagnetic total intensity and inclination angle;
- w_W and w_O, respectively describing responses to windborne and oceanborne odours.

Each of these are characterised by two parameters, k_i and κ_i, where $i \in T, I, O, W$. The former is a strength measure for the maximum "certainty" by which an agent follows a particular field, while the latter reflects the sensitivity of detection. Individual fields are combined into the consolidated field through simple summation ($w_C = w_T + w_I + w_O + w_W$). We subsequently take $k(x, t) = |w_C(x, t)|$ and $A(x, t)$ as the angle in the direction of $w_C(x, t)$ in Equation (A.1).

Ocean currents, surface winds and magnetic field components are obtained from standard (public domain) datasets: HYCOM for ocean currents, ASCAT measurements for surface winds and the IGRF model for the magnetic field, see [119].

Numerical methods are adapted from our previous studies (e.g. see [74]) and described briefly below. Initially we note that the computational domain differs

from the study region, extending two degrees longer in each dimension: in effect, turtles can leave the $10^o \times 10^o$ study region at one point and re-enter elsewhere. This practice allows specification of appropriate boundary conditions on the study region to be circumvented: on the computational domain edges we impose lossless boundary conditions for the turtles (turtles are, in effect, reflected) while chemical substances are allowed to flow across its edges. We note, however that the size of the computational domain is sufficiently large that the exact choice has negligible impact on the results presented. As a second remark, we note that computer simulations run for $t \in [-30, 100]$, where $t = 0$ denotes the point of release and $t = 100$ marks the final day of turtle tracking. The initiation of simulations 30 days before the release date ensures any odour plume has become established by the time of release.

The computational method used for the ABM combines stochastic simulations of each individual's velocity-jump random path with (when necessary) a numerical approximation for the continuous equation for plume dynamics. The numerical scheme is programmed using MATLAB. For the stochastic component, each particle is initiated at $t = 0$ with a position reflecting the stated initial conditions. Its movement path is subsequently generated through direct stochastic simulation of (4.1) according to the active and passive movement characteristics. The time discretisation Δt used in simulation is suitably small, in the sense that a set of representative simulations conducted with smaller timesteps generate near identical results. For the selection of new active headings via the directional distribution given in (A.1) we employ code (circ vmrnd.m) from the circular statistics toolbox. Currents and the inputs required for the active heading choice are interpolated from the native spatial/temporal resolutions in the saved variables to the individual particle's continuous position x and time t via a simple linear interpolation scheme.

A.3 XPP-Auto code used for stability analysis

This code was written in XPP-Auto [45] (available at `http://www.math.pitt.edu/~bard/xpp/xpp.html`) to find the steady states for the exponentially varying cue with radial distance (4.17,4.18).

```
p kappa1=0,ca1=0,kappa2=1,ca2=0,const_k=0.001

p ux=0.1,lambda=1,s=1
```

```
c1(x,y)=s*besseli(1,kappa1*(1-exp(-ca1*sqrt(x^2+y^2)))+...
const_k+kappa2*(exp(-ca2*sqrt(x^2+y^2))))/...
besseli(0,kappa1*(1-exp(-ca1*sqrt(x^2+y^2)))...
+const_k+kappa2*(exp(-ca2*sqrt(x^2+y^2))))

c3(x,y)=s^2/lambda*(besseli(2,kappa1*(1-exp(-ca1*sqrt(x^2+y^2)))+...
const_k+kappa2*(exp(-ca2*sqrt(x^2+y^2))))/...
besseli(0,kappa1*(1-exp(-ca1*sqrt(x^2+y^2)))...
+const_k+kappa2*(exp(-ca2*sqrt(x^2+y^2))))...
-(besseli(1,kappa1*(1-exp(-ca1*sqrt(x^2+y^2)))...
+const_k+kappa2*(exp(-ca2*sqrt(x^2+y^2)))))^2/...
(besseli(0,kappa1*(1-exp(-ca1*sqrt(x^2+y^2)))...
+const_k+kappa2*(exp(-ca2*sqrt(x^2+y^2)))))^2)

x'=ux-c1(x,y)*x/sqrt(x^2+y^2)-c3(x,y)*x/(x^2+y^2)

y'=-c1(x,y)*y/sqrt(x^2+y^2)-c3(x,y)*y/(x^2+y^2)

done
```

We start by running this code in XPP. To carry out the bifurcation analysis in Auto and find how the behaviour of a steady state changes with a given parameter we follow the following steps:

1. Use "View Axes" to change the limits of the phase plane to our domain of interest with $x \in (-10, 10), y \in (-10, 10)$. Note: the calculations were repeated with a larger domain size of $x \in (-100, 100), y \in (-100, 100)$ but no further steady states were found.

2. Use "Nullcline", "New" to find all steady states of the system for the given parameters.

3. Type "S" to find steady states and use option "Mouse" to consider one of the steady states (locations where the two nullclines cross). Then once you click on the initial guess choose to print the eigenvalues and XPP describes the type of steady state.

4. To carry out the continuation for the steady state click import and then choose "File", "Auto" from the menu options.

5. Specify the domain for computation using the "Numerics" option in the Auto window. Choose the continuation parameter from the "Parameter" tab in Auto and then click "Run" to solve the continuation.

6. Finally choose "File" and "Write Pts" to save the data onto your home directory for plotting.

A.4 MATLAB code used for computing the homing values

This code was written in MATLAB version 2018 [108] to compute the homing values for line based cues seen in (4.22,4.23).

```
close all; clear all;

% parameters
lambda = 1; s = [1]; ux = [0.3];

%line cue angles
ang1_list = [30]*pi/180;
ang2_list = [0]*pi/180;

% directory
dir_name = ['/home/ap45/Documents/turtle_hv/'];

time = [300];

% cue parameters
kappa1_list = [3.5:0.5:5];
alpha1_list = [0.5:0.5:5];
kappa2_list = [0];
alpha2_list = [0];
```

```
% mesh of initial locations
init_x_list = [-50 -40 -30 -20 -10 10 20 30 40 50];
init_y_list = [-50 -40 -30 -20 -10 10 20 30 40 50];

for aa = 1:length(ang1_list),
ang1 = ang1_list(aa);

for bb = 1:length(ang2_list),
ang2 = ang2_list(bb);

for cc = 1:length(kappa1_list),
kappa1 = kappa1_list(cc);

for dd = 1:length(alpha1_list),
alpha1 = alpha1_list(dd);

for ee = 1:length(kappa2_list),
kappa2 = kappa2_list(ee);

for ff = 1:length(alpha2_list),
alpha2 = alpha2_list(ff);


% read in divergence, computed from separate files
divx = csvread(['div_x_ang1_',num2str(ang1*180/pi),...
'_kappa1_',num2str(kappa1),'_alpha1_',num2str(alpha1),...
'_ang2_',num2str(ang2*180/pi),'_kappa2_',num2str(kappa2),'...
_alpha2_',num2str(alpha2),'.csv']);

divy = csvread(['div_y_ang1_',num2str(ang1*180/pi),...
'_kappa1_',num2str(kappa1),'_alpha1_',num2str(alpha1),...
'_ang2_',num2str(ang2*180/pi),'_kappa2_',num2str(kappa2),...
'_alpha2_',num2str(alpha2),'.csv']);

L = -350 : 1 : 350;
```

```
[xmesh,ymesh] = meshgrid(L , L);
xmesh = xmesh(:);
ymesh = ymesh(:);

for gg = 1:length(init_x_list),
init_x = init_x_list(gg);


for hh = 1:length(init_y_list),
init_y = init_y_list(hh);

tspan = [0 time];

# stiff ode solver
[t,y] = ode15s(@(t,y)[ux+besseli(1,kappa1*(1-...
exp(-alpha1*abs((tan(ang1)...
*y(1)-y(2))/sqrt(tan(ang1)^2+1)))))/...
besseli(0,kappa1*(1-exp(-alpha1*abs((tan(ang1)...
*y(1)-y(2))/sqrt(tan(ang1)^2+1)))))...
*cos(((y(2)<=tan(ang1)*y(1))...
*(ang1+pi/2)+(y(2)>tan(ang1)*y(1))*(ang1-pi/2)))...
+besseli(1,kappa2*(1-exp(-alpha2*abs((tan(ang2)...
*y(1)-y(2))/sqrt(tan(ang2)^2+1)))))/...
besseli(0,kappa2*(1-exp(-alpha2*abs((tan(ang2)...
*y(1)-y(2))/sqrt(tan(ang2)^2+1)))))...
*cos(((y(2)<=tan(ang2)*y(1))*(ang2+pi/2)...
+(y(2)>tan(ang2)*y(1))*(ang2-pi/2))) -...
input_divergence_x(y(1),y(2),divx,xmesh,ymesh,L);...
besseli(1,kappa1*(1-exp(-alpha1*abs((tan(ang1)*y(1)-y(2))...
/sqrt(tan(ang1)^2+1)))))/besseli(0,kappa1*...
(1-exp(-alpha1*abs((tan(ang1)*y(1)-y(2))/...
sqrt(tan(ang1)^2+1)))))*sin(((y(2)<=tan(ang1)...
*y(1))*(ang1+pi/2)+(y(2)>tan(ang1)...
*y(1))*(ang1-pi/2)))+besseli(1,kappa2*(1-exp(-alpha2*abs((tan(ang2)...
*y(1)-y(2))/sqrt(tan(ang2)^2+1)))))/...
```

```
besseli(0,kappa2*(1-exp(-alpha2*abs((tan(ang2)*y(1)-y(2))/...
sqrt(tan(ang2)^2+1)))))*sin(((y(2)<=tan(ang2)...
*y(1))*(ang2+pi/2)+(y(2)>tan(ang2)*y(1))...
*(ang2-pi/2)))-...
input_divergence_y(y(1),y(2),divy,xmesh,ymesh,L)]...
,tspan,[init_x; init_y]);

                % save final positions
            ANSWER_x(gg,hh) = y(end,1);
            ANSWER_y(gg,hh) = y(end,2);
            ANSWER_t(gg,hh) = t(end);

end
end
end
end
end
end
end
end
```

A.5 Python code used for computing the mean first passage time

This code was written in Python version 3.7.3 available at `http://www.python.org` and uses Fenics [7], an open source finite element software available at `https://fenicsproject.org`, which uses Dolfin [99] to compute the mean first passage time.

```
from dolfin import *
from mshr import *
import matplotlib.pyplot
import math

# Create mesh and define function space
inner_circle_radius = 1
```

```
outer_circle_radius = 10
domain = Circle(Point(0, 0), outer_circle_radius)
       - Circle(Point(0, 0), inner_circle_radius)
mesh = generate_mesh(domain, 200)

V = FunctionSpace(mesh, "Lagrange", 1)

# Define Dirichlet boundary (x = 0 or x = 1)
def boundary(x, on_boundary):
    r = math.sqrt(x[0] * x[0] + x[1] * x[1])
    return r < inner_circle_radius

# Define boundary condition
u0 = Constant(0.0)
bc = DirichletBC(V, u0, boundary)

# Define variational problem
u = TrialFunction(V)
v = TestFunction(V)
f = Constant(1.0)
g = Constant(0.0)
a = inner(grad(u), grad(v))*dx
L = f*v*dx + g*v*ds

# Compute solution
u = Function(V)
solve(a == L, u, bc)

# Plot solution
p = plot(u, interactive=True)
matplotlib.pyplot.colorbar(p);
matplotlib.pyplot.show()
```

Bibliography

[1] F. Ahmad and P. Baas. Beyond taxol: microtubule-based treatment of disease and injury of the nervous system. *Brain*, 136:2937–2951, 2013.

[2] B. Aigouy, R. Farhadifar, D. B. Staple, A. Sagner, J. Roper, F. Julicher, and S. Eaton. Cell flow reorients the axis of planar polarity in the wing epithelium of Drosophila. *Cell*, 142:773–786, 2010.

[3] S. Åkesson, A. C. Broderick, F. Glen, B. J. Godley, P. Luschi, F. Papi, and G. C. Hays. Navigation by green turtles: which strategy do displaced adults use to find ascension island? *Oikos*, 103:363–372, 2003.

[4] S. Åkesson, S. Capogrossi, G. C. Hays, P. Luschi, and F. Papi. Open-sea migration of magnetically disturbed sea turtles. *Journal of Experimental Biology*, 203:3435–3443, 2000.

[5] A. Akhmanova and M. O. Steinmetz. Control of microtubule organization and dynamics: two ends in the limelight. *Nature Reviews Molecular Cell Biology*, 16:711–26, 2015.

[6] B. Alberts, D. Bray, K. Hopkin, A. D. Johnson, J. Lewis, M. Raff, K. Roberts, and P. Walter. *Essential Cell Biology*. Garland Science, New York, USA, 3rd edition, 2013.

[7] M. S. Alnæs, J. Blechta, J. Hake, A. Johansson, B. Kehlet, A. Logg, C. Richardson, J. Ring, M. E. Rognes, and G. N. Wells. The fenics project version 1.5. *Archive of Numerical Software*, 3, 2015.

[8] D. A. Andow, P. M. Kareiva, S. A. Levin, and A. Okubo. Spread of invading organisms. *Landscape Ecology*, 4:177–188, 1990.

[9] T. Antal, P. L. Krapivsky, S. Redner, M. Mailman, and B. Chakraborty. Dynamics of an idealized model of microtubule growth and catastrophe. *Physical Review E*, 76:041907, 2007.

[10] G. Apodaca. Endocytic traffic in polarized epithelial cells: Role of the actin and microtubule cytoskeleton. *Traffic*, 2:149–159, 2001.

[11] J. Baek, J. Lee, H. S. Yun, C. Lee, J. Song, H. Um, J. Park, I. Park, J. Kim, E. Kim, and S. Hwang. Kinesin light chain-4 depletion induces apoptosis of radioresistant cancer cells by mitochondrial dysfunction via calcium ion influx. *Cell Death & Disease*, 9:496, 2018.

[12] A. Banino, C. Barry, B. Uria, C. Blundell, T. Lillicrap, P. Mirowski, A. Pritzel, M. J. Chadwick, T. Degris, J. Modayil, et al. Vector-based navigation using grid-like representations in artificial agents. *Nature*, 557:429–433, 2018.

[13] R. Berenbaum, C. Heller, D. Hillis, and D. Sadava. *Life: the Science of Biology*. Sinauer Associates, Inc., Sunderland, USA, 9th edition, 2010.

[14] P. Berens. Circstat: A MATLAB toolbox for circular statistics. *Journal of Statistical Software*, 31:1–21, 2009.

[15] A. Berk and H. Lodish. *Molecular Cell Biology*. W. H. Freeman, New York, USA, 5th edition, 2000.

[16] D. Bernoulli. Réflexions sur les avantages de l'inoculation. *Mém. Paris*, 1:439–482, 1758.

[17] R. Blakemore. Magnetotactic bacteria. *Science*, 190:377–379, 1975.

[18] L. C. Boles and K. J. Lohmann. True navigation and magnetic maps in spiny lobsters. *Nature*, 421:60–63, 2003.

[19] A. H. Brand and N. Perrimon. Targeted gene expression as a means of altering cell fates and generating dominant phenotypes. *Development*, 118:401–415, 1993.

[20] G. J. Brouhard. Dynamic instability 30 years later: complexities in microtubule growth and catastrophe. *Molecular Biology of the Cell*, 26:1207–1210, 2015.

[21] L. Brun, B. Rupp, J. J. Ward, and F. Nédélec. A theory of microtubule catastrophes and their regulation. *Proceedings of the National Academy of Sciences*, 106(50):21173–21178, 2009.

[22] N. Bulgakova, I. Grigoriev, A. Yap, A. Akhmanova, and N. Brown. Dynamic microtubules produce an assymetric E-cadherin-Bazookacomplex to maintain segment boundaries. *The Journal of Cell Biology*, 201:887–901, 2013.

[23] N. A. Bulgakova and N. H. Brown. Drosophila p120-catenin is crucial for endocytosis of the dynamic E-cadherin–Bazooka complex. *Journal of Cell Science*, 129:477–482, 2016.

[24] D. Calligaris, P. Verdier-Pinard, F. Devred, C. Villard, D. Braguer, and D. Lafitte. Microtubule targeting agents: from biophysics to proteomics. *Cellular and Molecular Life Sciences*, 67:1089–1104, 2010.

[25] E. Campillo-Funollet, C. Venkataraman, and A. Madzvamuse. Bayesian parameter identification for turing systems on stationary and evolving domains. *Bulletin of mathematical biology*, 81(1):81–104, 2019.

[26] N. Carlile, D. Priddel, and J. Madeiros. Establishment of a new, secure colony of endangered Bermuda Petrel Pterodroma cahow by translocation of near-fledged nestlings. *Bird Conservation International*, 22:46–58, 2012.

[27] A. Carr, D. W. Ehrenfeld, and A. L. Koch. The problem of open-sea navigation: the migration of the green turtle to ascension island. *Journal of Theoretical Biology*, 22:163–179, 1969.

[28] Y. Chen and T. Hill. Monte Carlo study of the GTP cap in a five-start helix model of a microtubule. *Cell Biology*, 82:1131–1135, 1985.

[29] C. Conde and A. Cáceres. Microtubule assembly, organization and dynamics in axons and dendrites. *Nature Reviews Neuroscience*, 10:319–332, 2009.

[30] Wikipedia contributors. Bird migration – Wikipedia, the free encyclopedia. `https://en.wikipedia.org/w/index.php?title=Bird_migration&oldid=894825057`. Online; accessed 30-April-2019.

[31] C. E. Cook, M. T. Bergman, R. D. Finn, G. Cochrane, E. Birney, and R. Apweiler. The European Bioinformatics Institute in 2016: data growth and integration. *Nucleic Acids Research*, 44:D20–D26, 2015.

[32] F. Crick. *What Mad Pursuit: a Personal View of Scientific Discovery.* BasicBooks, New York, USA, 1st edition, 1988.

[33] C. Darwin. Origin of certain instincts. *Nature*, 7:417–418, 1873.

[34] A. Datar, J. Ameeramja, A. Bhat, R. Srivastava, R. Bernal, J. Prost, A. Callan-Jones, and P. A. Pullarkat. The roles of microtubules and membrane tension in axonal beading, retraction, and atrophy. *bioRxiv*, page 575258, 2019.

[35] E. E. Deinum. *Simple models for complex questions on plant development.* PhD thesis, Wageningen University, Wageningen, Netherlands , 2013.

[36] M. A. Deriu, M. Soncini, M. Orsi, M. Patel, J. W. Essex, F. M. Montevecchi, and A. Redaelli. Anisotropic elastic network modeling of entire microtubules. *Biophysical Journal*, 99:2190–2199, 2010.

[37] P. Dhonukshe and T. W. J. Gadella. Alteration of microtubule dynamic instability during preprophase band formation revealed by yellow fluorescent protein–CLIP170 microtubule plus-end labeling. *The Plant Cell*, 15:597–611, 2003.

[38] J. A. Dix and A. S. Verkman. Crowding effects on diffusion in solutions and cells. *Annual Review of Biophysics*, 37:247–263, 2008.

[39] R. Dixit and R. Cyr. Encounters between dynamic Cortical microtubules promote ordering of the Cortical array through angle-dependent modifications of microtubule behavior. *The Plant Cell*, 16:3274–3284, 2004.

[40] M. Dogterom and G. H. Koenderink. Actin–microtubule crosstalk in cell biology. *Nature Reviews Molecular Cell Biology*, 20:38–54, 2018.

[41] C. Dumontet and M. Jordan. Microtubule-binding agents: a dynamic field of cancer theurapetics. *Nature Reviews Drug Discovery*, 9:790–803, 2010.

[42] C. Egevang, I. J. Stenhouse, R. A. Phillips, A. Petersen, J. W. Fox, and J. RD. Silk. Tracking of Arctic terns Sterna paradisaea reveals longest animal migration. *Proceedings of the National Academy of Sciences*, 107:2078–2081, 2010.

[43] J. R. Ellis. Macromolecular crowding: obvious but underappreciated. *Trends in Biochemical Sciences*, 26:597–604, 2001.

[44] C.S. Endres, N.F. Putman, D.A Ernst, J.A. Kurth, C.M.F. Lohmann, and K. J. Lohmann. Multi-modal homing in sea turtles: Modeling dual use of geomagnetic and chemical cues in island-finding. *Frontiers in Behavioral Neuroscience*, 10:19, 2016.

[45] B. Ermentrout. *Simulating, analyzing, and animating dynamical systems: a guide to XPPAUT for researchers and students*. Siam, Philadelphia, USA, 1st edition, 2002.

[46] S. R. Farkas and H. H. Shorey. Chemical trail-following by flying insects: a mechanism for orientation to a distant odor source. *Science*, 178:67–68, 1972.

[47] R. A. Fisher. The wave of advance of advantageous genes. *Annals of Eugenics*, 7:355–369, 1937.

[48] The National Center for Biomedical Ontology. Drosophila Development Ontology. `http://bioportal.bioontology.org/ontologies/FB-DV/?p=classes&conceptid=http%3A%2F%2Fpurl.obolibrary.org%2Fobo%2FFBdv_00005327`. Online; accessed 5-August-2019.

[49] P. J. Foster, S. Fürthauer, M. J. Shelley, and D. J. Needleman. Active contraction of microtubule networks. *eLife*, 4:e10837, 2015.

[50] M.A. Franker and C. C. Hoogenraad. Microtubule-based transport - basic mechanisms, traffic rules and role in neurological pathogenesis. *Journal of Cell Science*, 126:2319–29, 2013.

[51] K. Von Frisch. Decoding the language of the bee. *Science*, 185:663–668, 1974.

[52] J. A. Gagnon and K. L. Mowry. Molecular motors: directing traffic during RNA localization. *Critical Reviews in Biochemistry and Molecular Biology*, 46:229–39, 2011.

[53] T. Gao, R. Blackwell, M. A. Glaser, M. D. Betterton, and M. J. Shelley. Multiscale polar theory of microtubule and motor-protein assemblies. *Physical Review Letters*, 114:048101, 2015.

[54] T. Gilbert, A. Le Bivic, A. Quaroni, and E. Rodriguez-Boulan. Microtubular organization and its involvement in the biogenetic pathways of plasma membrane proteins in caco-2 intestinal epithelial cells. *The Journal of Cell Biology*, 113:275–288, 1991.

[55] W.R. Gilks, S. Richardson, and D. Spiegelhalter. *Markov Chain Monte Carlo in Practice*. Chapman and Hall, New York, USA, 1st edition, 1995.

[56] F. Gittes, B. Mickey, J. Nettleton, and J. Howard. Flexural rigidity of microtubules and actin filaments measured from thermal fluctuations in shape. *The Journal of Cell Biology*, 120:923–934, 1993.

[57] N. Glade, J. Demongeot, and J. Tabony. Microtubule self-organisation by reaction-diffusion processes causes collective transport and organisation of cellular particles. *BMC Cell Biology*, 5:23, 2004.

[58] J. M. Gomez, L. Chumakova, N. A. Bulgakova, and N. H. Brown. Microtubule organization is determined by the shape of epithelial cells. *Nature Communications*, 7:13172, 2016.

[59] J. M. Gomez, Y. Wang, and V. Riechmann. Tao controls epithelial morphogenesis by promoting Fasciclin 2 endocytosis. *The Journal of Cell Biology*, 199:1131–1143, 2012.

[60] H. V. Goodson and E. M. Jonasson. Microtubules and microtubule-associated proteins. *Cold Spring Harbor Perspectives in Biology*, 10:a022608, 2018.

[61] S. S. Goodwin and R. D. Vale. Patronin regulates the microtubule network by protecting microtubule minus ends. *Cell*, 143:263–274, 2010.

[62] J. L. Gould and C. G. Gould. *Nature's Compass: the Mystery of Animal Navigation*. Princeton University Press, Princeton, USA, 1st edition, 2012.

[63] V. Grimm, E. Revilla, U. Berger, F. Jeltsch, W. M. Mooij, S. F. Railsback, H. Thulke, J. Weiner, T. Wiegand, and D. L. DeAngelis. Pattern-oriented modeling of agent-based complex systems: lessons from ecology. *Science*, 310:987–991, 2005.

[64] K. G. Hales, C. A. Korey, and A. M. Larracuenteand D. M. Roberts. Genetics on the fly: A primer on the drosophila model system. *Genetics*, 201:815–842, 2015.

[65] O. Hamant, D. Inoue, D. Bouchez, J. Dumais, and E. Mjolsness. Are microtubules tension sensors? *Nature Communications*, 10:2360, 2019.

[66] S. F. Hamm-Alvarez. Molecular motors and their role in membrane traffic. *Advanced Drug Delivery Reviews*, 29:229–242, 1998.

[67] R. J. Hawkins, B. M. Mulder, and S. H. Tindemans. Survival of the aligned: ordering of the plant cortical microtubule array. *Physical Review Letters*, 104:058103, 2010.

[68] G. C. Hays, P. Luschi, R. Marsh, F. Papi, and C. Del Seppia. The navigational feats of green sea turtles migrating from Ascension island investigated by satellite telemetry. *Proceedings of the Royal Society of London B: Biological Sciences*, 265:2279–2284, 1998.

[69] G. C. Hays, R. Marsh, and R. Scott. A little movement orientated to the geomagnetic field makes a big difference in strong flows. *Marine Biology*, 159:481–488, 2012.

[70] E. Herawati, D. Taniguchi, H. Kanoh, K. Tateishi, S. Ishihara, and S. Tsukita. Multiciliated cell basal bodies align in stereotypical patterns coordinated by the apical cytoskeleton. *The Journal of Cell Biology*, 214:571–586, 2016.

[71] J. T. Hester, C. M. F. Lohmann, and K. J. Lohmann. Long-distance navigation in sea turtles. *Ethology Ecology & Evolution*, 11:1–23, 1999.

[72] T. Hillen, K. J. Painter, A. C. Swan, and A. D. Murtha. Moments of von mises and fisher distributions and applications. *Mathematical Biosciences & Engineering*, 14(3):673–694, 2017.

[73] T. Hillen and K.J. Painter. Transport and anisotropic diffusion models for movement in oriented habitats. In *Dispersal, Individual Movement and Spatial Ecology*, pages 177–222. Springer, Berlin, Germany, 2013.

[74] T. Hillen and K.J. Painter. Navigating the flow: individual and continuum models for homing in flowing environments. *Journal of The Royal Society Interface*, 12:20150647, 2015.

[75] P. Hinow, V. Rezania, and J. A. Tuszyński. Continuous model for microtubule dynamics with catastrophe, rescue, and nucleation processes. *Physical Review E*, 80:031904, 2009.

[76] D. Holcman. *Stochastic Processes, Multiscale Modeling, and Numerical Methods for Computational Cellular Biology*. Springer, Cham, Switzerland, 1st edition, 2017.

[77] J. Horváth, I. Szalai, and P. De Kepper. An experimental design method leading to chemical Turing patterns. *Science*, 324:772–775, 2009.

[78] International Union for Conservation of Nature and Natural Resources. The IUCN red list of threatened species. `http://www.iucnredlist.org/about/summary-statistics#How_many_threatened`. Online; accessed 25-March-2019.

[79] P. Ioalè, M. Nozzolini, and F. Papi. Homing pigeons do extract directional information from olfactory stimuli. *Behavioral Ecology and Sociobiology*, 26:301–305, 1990.

[80] K. V. Iyer, R. Piscitello-Gomez, J. Paijmans, F. Julicher, and S. Eaton. Epithelial viscoelasticity is regulated by mechanosensitive E-cadherin turnover. *Current Biology*, 29:578–591, 2019.

[81] F. Jankovics and D. Brunner. Transiently reorganized microtubules are essential for zippering during Dorsal closure in it Drosophila melanogaster. *Developmental Cell*, 11:375–385, 2006.

[82] I. M. Janosi, D. Chretien, and H. Flyvbjerg. Modeling elastic properties of microtubule tips and walls. *European Biophysics Journal*, 27:501–513, 1998.

[83] D. St Johnston and J. Ahringer. Cell polarity in eggs and epithelia: parallels and diversity. *Cell*, 141:757–774, 2010.

[84] R. Kamm and M. Mofrad. *Cytoskeleton Mechanics: Models and Measurements in Cell Mechanics*. Cambridge University Press, New York, USA, 1st edition, 2006.

[85] L. C. Kapitein and C. C. Hoogenraad. Which way to go? cytoskeletal organization and polarized transport in neurons. *Molecular and Cellular Neuroscience*, 46:9–20, 2011.

[86] L. C. Kapitein and C. C. Hoogenraad. Building the Neuronal microtubule cytoskeleton. *Neuron*, 87:492–506, 2015.

[87] K. Kawaguchi and A. Yamaguchi. Temperature dependence rigidity of non-Taxol stabilized single microtubules. *Biochemical and Biophysical Research Communications*, 402:66–9, 2010.

[88] W. T. Keeton. Magnets interfere with pigeon homing. *Proceedings of the National Academy of Sciences*, 68:102–106, 1971.

[89] J. G. Kemeny and J. L. Snell. *Finite Markov Chains*. Van Nostrand, New Jersey, USA, 1st edition, 1960.

[90] J. S. Kennedy, A. R. Ludlow, and C. J. Sanders. Guidance system used in moth sex attraction. *Nature*, 288:475–477, 1980.

[91] A. B. Kolomeisky and M. E. Fisher. Molecular motors: A theorist's perspective. *Annual Review of Physical Chemistry*, 58:675–695, 2007.

[92] Y. Komarova, A. Akhmanova, S. Kojima, N. Galjart, and G. G. Borisy. Cytoplasmic linker proteins promote microtubule rescue in vivo. *The Journal of Cell Biology*, 159:589–599, 2002.

[93] Y. Komarova, C. O. De Groot, I. Grigoriev, S. M. Gouveia, E. L. Munteanu, J. M. Schober, S. Honnappa, R. M. Buey, C. C. Hoogenraad, M. Dogterom, G. G. Borisy, M. O. Steinmetz, and A. Akhmanova. Mammalian end binding proteins control persistent microtubule growth. *The Journal of Cell Biology*, 184:691–706, 2009.

[94] Y. Komarova, C. O. De Groot, I. Grigoriev, S. M. Gouveia, E. L. Munteanu, J. M. Schober, S. Honnappa, R. M. Buey, C. C. Hoogenraad, and M. Dogterom

et al. Mammalian end binding proteins control persistent microtubule growth. *The Journal of Cell Biology*, 184:691–706, 2009.

[95] Y. Komarova, G. Lansbergen, N. Galjart, F. Grosveld, G. G. Borisy, and A. Akhmanova. EB1 and EB3 control CLIP dissociation from the ends of growing microtubules. *Molecular Biology of the Cell*, 16:5334–5345, 2005.

[96] C. Leduc, K. Padberg-Gehle, V. Varga, D. Helbing, S. Diez, and J. Howard. Molecular crowding creates traffic jams of kinesin motors on microtubules. *Proceedings of the National Academy of Sciences*, 109:6100–6105, 2012.

[97] J. R. Levy, C. J. Sumner, J. P. Caviston, M. K. Tokito, S. Ranganathan, L. A. Ligon, K. E. Wallace, B. H. LaMonte, G. G. Harmison, I. Puls, K. H. Fischbeck, and E. L. F. Holzbaur. A motor neuron disease–associated mutation in p150 glued perturbs dynactin function and induces protein aggregation. *The Journal of Cell Biology*, 172:733–745, 2006.

[98] A. Logg, K. Mardal, and G. Wells. *Automated solution of differential equations by the finite element method: The FEniCS book*. Springer Science & Business Media, Heidelberg, Germany, 1st edition, 2012.

[99] Anders Logg and Garth N. Wells. Dolfin: Automated finite element computing. *ACM Transactions on Mathematical Software*, 37(2):20, 2010.

[100] C. Lohmann and K. J. Lohmann. Orientation and open-sea navigation in sea turtles. *Journal of Experimental Biology*, 199:73–81, 1996.

[101] K. J. Lohmann. Magnetic orientation by hatchling loggerhead sea turtles. *Journal of Experimental Biology*, 155:37–49, 1991.

[102] V. S. Lopes, D. Jimeno, K. Khanobdee, X. Song, B. Chen, S. Nusinowitz, and D. S. Williams. Dysfunction of heterotrimeric kinesin-2 in rod photoreceptor cells and the role of opsin mislocalization in rapid cell death. *Molecular Biology of the Cell*, 21:4076–4088, 2010.

[103] R. Loughlin, R. Heald, and F. Nedelec. A computational model predicts Xenopus meiotic spindle organization. *The Journal of Cell Biology*, 191:1239–1249, 2010.

[104] K. Luby-Phelps. Cytoarchitecture and physical properties of cytoplasm: volume, viscosity, diffusion, intracellular surface area. In *International Review of Cytology*, pages 189–221. Elsevier, Amsterdam, Netherlands, 2000.

[105] K. V. Mardia and P. E. Jupp. *Directional Statistics*. John Wiley & Sons, Hoboken, USA, 2 edition, 2009.

[106] A. A. Markov. An example of statistical investigation of the text eugene onegin concerning the connection of samples in chains. *Science in Context*, 19(4):591–600, 2006.

[107] I. Maryshev, D. Marenduzzo, A. B. Goryachev, and A. Morozov. Kinetic theory of pattern formation in mixtures of microtubules and molecular motors. *Physical Review E*, 97:022412, 2018.

[108] MATLAB. *version 4 (R2018b)*. The MathWorks Inc., Natick, Massachusetts, 2018.

[109] H. W. McKenzie, M. A. Lewis, and E. H. Merrill. First passage time analysis of animal movement and insights into the functional response. *Bulletin of Mathematical Biology*, 71:107–129, 2009.

[110] A. Mogilner and L. Edelstein-Keshet. Regulation of actin dynamics in rapidly moving cells: a quantitative analysis. *Biophysical journal*, 83(3):1237–1258, 2002.

[111] A. Mogilner and G. Oster. The polymerization ratchet model explains the force-velocity relation for growing microtubules. *European Biophysics Journal*, 28(3):235–242, 1999.

[112] T. Nakamura, N. Mine, E. Nakaguchi, A. Mochizuki, M. Yamamoto, K. Yashiro, C. Meno, and H. Hamada. Generation of robust left-right asymmetry in the mouse embryo requires a self-enhancement and lateral-inhibition system. *Developmental Cell*, 11:495–504, 2006.

[113] D. Nashchekin, A. Ribeiro Fernandes, and D. St. Johnston. Patronin/shot cortical foci assemble the noncentrosomal microtubule array that specifies the Drosophila anterior-posterior axis. *Developmental Cell*, 38:61–72, 2016.

[114] National Oceanic and Atmospheric Administration. US/UK World Magnetic Model Main Field Inclination (I). `https://www.ngdc.noaa.gov/geomag/WMM/data/WMM2015/WMM2015_I_MERC.pdf`. Online; accessed 5-June-2019.

[115] National Oceanic and Atmospheric Administration. US/UK World Magnetic Model Main Field Total Intensity (F). `https://www.ngdc.noaa.gov/geomag/WMM/data/WMM2015/WMM2015_F_MERC.pdf`. Online; accessed 5-June-2019.

[116] F. Nedelec and D. Foethke. Collective Langevin dynamics of flexible cytoskeletal fibers. *New Journal of Physics*, 9(11):427, 2007.

[117] H. G. Othmer, S. R. Dunbar, and W. Alt. Models of dispersal in biological systems. *Journal of Mathematical Biology*, 26:263–298, 1988.

[118] K. J. Painter and T. Hillen. From random walks to fully anisotropic diffusion models for cell and animal movement. In *Cell Movement*, pages 103–141. Springer, Berlin, Germany, 2018.

[119] K. J. Painter and A. Z. Plochocka. Efficiency of island homing by sea turtles under multimodal navigating strategies. *Ecological Modelling*, 391:40–52, 2019.

[120] F. Papi, P. Ioalè, V. Fiaschi, S. Benvenuti, and N. E. Baldaccini. Olfactory navigation of pigeons: the effect of treatment with odorous air currents. *Journal of Comparative Physiology*, 94:187–193, 1974.

[121] L. Parrott and R. Kok. A generic, individual-based approach to modelling higher trophic levels in simulation of terrestrial ecosystems. *Ecological Modelling*, 154:151–178, 2002.

[122] C. Peskin. Optimal dynamic instability of microtubules. *Documenta Mathematica, Extra Volume ICM*, 3:633–642, 1998.

[123] J. Phillips and S. C. Borland. Use of a specialized magnetoreception system for homing by the eastern red-spotted newt Notophthalmus viridescens. *Journal of Experimental Biology*, 188:275–291, 1994.

[124] R. Phillips, J. Theriot, J. Kondev, and H. Garcia. *Physical Biology of the Cell*. Garland Science, New York, USA, 2 edition, 2013.

[125] K. L. Pope and T. J. C. Harris. Control of cell flattening and junctional remodeling during squamous epithelial morphogenesis in Drosophila. *Development*, 135:2227–2238, 2008.

[126] S. Portet, J. A. Tuszynski, J. M. Dixon, and M. V. Sataric. Models of spatial and orientational self-organization of microtubules under the influence of gravitational fields. *Physical Review E*, 68(2):021903, 2003.

[127] P. Pritchard and C. Howard. The conservation of sea turtles: practices and problems. *American Zoologist*, 20:609–617, 1980.

[128] N. F. Putman, M. M. Scanlan, E. J. Billman, J. P. O'Neil, R. B. Couture, T. P. Quinn, K. J. Lohmann, and D. L. Noakes. An inherited magnetic map guides ocean navigation in juvenile Pacific salmon. *Current Biology*, 24:446–450, 2014.

[129] N. F. Putman, P. Verley, T. J. Shay, and K. J. Lohmann. Simulating transoceanic migrations of young loggerhead sea turtles: merging magnetic navigation behavior with an ocean circulation model. *Journal of Experimental Biology*, 215:1863–1870, 2012.

[130] J. Raspopovic, L. Marcon, L. Russo, and J. Sharpe. Digit patterning is controlled by a Bmp-Sox9-Wnt Turing network modulated by morphogen gradients. *Science*, 345:566–570, 2014.

[131] S. L. Rogers, G. C. Rogers, D. J. Sharp, and R. D. Vale. Drosophila EB1 is important for proper assembly, dynamics, and positioning of the mitotic spindle. *The Journal of Cell Biology*, 158:873–884, 2002.

[132] A. Roll-Mecak and R. D. Vale. The Drosophila homologue of the hereditary spastic Paraplegia protein, Spastin, severs and disassembles microtubules. *Current Biology*, 15:650–655, 2005.

[133] D. C. Rowland, Y. Roudi, M. Moser, and E. I. Moser. Ten years of grid cells. *Annual Review of Neuroscience*, 39:19–40, 2016.

[134] P.V. Ryder and D.A. Lerit. RNA localization regulates diverse and dynamic cellular processes. *Traffic*, 19:496–502, 2018.

[135] I. A. T. Schaap, C. Carrasco, P. J. de Pablo, F. C. MacKintosh, and C. F. Schmidt. Elastic response, buckling, and instability of microtubules under radial indentation. *Biophysical Journal*, 91:1521–1531, 2006.

[136] Science Communications Unit at the Mechanobiology Institute, National University of Singapore. How do actin filaments grow? `https://www.mechanobio.info/cytoskeleton-dynamics/what-is-the-cytoskeleton/what-are-actin-filaments/how-do-actin-filaments-grow/`. Online; accessed 15-January-2019.

[137] S. Sedwards and T. Mazza. Cyto-sim: a formal language model and stochastic simulator of membrane-enclosed biochemical processes. *Bioinformatics*, 23:2800–2802, 2007.

[138] M. R. Shaebani, A. Pasula, A. Ott, and L. Santen. Tracking of plus-ends reveals microtubule functional diversity in different cell types. *Scientific Reports*, 6:30285, 2016.

[139] A. Shamloo, F. Manuchehrfar, and H. Rafii-Tabar. A viscoelastic model for axonal microtubule rupture. *Journal of Biomechanics*, 48:1241–1247, 2015.

[140] E. Shelden and P. Wadsworth. Observation and quantification of individual microtubule behavior in vivo: microtubule dynamics are cell-type specific. *The Journal of Cell Biology*, 120:935–945, 1993.

[141] M. J. Shelley. The dynamics of microtubule/motor-protein assemblies in biology and physics. *Annual Review of Fluid Mechanics*, 48:487–506, 2016.

[142] N. T. Sherwood, Q. Sun, M. Xue, B. Zhang, and K. Zinn. Drosophila Spastin regulates synaptic microtubule networks and is required for normal motor function. *PLoS Biology*, 2:e429, 2004.

[143] Y. Shimada, S. Yonemura, H. Ohkura, D. Strutt, and T. Uemura. Polarized transport of frizzled along the planar microtubule arrays in Drosophila wing epithelium. *Developmental Cell*, 10:209–222, 2006.

[144] J. G. Skellam. Random dispersal in theoretical populations. *Biometrika*, 38:196–218, 1951.

[145] A. Sokolov and I. S. Aranson. Physical properties of collective motion in suspensions of bacteria. *Physical Review Letters*, 109:248109, 2012.

[146] A. J. Squarr, K. Brinkmann, B. Chen, T. Steinbacher, K. Ebnet, M. K. Rosen, and S. Bogdan. Fat2 acts through the WAVE regulatory complex to drive collective cell migration during tissue rotation. *The Journal of Cell Biology*, 212:591–603, 2016.

[147] M. Takeda, M. M. Sami, and Y. Wang. A homeostatic apical microtubule network shortens cells for epithelial folding via a basal polarity shift. *Nature Cell Biology*, 20:36–45, 2018.

[148] W. Tang and D. A. Bennett. Agent-based modeling of animal movement: a review. *Geography Compass*, 4:682–700, 2010.

[149] G. I. Taylor. Statistical theory of turbulence. iv. diffusion in a turbulent air stream. *Proceedings of the Royal Society of London. Series A-Mathematical and Physical Sciences*, 151(873):465–478, 1935.

[150] R. Tomer, K. Khairy, F. Amat, and P. J. Keller. Quantitative high-speed imaging of entire developing embryos with simultaneous multiview light-sheet microscopy. *Nature Methods*, 9:755–763, 2012.

[151] N. Tompkins, N. Li, C. Girabawe, M. Heymann, G. B. Ermentrout, I. R. Epstein, and S. Fraden. Testing Turing's theory of morphogenesis in chemical cells. *Proceedings of the National Academy of Sciences*, 111:4397–4402, 2014.

[152] P. K. Trong, H. Doerflinger, J. Dunkel, D. St Johnston, and R. E. Goldstein. Cortical microtubule nucleation can organise the cytoskeleton of Drosophila oocytes to define the anteroposterior axis. *eLife*, 4:e06088, 2015.

[153] A. M. Turing. The chemical basis of morphogenesis. *Bulletin of Mathematical Biology*, 52:153–197, 1990.

[154] J. A. Tuszynski, T. Luchko, S. Portet, and J. M. Dixon. Anisotropic elastic properties of microtubules. *The European Physical Journal E*, 17:29–35, 2005.

[155] Y. Wang, M. Sarkar, A. E. Smith, A. S. Krois, and G. J. Pielak. Macromolecular crowding and protein stability. *Journal of the American Chemical Society*, 134:16614–16618, 2012.

[156] P. A. H. Westley, A. M. Berdahl, C. J. Torney, and D. Biro. Collective movement in ecology: from emerging technologies to conservation and management. *Philosophical Transactions of the Royal Society B: Biological Sciences*, 373:20170004, 2018.

[157] W. Wiltschko and R. Wiltschko. Magnetic orientation and magnetoreception in birds and other animals. *Journal of Comparative Physiology A*, 191:675–693, 2005.

[158] M. L. Winston. *The Biology of the Honey Bee*. Harvard University Press, Cambridge, USA, 1st edition, 1987.

[159] F. Wrangell. *Narrative of an Expedition to the Polar Sea: In the Years 1820, 1821, 1822 and 1823*. Harper and Brothers, New York, USA, 1st edition, 1845.

[160] C. Xue, B. Shtylla, and A. Brown. A stochastic multiscale model that explains the segregation of axonal microtubules and neurofilaments in neurological diseases. *PLoS Computational Biology*, 11:e1004406, 2015.

[161] H. Yang and L. A. Pon. Actin cable dynamics in budding yeast. *Proceedings of the National Academy of Sciences*, 99:751–756, 2002.

[162] D. Zhang, K. D. Grode, S. F. Stewman, J. D. Diaz-Valencia, E. Liebling, U. Rath, T. Riera, J. D. Currie, D. W. Buster, A. B. Asenjo, H. J. Sosa, J. L. Ross, A. Ma, S. L. Rogers, and D. J. Sharp. Drosophila katanin is a microtubule depolymerase that regulates cortical-microtubule plus-end interactions and cell migration. *Nature Cell Biology*, 13:361, 2011.

[163] H. Zhou, G. Rivas, and A. P. Minton. Macromolecular crowding and confinement: biochemical, biophysical, and potential physiological consequences. *Annual Review of Biophysics*, 37:375–397, 2008.

[164] Y. Zilberman, C. Ballestrem, L. Carramusa, R. Mazitschek, S. Khochbin, and A. Bershadsky. Regulation of microtubule dynamics by inhibition of the tubulin deacetylase HDAC6. *Journal of Cell Science*, 122:3531–3541, 2009.